Understanding Catalyst Layer Morphologies and Degradation and their Impact on Critical Oxygen Transport in PEMFC Cathodes

Submitted in partial fulfillment of the requirements for
the degree of
Doctor of Philosophy
in
Mechanical Engineering

Jonathan P Braaten

B.S., Mechanical Engineering, Milwaukee School of Engineering

Carnegie Mellon University
Pittsburgh, PA

May, 2021

Acknowledgements

I would like to thank each of my dissertation committee members, Drs. Jonathan Malen, Jeremy Michalek, and Jay Whitacre for their time in advising and adjudicating my research efforts presented in this written dissertation and defense presentation.

I would like to thank my project partners and research collaborators at General Motors, 3M, Chemours, Ballard, University at Buffalo, Drexel University, and Cornell University for their invaluable discussions and collaboration efforts. I would like to acknowledge and thank the US Department of Energy, Office of Energy Efficiency and Renewable Energy for funding the work in this dissertation under grants DE-EE0007271, DE-EE0008076, and DE-0008822.

I would like to thank my lab mates, both current and former, for their assistance and support at each stage of my Ph.D. journey. Research is never a solo venture and each person in the lab for Transport Phenomena in Energy Systems (TPES) has contributed to my development as a researcher as well as my finished research projects and publications. Namely, I would like to thank my early Ph.D. mentors, Drs. Leiming Hu, Shohei Ogawa, Sarah Frisco, Siddharth Komini Babu, MD Aman Uddin, Bahareh Tavakoli, Bharathy Parimalam and soon-to-be Dr. Paul Choi. Their assistance and guidance proved invaluable in helping me get off the ground and succeed in my research and personal endeavors while at Carnegie Mellon University.

I would like to thank my family and friends for their endless support and encouragement during my years as a Ph.D. student. Namely, I would like to acknowledge my parents, Patrick and Nancy, my siblings, Emily, Josie, Isaac, and brother-in-law Matt for fielding late-night panic calls, existential crisis management, understanding in missed familial events, and overall grace whilst I finished my formal education. I would like to thank my friends, specifically Zach Posten, Scott Connors, Ariel Noorparvar, Alp Karacakol, Paula Arambel, Rebecca Gruener, Rachel Mego, Megan Huberty, and last but certainly not least, my amazing girlfriend Meg Kinzler for their dedication during my Ph.D. and for reminding me of life outside of the office and lab.

Finally, I would like to thank my advisor and mentor, Dr. Shawn Litster, for his 5 years of guidance and support in beginning, toiling through, and finishing my Ph.D. Shawn is a rare combination of genius and good-nature and has made my Ph.D. journey not only manageable but also enjoyable, and I will be forever grateful for his tutelage.

Abstract

Polymer electrolyte membrane fuel cells or PEMFCs are a promising technology to address the need for electrification of the US and world automotive fleets. They are well-suited to vehicles requiring longer range and higher power operation like semis, delivery trucks, and traditional fleet vehicles as a result of fuel cells' innate decoupling of energy conversion from storage, allowing the power generating fuel cell stack and fuel tank to be scaled independently as needed for range and/or power. However, PEMFC technology remains more expensive than the incumbent internal combustion engine as a result of PEMFCs' reliance on platinum (Pt) for the catalysts in their anodes and cathodes, making up roughly 40% of the overall stack cost at high production volumes. Pt does not benefit from economies of scale due to its pure raw material costs and thus there have been widespread efforts to reduce Pt loadings to levels consistent with the Pt usage in catalytic converters for internal combustion engine vehicles. With these efforts to reduce Pt, significant performance losses have been observed due to hindered reactant transport, specifically oxygen (O_2), and catalyst degradation and ultimately Pt loss has occurred.

In this dissertation, we outline five efforts aimed at better understanding and evaluating Pt-based catalyst degradation and the impacts on performance as well as addressing the need for improved O_2 transport to the catalyst surface that has traditionally hindered high power performance. Specifically, we studied Pt and Pt-alloy catalyst and carbon support degradation for state-of-the-art catalyst layers (CLs) using our nanoscale X-ray computed tomography (nano-CT) imaging technique. We then evaluated the impacts of leached cations from unstable and degraded catalysts as well as other common contaminants on the O_2 transport properties of the ionomer that covers the catalyst surface and studied the migration and accumulation of such cations within the CL in-operando using a novel X-ray conducive PEMFC in a hydrogen (H_2) pump configuration. In the final efforts of this dissertation, we examined the fundamental transport of O_2 through water-filled nanopores that are common in state-of-the-art carbon supports and integrated a novel high oxygen permeable ionomer (HOPI) with state-of-the-art CLs to improve PEMFC performance at low and high power, corresponding to improvement in heavy duty PEMFC vehicle efficiency and total available power.

Contents

List of Figures

List of Tables

Chapter 0

Introduction

With the current state of emissions and the progression of climate change causing biodiversity loss [1], extreme weather patterns [2], projected negative economic impacts [3], and much more, the need for clean power generation has become dire. The transportation industry is responsible for roughly 1/3 of climate-impacting CO_2 emissions [4] and is one of the main targets for curbing our impact on the planet. To reduce automotive emissions through electrification, many technologies have been researched and developed, specifically Lithium-ion batteries and H_2 fueled PEMFCs, the latter of which is the focus of this dissertation.

While Lithium-ion batteries have been established as the electrification technology of choice for smaller and low- to mid-range vehicles, they are hindered by their low gravimetric energy density and coupled energy storage and conversion. In contrast, PEMFC technology allows for the independent scaling of both range and power through the separation of storage and conversion, similar to traditional IC engines in terms of fuel tank and engine size, respectively. This decoupling allows for their application to transportation industries not well-suited for Li-ion batteries, such as long-range hauling, local delivery vehicles, buses, standard-duty pickup trucks, and SUVs. In recent years, this technology has gained traction and market share as a contributor to a greener auto fleet. However, many challenges remain before this technology can achieve mass-market penetration and help reduce our dependence on fossil fuels.

Two of the main inhibitors to PEMFC adoption are the cost and durability of PEMFC components, specifically the Pt catalyst used to maintain high reaction rates under high power loadings. Cost forecasting by the DOE has estimated that the raw cost of Pt will make up 40% of the overall PEMFC stack cost at high production volumes [5], reducing the affordability of PEMFC vehicles for the general public and preventing widespread adoption. Further, many works have shown degradation of the Pt catalysts and their carbon supports, resulting in unacceptable power losses due to reduced activities and contaminated membranes. The work described in this dissertation seeks to address a lack of understanding of these important PEMFC degradation mechanisms and their impacts, as well as research into the development of advanced cathode catalyst layers (CCLs) to mitigate transport losses. Specifically, this work contains analyses of state-of-the-art CCL degradation and the impact on specific transport processes, including O_2 transport through contaminated ionomers

and the migration and accumulation of contaminant cations during PEMFC operation. In addition, this work examined transport through water-filled nanopores relevant to the new class of high surface area carbon (HSC) supports that is not well understood and outlines an initial integration and optimization study for HOPIs in next-generation PEFMC CCLs.

0.1 Background

0.1.1 Polymer Electrolyte Membrane Fuel Cells (PEMFCs)

At a high level, PEMFCs function by combining H_2 and O_2 in an electrochemical reaction to form water, with heat and electricity as biproducts. As shown in Figure 0.1, the H_2 is broken down on the surface of the electrocatalyst in the anode to form protons and electrons in a H_2 oxidation reaction (HOR). The electrons are transported through the carbon support of the anode catalyst layer (ACL) to the external circuit, where they do electrical work driving the vehicle, while the protons are pulled through the proton exchange membrane (PEM) to the CCL. Once in the CCL, the protons move through an ion-conducting polymer, or ionomer thin-film network to the electrocatalyst surface, where they combine with the electrons from the external circuit and the O_2 that has diffused through the pores of the CCL to form water in the oxygen reduction reaction (ORR). The half-cell and full reaction equations are given below.

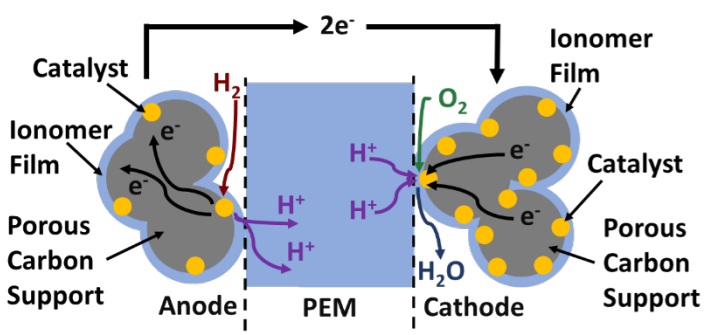

Figure 0.1: Schematic of PEMFC processes.

$$H_2 \rightarrow 2H^+ + 2e^- \text{ (Anode HOR)} \tag{0.1}$$

$$2e^- + 2H^+ + \frac{1}{2}O_2 \rightarrow H_2O \text{ (Cathode ORR)} \tag{0.2}$$

$$H_2 + \frac{1}{2}O_2 \rightarrow H_2O + heat + electricity \text{ (Full)} \tag{0.3}$$

The ACL and CCL typically consist of Pt catalyst particles supported on porous carbon, all bound by thin films of ionomer. The carbon provides structural stability for the catalyst and a pathway for electrons to access the catalyst particles while the protons are transported through the network of ionomer films to the surface of the catalyst. The ACL and CCL are

traditionally hot-pressed or cast to the PEM, forming continuous ionomer paths that allow the protons to be efficiently transferred from the ACL to the CCL. The ACL/PEM/CCL assembly is known as a membrane electrode assembly, or MEA.

0.1.1.1 The Carbon Support

There are many types of carbon support, but current state of the art supports feature either a medium surface area Vulcan (Vu) (shown in Figure 0.2a) or a high-surface area (HSC) support, the latter of which was the focus of our previous sponsoring project through the DOE and GM – Highly Accessible Catalysts for Durable High-Power Performance [6]. Vu supports have few internal mesopores (diameter < 10 nm), whereas the HSC-type supports have many [7, 8]. These small internal pores are extremely important, as they allow access to internal Pt particles that are inaccessible and thus inactive for lower surface area supports [9], as shown in Figure 0.2b. As a result, these HSC supports have been shown to dramatically increase catalytic accessibility, boosting performance under all operating conditions, but especially under high current density conditions, which are of interest for high power applications [9]. However, they have been shown to be less robust than lower surface area supports like Vu or graphitized carbon, a low surface area carbon (LSAC) support [10, 11].

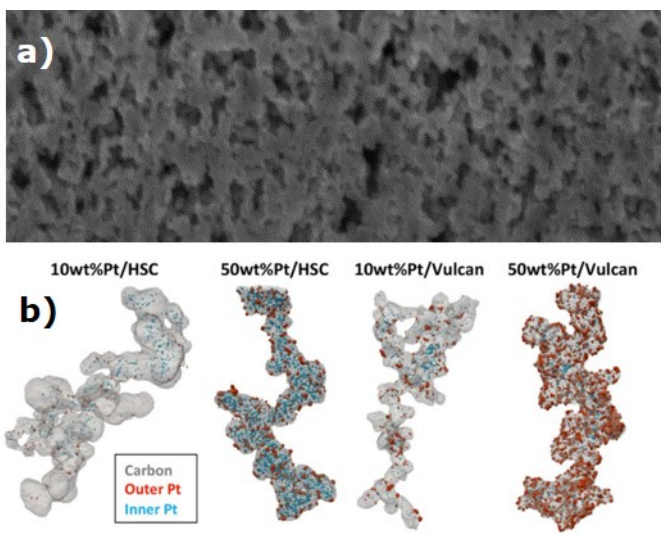

Figure 0.2: a) PFIB-SEM image of porous Vu carbon support and b) Cryo-STEM tomography of Vu and HSC carbon agglomerates with internal and external Pt [9].

0.1.1.2 The Ionomer

The ion-conducting polymer, or ionomer, traditionally consists of a polytetrafluoroethylene (PTFE) backbone with side chains terminating in a negatively charged sulfonic acid functional group. These sulfonic acid groups enforce negative ion and electron exclusion (electrically insulate) but allow for cations (like protons) to be transferred between sulfonic

acid groups. In PEMFCs, there are two general forms of the ionomer. The first is the bulk form which makes up the PEM. The PEM serves to electrically insulate the ACL from the CCL, preventing electrical shorting, while allowing for proton migration to the CCL where the ORR reaction occurs. The second form of the ionomer consists of the thin films, which cover and bind the exposed surface of the carbon/catalyst matrix of the CCL. These thin films allow for protons to move within the ACL and CCL, extending the reach of the HOR and ORR reactions into the ACL and CCL, respectively.

The internal structure of the ionomer is extremely complex and hotly debated, even after decades of study. The most well-accepted description of its structure consists of an inverted micelle network (Figure 0.3a), where the non-polar PTFE backbones collapse together [12] with the polar sulfonic acid groups facing in [13, 14, 15, 16]. This results in distinct phase segregation, with water collecting near the polar sulfonic acid groups, forming a vast interconnected water domain [13] at high water activities (relative humidity – RH), as shown in Figure 0.3b. The polar hydrophilic domains provide a pathway for proton (and other cation) transport, while the collapsed PTFE backbones provide structural rigidity for the membranes. In the thin films within the CCL, the phase segregation present in the bulk ionomer is suppressed, leading to even more complex and less-well understood structures and properties [17, 18, 19].

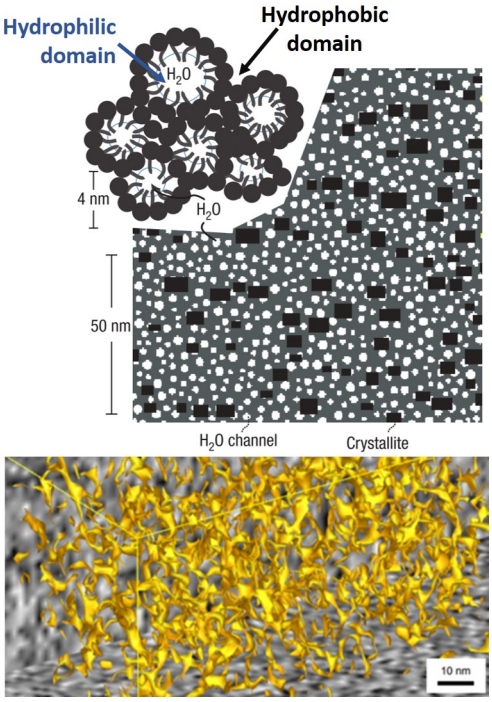

Figure 0.3: a) Hypothesized inverted micelle structure of ionomers [16]. Used with permission from Nature Materials, ©2008. b) Cryo-electron tomography of Nafion (gold corresponds to the hydrophilic water domain) [13]. Used with permission from the American Chemical Society (ACS), ©2014 (https://pubs.acs.org/doi/10.1021/mz500606h). Further permissions related to the material excerpted in b) should be directed to the ACS.

0.1.1.3 The Catalyst

The catalyst typically consists of nano-dispersed Pt or Pt-based particles distributed on the surface and within the pores of the carbon support. Due to its high cost [5], significant efforts have been made to reduce the amount of Pt used in PEMFCs by improving utilization through the above-mentioned carbon support techniques as well as alloying with transition metals (e.g. Co, Ni, Fe, etc.) to boost the catalytic activity [20, 21]. However, characterization of these reduced Pt loaded and alloyed catalyst MEAs has indicated performance losses attributed to catalyst particle degradation and resultant ionomer poisoning [22, 23, 24, 25]. The following sections will describe in detail the fundamentals of the degradation processes and broadscale impacts of the lost Pt and contamination of the MEA.

0.1.2 Catalyst Degradation

It has been shown through numerous studies that Pt-based catalysts degrade during voltage cycling, resulting in electrochemically active surface area (ECSA) loss [21, 22]. This is the result of instability of the Pt and transition metals under the electric potential and acidic conditions of a PEMFC [26]. Under these high potential and low pH conditions, Pt is stripped from the surface of the particles and ionized, forming Pt^{2+}. These Pt^{2+} cations are then absorbed by the ionomer and diffuse/migrate through the water/ionomer network. Depending on the conditions in the cell, the Pt^{2+} cations can be reduced back to neutral Pt with crossover H_2 from the ACL [25], forming a Pt band [21, 25], or be redeposited on another Pt particle in a process known as particle coarsening [21, 23]. Each of these mechanisms results in an irreversibly reduced ECSA and a corresponding loss in PEMFC power. Given the cost of raw Pt, any loss of ECSA is significant and methods of minimizing or preventing it are of the utmost importance.

With the implementation of Pt alloys, typically PtCo or PtNi, further performance impacts are witnessed. The alloyed transition metals are much less stable than Pt and therefore ionize under less extreme conditions. Thus, catalysts are typically designed such that the alloying element besides Pt is confined to the interior of the catalyst particle with a few layers of Pt around the alloyed core, called the Pt 'skin.'[27, 28, 29] However, with cycling and Pt degradation, it is possible for the alloying element to be exposed to the acidic ionomer, leading to rapid dissolution and absorption by the membrane. These leached cations do not redeposit on other catalyst particles or get reduced to their neutral forms with crossover H_2. Rather, they remain in the ionomer films and PEM as mobile contaminants that are not consumed in any electrochemical reaction and therefore cannot be easily removed or eliminated.

0.1.3 Catalyst Layer Oxygen Transport

As the Pt loadings are reduced in PEMFC CCLs either intentionally or through irreversible degradation, the O_2 flux through the thin ionomer films on top of each catalyst site becomes much greater. With these increased fluxes, additional performance losses have become apparent at high current densities and have been attributed to high O_2 transport resistances

or R_{O2}'s through the ionomer films in the CCLs [30, 31, 32]. Further, the introduction of contaminant cations like Co^{2+} (from the cores of degraded PtCo alloy catalysts) has caused an additional resistance, especially at low RH/water activity [33, 34].

Ionomer structure and transport studies have indicated that O_2 primarily diffuses through the hydrophilic domains of the ionomer and that higher water contents result in improved O_2 transport [35, 36, 37, 38, 39]. Given the phase segregated structure of the ionomer, we suspect that increased water contents result in an expanded hydrophilic domain and lower point-to-point diffusion tortuosity compared to the ionomer's dry state. Other studies have shown that for ionomer's doped with contaminant cations, there exist significant structural changes due to stronger ion pairing, reduced water uptake, and ionic cross-linking for multivalent cations [40, 41, 42, 43, 44, 45]. From their results, we have hypothesized that contaminant cations like Co^{2+} or Ni^{2+} cause distortion of the hydrophilic domain and a more tortuous O_2 path.

In addition to diffusion through the ionomer films, permeation through the porous carbon layers also has to be taken into account. There are many sizes of pore inside PEMFC CLs, corresponding to the different materials that make up the CLs and diffusion media, which impact the ability of O_2 to diffuse at a rate capable of maintaining high current densities. Different diffusion regimes determine the overall diffusivity of O_2 through these layers, including the Knudsen regime for pores less than 5 nm in diameter (common in CLs), a transition regime for pores between 5 nm and 5 µm (CLs and diffusion media), and a bulk regime for voids larger than 1 µm (flow channels and diffusion media) [46]. In cases where the pores are filled with liquid water (PEMFCs typically operate below 100°C), O_2 transport is further reduced.

0.1.4 Catalyst Layer Cation Transport

The mobile and permanent contaminant cations in the ionomer are suspected to migrate as a function of the potential gradient in the operating PEMFC, forcing them towards the CCL [47, 48], as shown in Figure 0.4. With high percentages of these contaminant cations relative to the number of sulfonic acid sites, protons have difficulty moving through the ionomer, resulting in a high electrical resistance. In addition, large contaminant cation exchanges in the ionomer films near the surface of the catalyst are suspected to cause large R_{O2}'s. Both mechanisms are suspected to contribute to the performance degradation witnessed for contaminated MEAs [33, 34]. Due to these effects, knowledge of the migration and accumulation tendencies of these cations within the CLs of PEMFCs is critical to their mitigation and to-date is not well documented or validated. Further, knowledge of the mechanisms of these cations' migration and accumulation in confined films is even less understood. Given their impact on performance, understanding and minimizing these phenomena is important for development of next-generation PEMFCs.

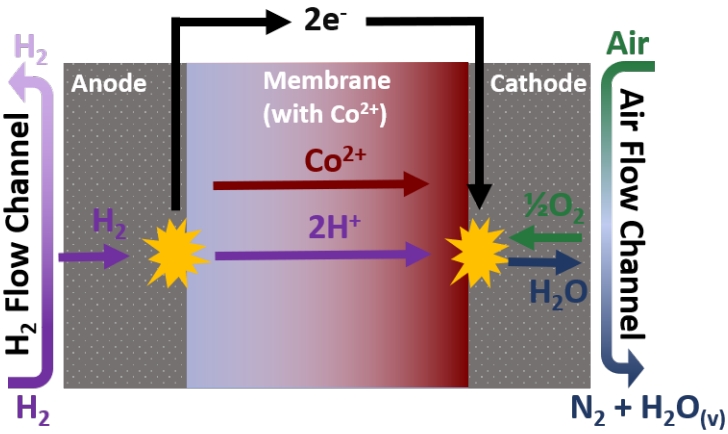

Figure 0.4: Suspected migration of Co^{2+} (or other foreign cation) to the CCL during PEMFC operation due to the potential gradient formed during cell polarization.

0.2 Scope of Dissertation

The work outlined in this dissertation seeks to address the need for improved understanding of fuel cell degradation processes and their impacts on specie transport within the critical CCL as well as better understanding and improvement of the critical O_2 transport pathway. In Chapter 1, we present a combined electrochemical characterization and nanoscale X-ray computed tomography (nano-CT) imaging technique to analyze structural changes to state-of-the-art CCLs resulting from catalyst-specific accelerated stress tests or ASTs and discuss the changes within the context of the CCLs' observed performance degradation. In Chapter 2, we examine the impact of leached catalyst alloying elements and other cationic contaminants on the O_2 transport properties of ionomer films. In Chapter 3, we present a novel operando analysis of cation migration and accumulation within the CL of a functioning PEMFC MEA. To round out this dissertation, we show a fundamental analysis of O_2 transport through water-filled nanopores representing the micro- and mesopores of advanced HSC supports in Chapter 4, as well as an initial CCL integration and optimization effort with a novel high-performance HOPI for enhanced PEMFC efficiency and power in Chapter 5. The final chapter of this dissertation presents brief summaries, contributions, and future efforts from the above-mentioned analyses.

Chapter 1

Studying Pt-Based Fuel Cell Electrode Degradation with Nanoscale X-Ray Computed Tomography

1.1 Motivation

It has been shown in numerous studies [21, 22, 23, 25] that Pt catalysts degrade during PEMFC voltage cycling, causing decreased ECSA and a corresponding loss in power density. Numerous methods have been used to analyze this phenomenon, including SEM and TEM [22, 23, 25] and the results of these studies have indicated that Pt is stripped from the surface of the catalyst particles at high potentials corresponding to the formation of Pt-oxide species and the ionization and dissolution of Pt [22, 49]. Once dissolved from the catalysts' surfaces, these Pt cations (Pt^{2+}) migrate either to larger particles in a process known as particle coarsening [23] or are reduced by crossover H_2 in the PEM, forming a 'Pt band' close to the PEM/CCL interface [22, 25]. With the redistribution of Pt for both cases, the ECSA of the CCL is irreversibly decreased, resulting in significant performance losses. Thus, understanding these degradation mechanisms as well as methods of minimizing the loss of expensive Pt is of great priority in bringing PEMFC technology to the forefront of the automotive industry's push towards a greener auto fleet.

In this work, we sought to analyze 3 CCL degradation phenomena: carbon support stability, ECSA loss, and Pt band formation. Catalyst degradation processes have traditionally been evaluated with high-resolution SEM or TEM methods, which suffer from small sample heterogeneities and edge and processing artifacts. We wanted to characterize these phenomena over a larger, more representative MEA volume than is possible with these traditional methods and our laboratory-scale nano-CT machine allowed us to do so.

The nano-CT method has previously been used for CL and MEA-scale morphological studies, including the examination of anode carbon corrosion due to cell reversal [50], porosity/tortuosity analyses [46, 51, 52], and ionomer distribution mapping [52, 53, 54]. While not capable of resolving morphological features less than 50 nm in high-resolution mode and 192 nm in the large field of view mode (used in this study), this technique allowed for the

characterization of the phenomena mentioned above with the dual Zernike phase contrast (ZPC) and absorption contrast (ABS) modes for evaluating the solid/void morphology and Pt distributions, respectively. Our workflow included the electrochemical characterization (ECSA and polarization curves) and subsequent ex-situ nano-CT imaging of the MEAs before and after the catalyst AST cycling. The two catalyst types used in this study were Vulcan-supported Pt (Pt/Vu) and KetjenBlack high-surface-area carbon-supported Pt_3Co (PtCo/HSC). Pt/Vu has traditionally been used in prototype FCEVs, while PtCo/HSC has become more popular thanks to its higher activity. Further, Vu is a solid, compact carbon while the KetjenBlack is an HSC with a large amount of accessible internal porosity in the carbon particles. Comparing the degradation of these MEAs allowed us to observe the change in large-scale carbon void feature distribution or macroporosity, as well as the Pt loss to the Pt band as a function of both carbon support and metal catalyst. This data was then compared with the results of the ECSA and polarization measurements to determine the impact of each degradation process on the performance of the MEAs.

1.2 Experimental

1.2.1 MEA Preparation

The performance of the CCLs were evaluated using MEAs with active areas of 50 cm^2. Both 20 wt. % Pt/Vu and 30 wt. % PtCo/HSC electrocatalysts were tested as the CCLs. The PtCo catalyst was washed with an acid solution to prepare a dealloyed core-shell PtCo catalyst with an average Pt to Co atomic ratio of 3, per the method of Han et al [55]. 20 wt. % graphitic carbon-supported Pt was used for the anode catalyst layer (ACL). A perfluorosulfonic acid (PFSA) ionomer dispersion (Nafion D2020) was used to fabricate the electrode catalyst layers with the ionomer to carbon weight ratios (I/C) fixed at 0.8. The electrode inks were coated on a sheet of ethylene tetrafluoroethylene using Mayer rods with given sizes to result in target Pt loadings of 0.1 and 0.025 mg_{Pt}/cm^2 in the CCL and ACL, respectively. Although there is some variation across large numbers of prepared sample sheets using this technique, the variation of Pt loading within the small sample pieces used in this study (7×7 cm) is usually less than 5%. Table 1.1 shows the measured Pt loadings for each CCL using calibrated X-ray fluorescence. The electrodes were then transferred from the decals to an 18 µm thick PFSA membrane using a planar hot press. More details on the MEA lamination procedure can be found in a previous publication [20]. The gas diffusion media used for this study consisted of a 30 µm thick microporous layer coated on top of a 240 µm thick carbon paper.

1.2.2 MEA Cycling

A US DOE-recommended catalyst AST was used to study the durability of the Pt/Vu and PtCo/HSC CCLs. The catalyst AST was targeted towards accelerating Pt particle degradation. A total of 30,000 trapezoidal voltage cycles were run with the lower and upper voltage limits being 0.6 and 0.95 V. The residence time at both 0.6 and 0.95 V was 2.5 s and the

Table 1.1: CCL Pt loading for each MEA tested [56]. Used with permission from the Journal of Power Sources ©2020.

MEA Sample	CCL Pt Loading [mg_{Pt}/cm^2]
Pt/Vu-Fresh	0.136
Pt/Vu-30k Cycles	0.120
PtCo/HSC-Fresh	0.084
PtCo/HSC-30k Cycles	0.104

ramp time was 0.5 s. Each voltage cycle required 6 seconds total. A set of electrochemical measurements (ECSA and performance/polarization curves) were performed after 0 (fresh), 10k, and 30k AST cycles. The performance (polarization) curves were recorded at 94°C, 65% RH_{inlet}, 250 $kPa_{abs,outlet}$ under H_2/air at stoichiometries of 1.5/2.

1.2.3 Nano-CT Sample Preparation

To image the MEA samples after cycling, 1 mm square sections of the samples were cut from the channel (uncompressed) area of the 50 cm^2 MEAs and subsequently cut in half using razor blades, forming two triangles. The triangles were then glued to sewing pins so they could be installed in the nano-CT instrument's pin mount sample holder. The edges of the samples were then folded together and glued, resulting in a 'flag-style' pin mount. This process is shown in Figure 1.1, along with the corresponding microscope and X-ray view (ZPC) of the PtCo/HSC 30k sample (in-plane). This mounting technique allowed for a small portion of the tip of the MEA to be imaged and reconstructed, giving solid volume data for the ACL, CCL, and PEM of each MEA sample.

1.2.4 Imaging

We utilized our laboratory-scale nano-CT instrument (XRadia UltraXRM-L200, Carl Zeiss X-ray Microscopy, Inc., Pleasanton, CA) to evaluate the MEA samples in their fresh and cycled states. The nano-CT method has been described in a previous work [57] but fundamentally functions by passing X-rays (8keV) through a sample and detecting the change in intensity due to high-Z materials (ABS mode) or the phase shift through the material (ZPC mode) for the creation of a 2-D radiograph. A series of these radiographs over a range of angles allowed for the reconstruction of a solid volume of the MEA using Zeiss' proprietary reconstruction software, which utilizes the filtered back projection algorithm.

The nano-CT method consists of two different techniques, depending on which features are being studied. The two techniques available for this method are ZPC and traditional ABS. The ZPC technique allows for phase distinction, made possible through a Zernike phase ring, and is advantageous for differentiating voids and solids, especially in low-Z materials like carbon. The ABS technique allows for the distinction of high-Z materials like Pt or gold,

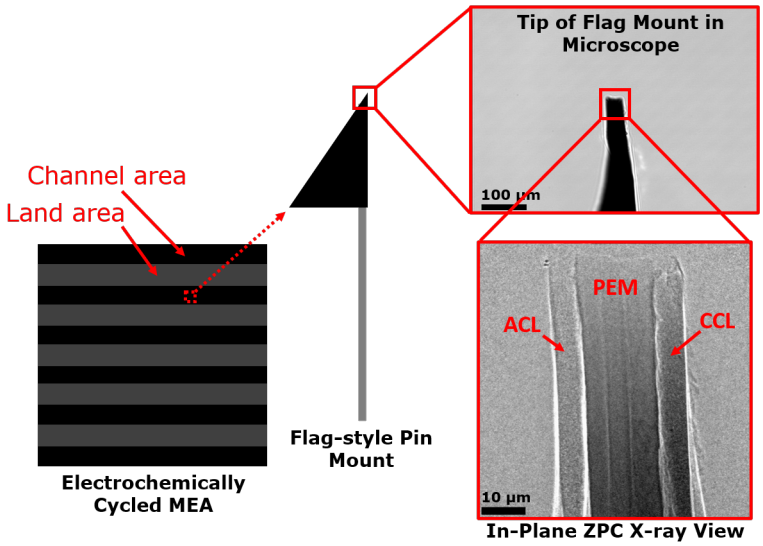

Figure 1.1: MEA sample assembly and tomographic arrangement [56]. Used with permission from the Journal of Power Sources ©2020.

which appear much brighter than their low-Z carbon counterparts, allowing for the rendering of the Pt band as well as the Pt in the ACLs and CCLs of our MEA samples. Thus, for evaluating carbon support degradation and Pt dissolution and migration to form the Pt band, the nano-CT method has the appropriate analysis techniques available to accomplish a high-quality comparison of the catalyst and support degradation mechanisms of interest in this study.

The resolution (pixel/voxel size) of our instrument varies by analysis mode and binning. There are two modes accessible for both the ZPC and ABS techniques: LFOV and high resolution (HRES). The LFOV mode is characterized by a 65 µm detector/viewing area and has a voxel size of 64 nm for a binning of 1. This voxel size can be changed by using less sensitive binnings (2, 4 or 8) to achieve higher X-ray counts for shorter imaging times, at the expense of spatial resolution. The HRES mode is characterized by a 16 µm detector/viewing area and has a voxel size of 16 nm for a binning of 1. In this study, we utilized only the LFOV mode and a binning of 1 for the carbon support analysis (ZPC), and a binning of 2 for the Pt band analysis (ABS). We found that the LFOV mode provided a sufficient representative volume and resolution for this analysis. The HRES mode was not utilized in this study but could augment future analyses with a more complete porosity analysis down to 50 nm.

After the tomographies of each sample were completed according to the imaging parameters in Table 1.2, the X-ray datasets were reconstructed into solid volumes using Zeiss' proprietary software. The resulting volumes consisted of 3D matrices of intensity values corresponding to the Z-number and/or density of the material (ABS) and pore/solid (ZPC). Then, using the PoreSpy toolbox [58] and in-house MATLAB and Python scripts, the large-scale void feature and Pt distributions were characterized for each sample.

Table 1.2: Tomography parameters for each sample and nano-CT imaging mode [56]. Used with permission from the Journal of Power Sources ©2020.

Sample-Mode	Radiograph Duration [s]	Binning	Angle Range [°]	Number of Radiographs
Pt/Vu Fresh-ZPC	90	1	180	901
Pt/Vu 30k-ZPC	90	1	180	901
Pt/Vu Fresh-ABS	30	2	180	901
Pt/Vu 30k-ABS	30	2	180	901
PtCo/HSC Fresh-ZPC	120	1	180	901
PtCo/HSC 30k-ZPC	115	1	180	901
PtCo/HSC Fresh-ABS	45	2	180	901
PtCo/HSC 30k-ABS	45	2	180	901

*Note that the radiograph durations were adjusted on an as-needed basis, to counteract the effects of the nano-CT instrument's X-ray source degradation.

1.2.5 Large-Scale Void Feature Analysis

With the 3D matrix of intensities attained from the reconstruction, we performed a reorientation, segmentation, and cropping operation using AVIZO (Avizo 9.0, Thermo Fisher Scientific, Waltham, MA) to extract a through-plane region of interest (ROI) that included the ACL, PEM, and CCL. A binary segmentation was performed such that the ACL's large-scale void feature volume fraction was the same for each MEA sample. For each sample, the segmentation parameter used for the ACL was then applied to the CCL, yielding a segmented volume with binary data corresponding to solids and voids. This binarized data was then fed into the PoreSpy analysis toolbox [58] to generate void feature distributions. It is important to note that the nano-CT LFOV mode's voxel size of 64 nm prevents identification of pores smaller than this, all the way up to roughly 3 times the voxel size (192 nm equivalent spherical diameter), as pores are difficult to accurately identify without 20-30 voxels of data in 3D (ca. 3x3x3 voxel volume). Thus, this analysis is considered a large-scale void feature or macroporosity analysis, and the data shown in the Results should only be considered accurate for void equivalent diameters greater than 192 nm.

1.2.6 Pt Band Analysis

For the Pt band analysis, the intensity volume data was imported to AVIZO, normalized with respect to the ABS intensity of the PEM, reoriented such that the MEA was aligned parallel to the orthogonal axes, and cropped to remove any artifacts and edge effects. This data was then exported to MATLAB, where a slice averaging method was used to analyze the intensities of each in-plane slice of the MEA. This data was then plotted against the thickness of the MEA to show the slice averages of the highly attenuating Pt, yielding a through-plane Pt distribution. An additional analysis was performed to give insight into the distribution of Pt within each slice. Instead of averaging, the pixel intensities were binned,

yielding a probability distribution function (PDF) of the intensities for each slice through the thickness of the MEA and giving insight into the uniformity of the Pt band and degradation-affected regions of the CCL.

1.3 Results

1.3.1 Electrochemcial Analysis

The results from the ECSA and performance characterizations are shown in Figures 1.2 and 1.3, respectively. Consistent with a previous analysis [59], the ECSA decreased for both MEA types tested at both 10k and 30k cycles. However, we observed less ECSA degradation for the PtCo/HSC samples compared to the Pt/Vu samples (30% loss vs 75% loss). This is largely due to the larger mean particle size of PtCo catalysts compared to pure Pt catalysts (4.4 vs 2.4 nm) and thus a lower Pt dissolution rate, as well as the documented ability of HSCs to suppress catalyst degradation [59]. The polarization curves showed decreased power densities for both types of MEA, again with a greater reduction witnessed for Pt/Vu. However, the origins of the power density decrease were different between the types of MEA. For the cycled Pt/Vu sample, there is a significant drop in voltage within the activation region of the polarization curve and a steeper linear region at moderate and high current densities. In contrast, the cycled PtCo/HSC sample showed little to no decrease in activity and little to no increase in the slope of the linear region at moderate current densities. Rather, the power density decreased only at high current densities (>1.5 A/cm^2), indicating mass transport limitations.

1.3.2 Large-Scale Void Feature Analysis

The raw ZPC data from each MEA sample's reconstruction is shown in Figure 1.4, noting the porous nature of the ACL and CCL, in contrast with the continuous PEM X-ray signal. The greyscale values correspond to a range of ZPC intensities, with bright pixels corresponding to the void/solid interfaces and dark pixels corresponding to voids. Using a binary segmentation and the PoreSpy toolbox as described previously, we generated void distributions for each MEA sample's ACL and CCL. This allowed us to examine the degradation of each CCL's carbon support after the catalyst AST cycling. Figure 1.5a shows the ACLs' void structure volume fractions, which were used to inform the binary segmentation parameters used in the CCL analysis. Figures 1.5b and 1.5c show the fresh and cycled CCLs' large-scale void feature volume fractions for Pt/Vu and PtCo/HSC, respectively.

From 1.5b, the Vu support's large-scale void structure remained unchanged during the AST cycling, whereas the HSC support (Figure 1.5c) experienced a significant reduction in the large-scale void volume or macroporosity, which is likely due to crushing effects or primary particle rearrangement resulting from carbon oxidation/corrosion and/or membrane swelling and cell compression over time and cycling [10, 60, 61]. The loss in macroporosity is consistent with electrode thinning witnessed for similar HSC supports under catalyst AST

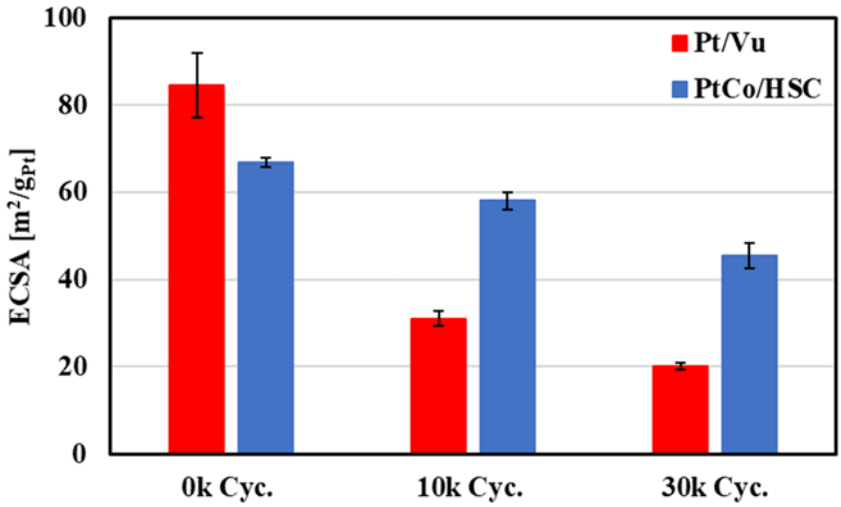

Figure 1.2: ECSA data for fresh, 10k cycles, and 30k cycles MEAs [56]. Used with permission from the Journal of Power Sources ©2020.

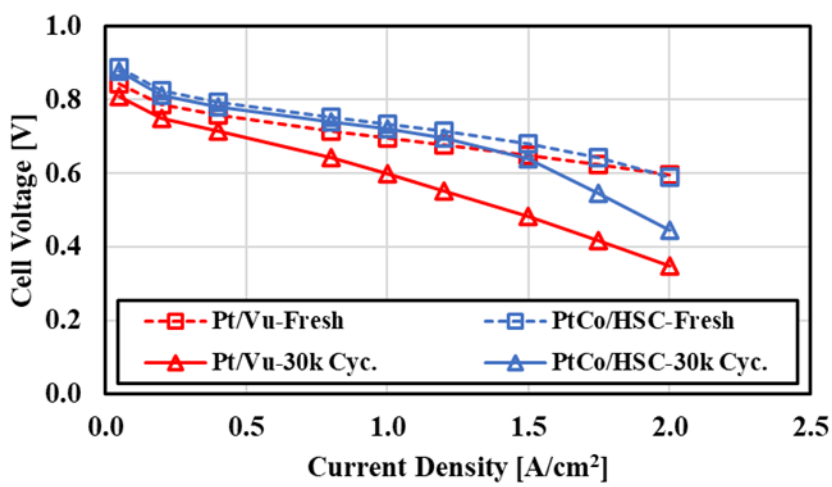

Figure 1.3: Polarization curves for fresh and 30k cycles MEAs at 94°C, 65% RH_{inlet}, 250 $kPa_{abs,outlet}$ under H_2/air at stoichiometries of 1.5/2 [56]. Used with permission from the Journal of Power Sources ©2020.

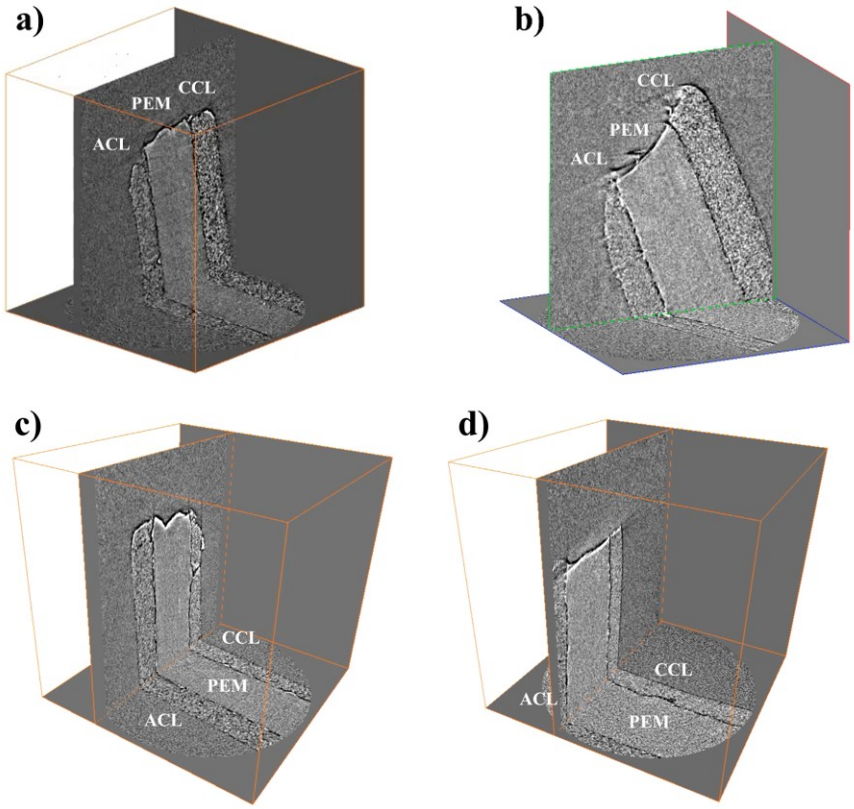

Figure 1.4: LFOV ZPC orthogonal slice renderings for a) Pt/Vu-fresh b) Pt/Vu-30k cycles c) PtCo/HSC-fresh and d) PtCo/HSC-30k cycles samples. Note that bright pixels correspond to solid/void interfaces and the dark pixels correspond to voids [56]. Used with permission from the Journal of Power Sources ©2020.

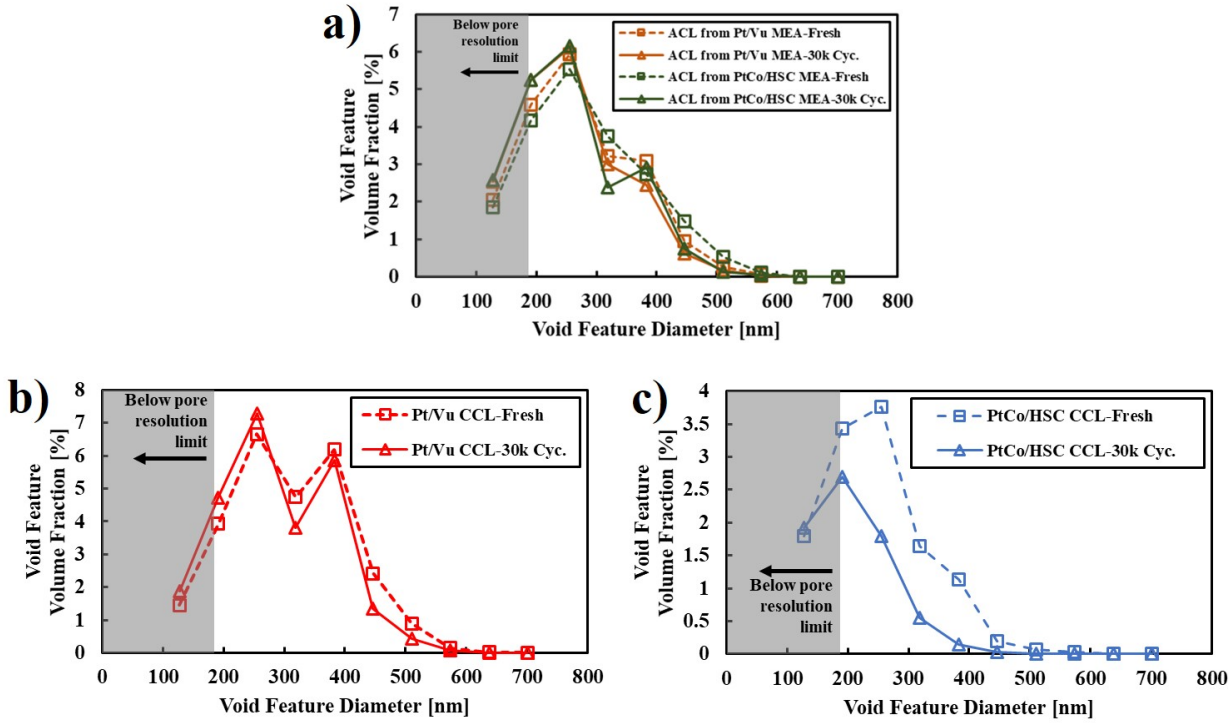

Figure 1.5: Large-scale void feature distributions from a) all graphitized carbon ACLs, b) Pt/Vu CCLs, and c) PtCo/HSC CCLs [56]. Used with permission from the Journal of Power Sources ©2020.

cycling [11], though electrode thinning was not witnessed in our analysis, which is likely due to sample-to-sample heterogeneities in CCL thickness masking the effect of CCL thinning. This analysis case illustrates well the advantage of the nano-CT technique; we can capture the changes in porosity/macroporosity over a larger representative volume than traditional methods, yet on the scale relevant to the internal morphology that is dependent on the carbon support type rather than deposition effects like overall CCL thickness.

The reduction in the macroporosity helps elucidate the origins of the mass transport loss seen for the cycled PtCo/HSC sample in Figure 1.3, compared to the Pt/Vu sample which had neither the macroporosity reduction nor the mass transport losses in the polarization curve. While at the current time we speculate on the origins of this loss in macroporosity for HSC supports, further research and analysis can and should be performed to better understand this loss.

When comparing the void volume fractions in Figures 1.5b and 1.5c, we observed that the total large-scale void volume fraction of the Vu support was greater than that of the HSC support. This is justified, given that our technique does not accurately capture voids below 192 nm equivalent pore diameter. Both the Vu and HSC supports are known to have significant volume fractions of pores below 200 nm, with HSC supports known to have a

greater volume fraction in this range [62]. With our analysis, we were unable to capture pores in this range, resulting in an initially misleading conclusion. When accounting for the volume fraction of the micro- and mesopores, the HSC support will have a higher overall porosity than the Vu.

1.3.3 Pt Band Analysis

The raw ABS data from each MEA sample's reconstruction is shown in Figure 1.6. Once these datasets were properly normalized, oriented, and cropped, each MEA's average ABS intensity was plotted for each slice through the thickness of the MEA. These results are shown in Figures 1.7a and 1.7b. From these plots, we can see an intensity spike at the PEM/CCL interface, corresponding to the formation of a Pt band in the 30k cycle samples. There exists a much smaller intensity spike in the fresh samples, which is likely due to Pt agglomeration during MEA fabrication. In addition, there are some proprietary high-Z radical scavengers located in the PEM, near the CCL, which cause the intensity of the PEM to increase prior to the Pt band peak. In addition to the Pt band peak, we see a region of Pt loss, or Pt depletion trough, inside each of the cycled CCLs, beginning roughly halfway through the CCL and increasing in depth until the Pt band, consistent with the analysis by Padgett et al [59]. It is important to note that the intensities of the Pt/Vu CCLs are roughly similar in the regions without dissolution, whereas the intensities of the PtCo/HSC CCLs are different. This is the result of different Pt loadings, as shown in Table 1.1, where the cycled PtCo/HSC sample has a 20% higher Pt loading than the fresh version. In addition, the relative amount of ECSA loss (Pt band peak height relative to CCL Pt signal) was less for the PtCo/HSC samples compared to the Pt/Vu samples, which is consistent with less ECSA loss for PtCo/HSC as shown in the ECSA measurements of Figure 1.2.

From the through-plane intensity plots of Figure 1.7b, it is apparent that the thickness of the 30k cycled HSC CCL is greater than the thickness of the fresh HSC CCL. While this may at first appear to be contradictory to the expected electrode thinning seen by other work's catalyst AST cycling of similar supports [11] and our reduced macroporosity for the 30k cycled HSC CCL in 1.5c, we must acknowledge the sample-to-sample variation in CL thickness across these fabricated MEAs' areas. Thus, while we witness the loss in macroporosity that leads to thinning, the local thickness heterogeneities will mask this effect in our through-plane slice analysis.

In addition to plotting the slices' average intensities, we also show the distribution of the ABS intensities through the thickness of the MEA. These plots are shown in Figure 1.8, where the dark regions correspond to a narrow distribution of intensities and the light regions correspond to wide distributions. As is shown in Figures 1.8a and 1.8c, the fresh samples have very narrow distributions through the entirety of the MEA. Once the MEAs have been cycled (Figures 1.8b and 1.8d), however, the distributions widen in the regions of dissolution and agglomeration, showing the loss of Pt particle size uniformity in the CCL and the heterogeneity of the Pt band.

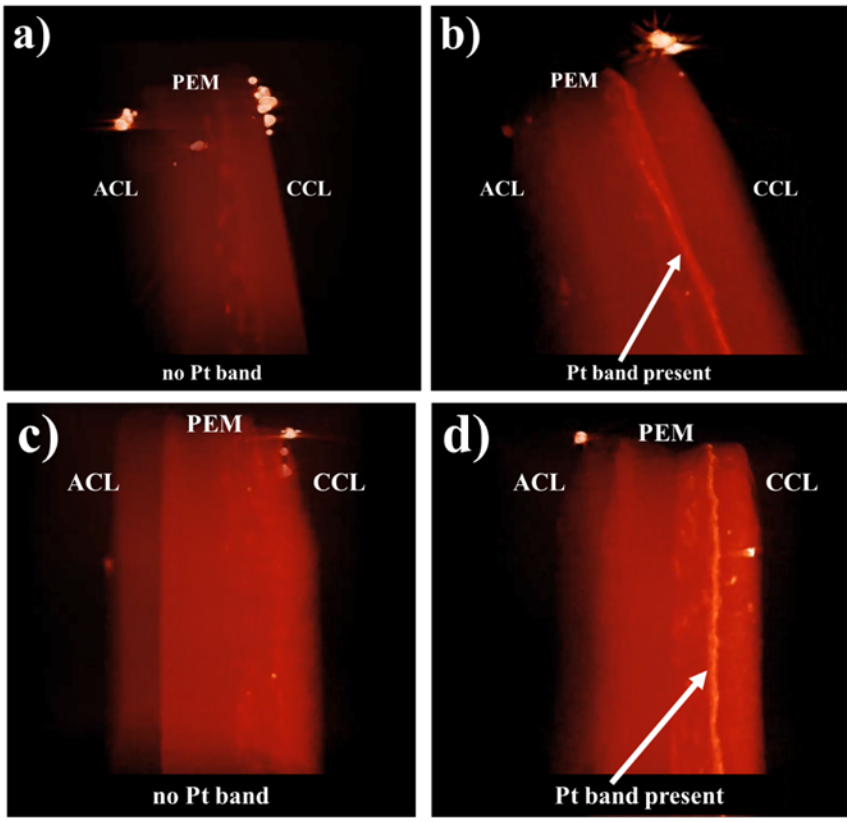

Figure 1.6: LFOV ABS high-Z (Pt) distributions in a) Pt/Vu-fresh b) Pt/Vu-30k cycles c) PtCo/HSC-fresh and d) PtCo/HSC-30k cycles MEA samples. Note the presence of the Pt band present at the CCL/PEM interface for both cycled samples. The high attenuation balls near the tip of each sample are gold fiducials installed ex-situ for reconstruction purposes [56]. Used with permission from the Journal of Power Sources ©2020.

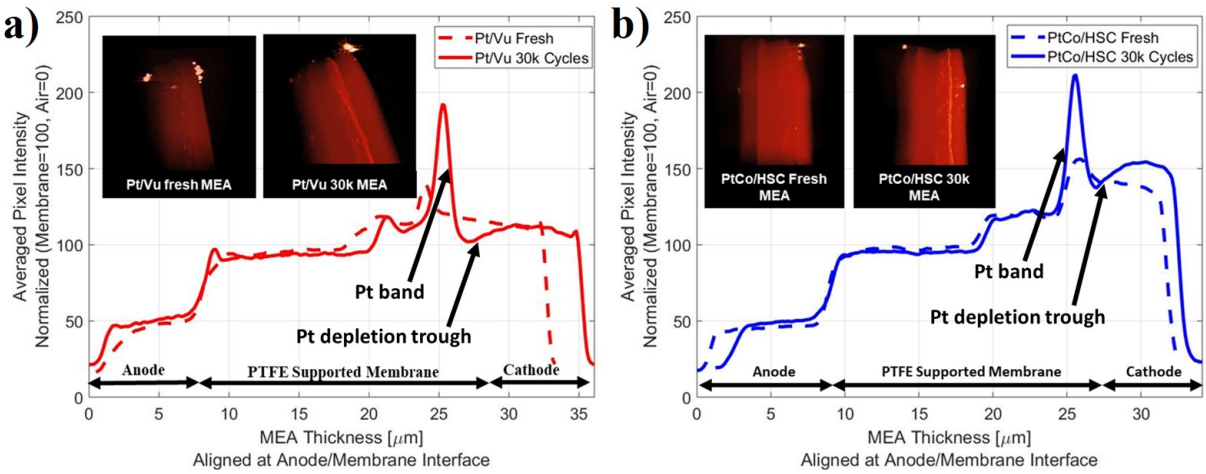

Figure 1.7: Average slice intensity (ABS) for a) Pt/Vu MEAs and b) PtCo/HSC MEAs [56]. Used with permission from the Journal of Power Sources ©2020.

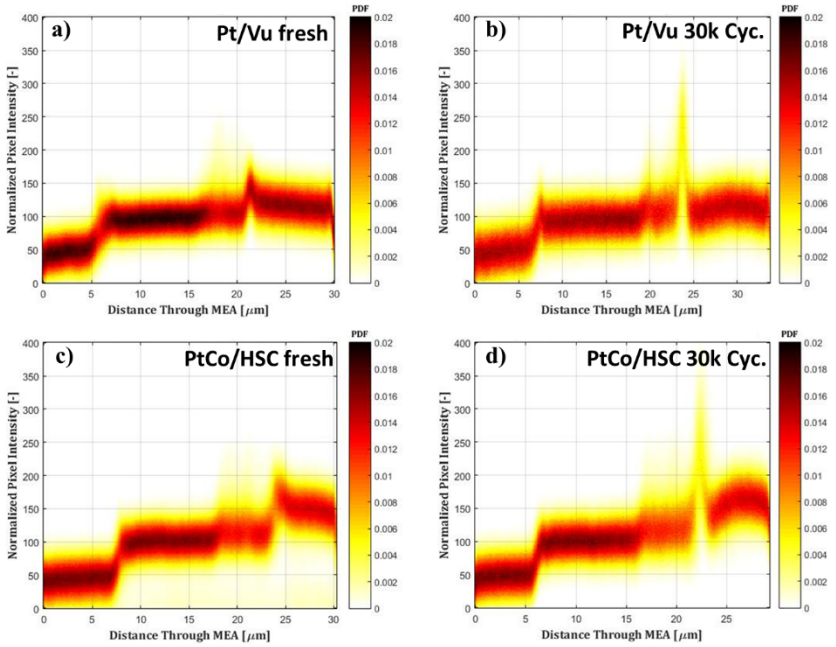

Figure 1.8: Slice intensity (ABS) distributions for a) Pt/Vu-fresh b) Pt/Vu-30k cycles c) PtCo/HSC-fresh and d) PtCo/HSC-30k cycles MEA samples. Note the widening of the PDF at the CCL/PEM interface for the cycled samples [56]. Used with permission from the Journal of Power Sources ©2020.

1.3.4 Combined Electrochemical/Nano-CT Analysis

The impact of the dissolution and reagglomeration of the Pt results in reduced ECSA, as shown in Figure 1.2. Due to the relative lesser loss of Pt from the PtCo/HSC samples, we do not see as much of an impact on the activity of the catalyst compared to the Pt/Vu samples, as shown in the activation regions of the polarization curves of Figure 1.3. The Pt/Vu lost 75% of its initial ECSA after the AST, leaving very little Pt surface area available for the ORR reaction. This led to an increase in the local transport resistance-related losses, as discussed in previous studies [30, 63]. Although the decay of the Pt/Vu 30k polarization curve is quite linear and is analogous to cases with increased ohmic resistance, this is not the case. This linearity is quite common for CCLs with low available Pt area (low Pt loading and/or low ECSA) [64].

On the other hand, ECSA loss was relatively small after the AST cycling for the PtCo/HSC sample. The polarization curve behavior was also quite different from Pt/Vu, only showing significant loss at high current densities. This may be explained by the loss in macroporosity shown in 1.5c, which could contribute to increased transport losses. As mentioned previously, the loss in macroporosity of the HSC support is somewhat surprising as it has never been confirmed with confidence. Other more common techniques, including cross-sectional optical imaging and TEM often introduce concerns about small section sampling and/or artifacts from sample preparation, lending uncertainty, whereas the larger sample volume of the LFOV nano-CT method is capable of capturing carbon support degradation over a

more representative volume without the sample preparation/artifact concerns. Some potential causes of the macroporosity loss include carbon oxidation and crushing/rearrangement resulting from membrane swelling and cell compression [60, 61]. While some previous studies suggest carbon oxidation of HSC to be minimal under these operating conditions, more work is needed to elucidate the impact of cycling on the structure of HSC supports.

1.4 Conclusion

In this study, we analyzed the degradation of two Pt-based CCLs using electrochemical characterization and a dual ZPC and ABS imaging technique featuring our laboratory-scale nano-CT imaging facility. The combination of electrochemical characterization and ex-situ imaging allowed for a comprehensive analysis of MEA-scale degradation processes. We used the ZPC data to characterize the change in large-scale void features or macroporosity in the range of 192-700 nm equivalent pore diameter resulting from catalyst AST cycling. We found that the AST cycling had little impact on the Vu but caused a significant reduction in the macroporosity of the KetjenBlack HSC support, corresponding to the mass transport losses shown in the performance characterization of the PtCo/HSC sample. We used the ABS data to quantify the degradation of the Pt-based catalyst in terms of the Pt distribution within the MEA. After the AST cycling, we witnessed the formation of a Pt band at the interface of the PEM and CCL and a corresponding Pt depletion trough near the PEM/CCL interface for both the Pt/Vu and PtCo/HSC samples. However, the Pt distribution signal showed that the percentage of Pt lost to the band was more significant for the Pt/Vu sample compared to the PtCo/HSC sample, which is consistent with the ECSA measurements and performance losses observed for the Pt/Vu sample during the electrochemical characterization.

In addition to the characterization of the state-of-the-art CCLs, we also demonstrated the effectiveness of our nano-CT method for analyzing CCL degradation on a representative MEA scale. This high-throughput analysis technique allowed us to evaluate the above-mentioned degradation mechanisms on a larger scale than has been previously reported and demonstrates a valuable evaluation technique for characterizing and comparing the degradation of future state-of-the-art CCLs.

Chapter 2

Contaminant Cation Effect on Oxygen Transport Through the Ionomers of Polymer Electrolyte Membrane Fuel Cells

2.1 Motivation

As the Pt catalyst loading is reduced in the cathodes of PEMFCs either intentionally for the sake of cost or through ECSA loss, the total number of accessible catalytic sites or Pt area is reduced, and the O_2 flux through the thin films of ionomer in the CLs becomes higher and more concentrated. This has resulted in a mass transport limited current caused by high local R_{O2} ($R_{O_2}^{Pt}$), as illustrated by previous works [30, 65]. These high $R_{O_2}^{Pt}$'s result in lower current densities and lower power output, preventing PEMFC developers from further reducing the amount of Pt. Compounding this already substantial performance reduction, contaminant cations have been shown to decrease the limiting current density of PEMFCs, which is thought to be partially the result of an increase in the local resistance [33, 34]. These contaminant cations can be introduced to the ionomer by unstable alloy catalysts like PtNi or PtCo [20, 33], environmental sources such as road salts (NaCl, $CaCl_2$, etc.) or water contaminants, or from cation sources intentionally added to PEMFCs, such as the cerium (Ce) used as a radical scavenger inside the membranes of PEMFCs.[66] These contaminant cations have been shown to preferentially exchange with the protons in the ionomer, preventing the ionomer's sulfonate groups from conducting protons and inhibiting O_2 transport within the cathode catalyst layers (CCLs) [33, 43, 44]. While significant efforts have been made to understand the role of these contaminant cations in reducing proton conductivity, little has been done to quantify or understand their effects on the O_2 transport through the ionomer in CCLs.

While the literature on the primary cation of our study (Co^{2+}) is scarce in terms of O_2 transport effects, some works [33, 41, 43, 44, 67] have captured the effects of similar cations on the water content and structure of contaminated ionomers. Their results have indicated reduced water uptake for contaminant cation-form membranes, with lesser uptake witnessed

for larger radius cations [41, 68, 69, 70]. This water loss is significant, due to the well-established conclusion that the O_2 permeability of ionomer membranes is highly dependent on the water content. [35, 36, 37] Thus, any reduction in the ionomer's water content would cause fuel cell performance losses due to lower O_2 permeability of the membranes of the CCLs.

Another relevant hypothesis was made by others [14, 40, 41], based on the observed increase in modulus (stiffness) for contaminant cation-form ionomers. Their results indicate the establishment of cross-links between sulfonate groups within the hydrophilic domains of the ionomer for higher valency cation-form membranes as well as stronger ion pairing between the cations and the sulfonate groups [14, 41]. This enhanced cross-linking and ion pairing is thought to be significant, due to the suspected increase in hydrophilic domain tortuosity, which would result in longer diffusion lengths in addition to the reduced water contents of the ionomer.

The purpose of this work is to quantify the effects of cation contamination of the ionomer used in CCLs, in terms of their R_{O2}. Cobalt (Co^{2+}) was selected as the primary cation contaminant in this study, due to its demonstrated ability to boost the catalytic performance when alloyed with Pt [20, 21]. While these PtCo alloys meet the 2020 DOE targets for performance in terms of beginning of life mass activity and total platinum group metal loading [30], extensive testing has indicated significant performance losses for cycled stacks due to the presence of leached Co^{2+} in the ionomer.[33, 34]

We also performed experiments with several other cations frequently encountered in PEMFCs. Nickel (Ni^{2+}) was chosen, for the same reason as Co^{2+}; it is used as an alloying element to boost catalytic activity [21]. Ce^{3+} was chosen, due to its use as a radical scavenger in the membrane and demonstrated (negative) effect on O_2 transport in PEMFC CCLs.[71, 72] The remainder of the cations tested (Li^+, Na^+) were studied to determine the effects of monovalent cations, as opposed to divalent cations like Co^{2+} and Ni^{2+}, and trivalent Ce^{3+}. These cations gave us an adequate study group from which to analyze the effects of valency, ion pairing, hydration state, and contamination level.

In an earlier study, we successfully developed an apparatus capable of measuring R_{O2} as a function of ionomer membrane thickness.[65] We found that the resistance was linearly proportional to the membrane thickness in the range of 50 to 2000 nm. In the current study, we use a similar apparatus to study the R_{O2} as a function of cation content and cation specie. We discuss how R_{O2} changes with cation poisoning through stronger ion pairing, cross-linking, and reduced water uptake. We then discuss how these results can be applied to the effects observed in an operating fuel cell.

2.2 Experimental

In order to measure the distinct effect of contaminant cations on O_2 transport through the PFSA ionomer, we had to isolate the O_2 transport losses from the proton conduction

losses and cation accumulation, which is difficult to accomplish when analyzing contaminated MEAs. In addition, we needed to eliminate the confinement and interfacial effects found in CCLs' ionomer films [18, 19] and the gradients in contaminant cation concentration in polarized MEAs.[33, 47, 48] Therefore, we designed a test cell utilizing an unsupported (no interfacial or confinement effects) and non-polarized (no proton conduction current or contaminant concentration gradient) ionomer membrane. The samples were prepared as described in the following section and were then tested as described in the Experimental Setup and Testing Procedure sections.

2.2.1 Ionomer Contamination Procedure

We prepared ionomer membrane samples (Nafion N117, Ion Power, New Castle, DE) contaminated with Li^+, Na^+, Ni^{2+}, Co^{2+}, and Ce^{3+} cations using a method similar to that of Greszler et al. [33] The samples were cut from an as-received sheet of Nafion N117 PFSA membrane and purified by boiling for one hour in a 3% hydrogen peroxide (Certified, Fisher Scientific, Waltham, MA) solution to remove contaminants and impurities. Next, they were soaked for another hour in near-boiling de-ionized (DI) water to remove the hydrogen peroxide and then boiled for one hour in 0.5 M sulphuric acid (Reagent Grade, Sigma Aldrich, St. Louis, MO) to re-protonate the samples. Lastly, they were soaked for one hour in near-boiling DI water and then stored in DI water.

2.2.1.1 Intermediate Cobalt Contamination Process

The purified membrane samples were contaminated in batches of 4 using aqueous solutions of cobalt nitrate (Reagent Grade, Sigma Aldrich, St. Louis, MO) and nitric acid (Reagent Grade, Sigma Aldrich, St. Louis, MO) to vary the Co^{2+} and proton concentrations. The Co^{2+} concentration in the solution ranged between 0 and 0.22 M and the proton concentrations were varied between 0 and 3.14 M, depending on the target Co^{2+} concentrations in the samples. We soaked the membrane samples for at least two days, replacing the solution after the first day to ensure the exchange solution would not be cation depleted to the point where the exchange would be incomplete. The samples were then rinsed in DI water and dried prior to being humidified and analyzed in the R_{O2} test cell. The levels of Co^{2+} contamination were measured using inductively coupled plasma optical emission spectroscopy (ICP-OES) (RJ Lee Analytical Chemistry Group, Pittsburgh, PA) and the resulting Co^{2+} exchange isotherm is presented in Figure 2.1. Note that the proton fraction, ξ, has been defined by Greszler et al. [33] as:

$$\xi = \frac{c_{H^+}}{2(c_{Co^{2+}}) + c_{H^+}} \tag{2.1}$$

where c_{H^+} and $c_{Co^{2+}}$ are the concentrations of protons and cobalt in the sample, respectively.

2.2.1.2 Cation Comparison Study Contamination Process

We prepared aqueous solutions of lithium sulfate, sodium sulfate, nickel sulfate, cobalt sulfate, and cerium sulfate (Reagent Grade, Sigma Aldrich, St. Louis, MO) for the cation

comparison experiments, similar to the Co^{2+} exchange process but without the nitric acid. The solution concentrations ranged from 0.20 to 1.60 M. For all cation types except Ce^{3+}, we accomplished full exchanges, again verified by ICP-OES. For the Ce^{3+} samples, we accomplished only a 5% exchange, due to the limited solubility of cerium sulfate, which prevented the Ce^{3+} cations from being absorbed by the membrane samples.

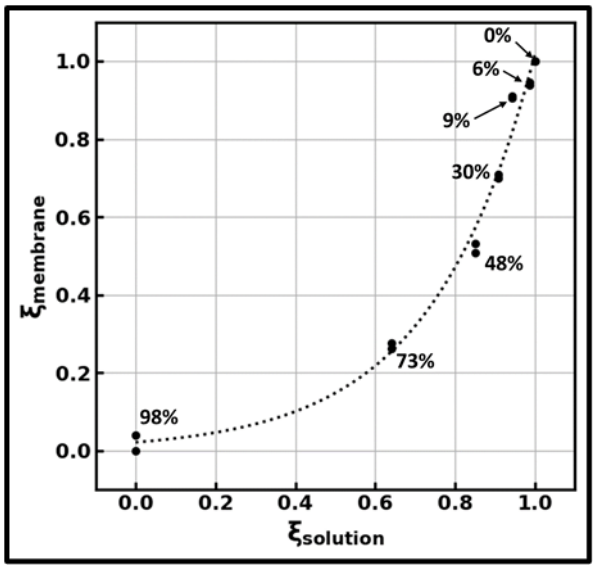

Figure 2.1: Co^{2+} exchange relation from solution to membrane, where ξ is the proton fraction from Eq. 2.1. Note that the percentages shown are the average Co^{2+} levels of 2 samples.[73] Used with permission from the Journal of the Electrochemical Society ©2019.

2.2.2 Experimental Setup

To create an R_{O2} measurement cell, we modified existing commercial fuel cell hardware (Dual Area Fuel Cell Fixture, Scribner and Associates, Southern Pines, NC), similar to that of our prior work in Liu et al.[65] The cell consisted of a modified cathode flow plate and sample holder with a free-standing, electrically isolated membrane sample, and a fuel cell MEA (4 cm^2 active area) functioning as an O_2 sink and O_2 transport rate monitor. The anode side of the Scribner cell remained unchanged. The R_{O2} test cell's design is shown in Figure 2.2 This setup allowed for the bulk measurement of the R_{O2} of cation contaminated membrane samples, while eliminating the confinement, interfacial, conductivity, and electrical gradient effects found in operating MEAs. Thus, the measurements from this setup provided the pure, bulk R_{O2} effects of cation contaminants and allowed valuable insight into the mechanisms of the observed decrease in O_2 transport for cation contaminated MEAs.

Once the contaminated membrane sample was installed, we supplied air to the top of the membrane sample and operated the test cell's MEA under its limiting current regime (0.4 and 0.3 V). This allowed us to drive the O_2 concentration to roughly zero below the sample as shown in Figure 2.3, enabling the application of a Faradaic Ohm's Law analogy for the

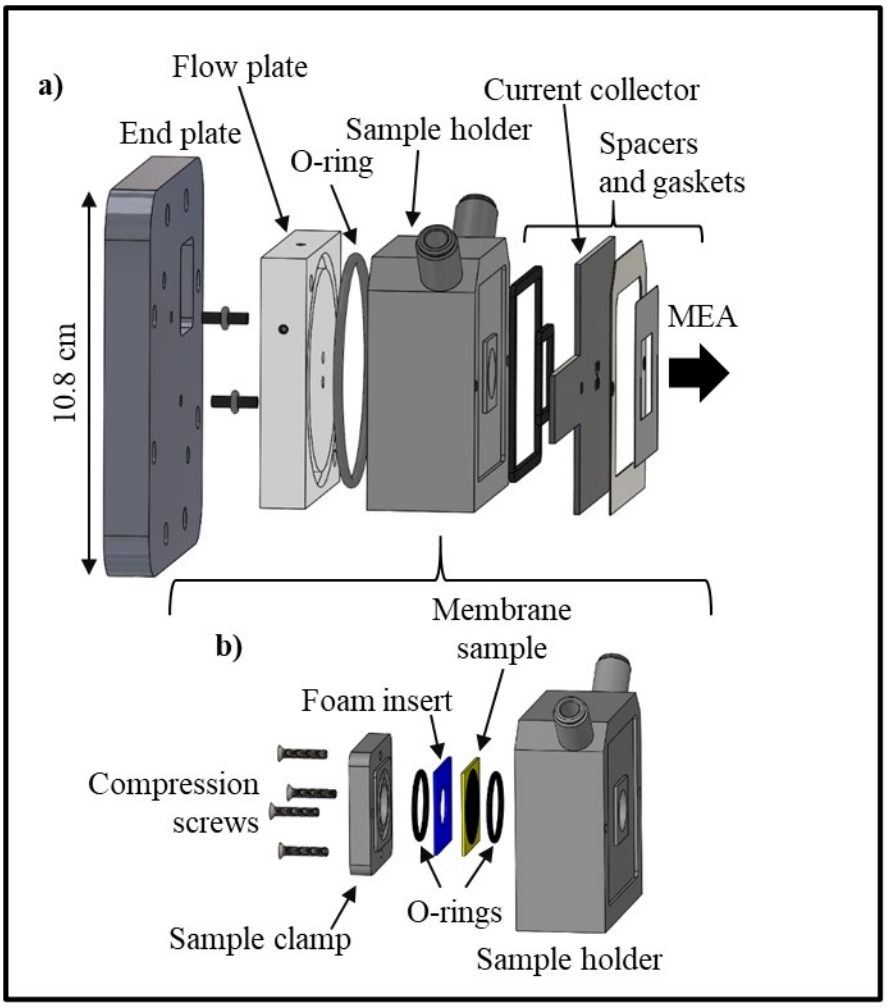

Figure 2.2: a) Exploded view of the cathode side of the test cell assembly. The anode side of the assembly remained unchanged from the fuel cell hardware. b) Exploded view of the sample holder assembly. Note that the foam insert was used to prevent condensation buildup on the sample during testing. The diameter of the sample's test area is 14 mm.[73] Used with permission from the Journal of the Electrochemical Society ©2019.

R_{O2}:[65]

$$R_{O_2} = \frac{nFAc_{O_2,a}}{I} \tag{2.2}$$

where n is the number of electrons transferred per mole of fuel (4 for O_2, in this case), A is the area of the membrane sample, F is Faraday's constant, $c_{O_2,a}$ is the O_2 concentration above the sample from the feed gas, and I is the current produced by the MEA, which served as the O_2 sink.

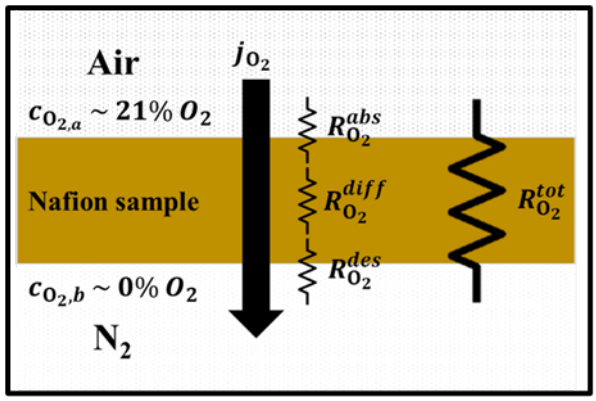

Figure 2.3: R_{O2} resistance network from the cathode stream to the O_2 depleted zone below the membrane sample. Note the known concentrations of O_2 above and below the sample, which are used in Eq. 2.2.[73] Used with permission from the Journal of the Electrochemical Society ©2019.

While this approach to measuring the R_{O2} includes both the non-equilibrium absorption resistance at the gas/membrane interface, $R_{O_2}^{abs}$, in Figure 2.3 as well as the non-equilibrium desorption resistance at the membrane/gas interface, $R_{O_2}^{des}$, in Figure 2.3), these resistances have been shown to be negligible compared to the diffusive resistance through the membrane, especially for bulk ionomer membranes.[65] Also, the R_{O2} due to diffusion through the O_2 depleted zone from the bottom of the sample to the CCL of the test cell's MEA has been calculated to be several orders of magnitude smaller than the resistance due to diffusion through the uncontaminated membrane sample. Thus, the total resistance $R_{O_2}^{tot}$ in Figure 2.3 measured by our method is dominated by the R_{O2} due to diffusion through the membrane sample, $R_{O_2}^{diff}$, in Figure 2.3.

2.2.3 Testing Procedure

We tested the samples by clamping them in the sample holder assembly as shown in Figure 2.2b, and then assembling the remainder of the test cell shown in Figure 2.2a. The cell was heated to 80°C at 1 atm, and the relative humidity (RH) of the cathode and anode streams were controlled using the humidifier temperature. Two different experimental procedures were used: one for the intermediate Co^{2+} loading experiment and one for the cation

comparison experiment. For the intermediate Co^{2+} loading experiments, the anode's RH was held at 40%, and the cathode's RH was varied from 40% to 80% to reflect low (40%), medium (60%) and high (80%) water activities in the contaminated membrane samples. For the cation comparison experiments, the relative humidities of the anode and cathode were varied together between 40% and 100% RH to test the effects of low, medium, high, and fully humidified membrane samples.

We performed the experiments by holding the test cell's MEA at 0.4 and 0.3 V, which were established as the limiting current voltages in preliminary experiments. A background current was established using N_2 on the cathode, and pure H_2 on the anode. Once the background current stabilized, we switched the N_2 supply to air (21% O2) and again held the test cell at 0.4 and 0.3 V until the current stabilized for each voltage. This allowed for the current due to O_2 permeation through the membrane sample to be determined by evaluating the difference between the N_2/H_2 background and air/H_2 currents. We used the current from the 0.3 V holds to calculate the R_{O2} as described in Equation 2.2. During measurements, we would occasionally observe irregular disturbances, especially at low MEA RH, which we attributed to MEA instability in our test cell. These sections of data were omitted from the subsequent current averaging methods used to find the background and O_2 permeation currents. Figure 2.4 shows an example of the raw current data from the testing procedure, along with the difference in currents used for the resistance calculation.

2.2.4 MEA O_2 Limiting Current Testing

The local R_{O2} of the MEAs was obtained via the O_2 limiting current method described in previous works.[64, 74] Specifically, 18 µm thick PFSA membranes with internal reinforced layers were doped with given levels of Co^{2+} following the procedure given previously. MEAs with an active area of 5 cm^2 were prepared by hot pressing the Co^{2+}-doped membrane with electrode decals at 295°C and 5000 lbs for two minutes. The cathodes were 10 wt% Pt/Vu with a loading of 0.05 mg_{Pt}/cm^2. The cathode thickness was measured to be 10 µm by SEM. All anodes were 20 wt% Pt/GrC (graphitized carbon) with a loading of 0.05 mg_{Pt}/cm^2.

Low-pressure drop flow plates were used to enable operation at high flows (stoichiometry of >15) without significant down-channel pressure drop or gas composition variation through the cell. The limiting current measurements were performed at 80°C and 62% RH with three dry mole fractions of O_2 (0.01, 0.02, and 0.04) at four different pressures: 110, 150, 200, and 300 kPa. The measurements were collected at sub-saturated conditions such that liquid water effects could be neglected. Diluted O_2 concentrations were chosen to reduce the limiting current density and keep the product water in a vapor form, as well as simplification of the transport model by enabling the use of Fick's law. A minimum of three replicates were tested for each level of cation.

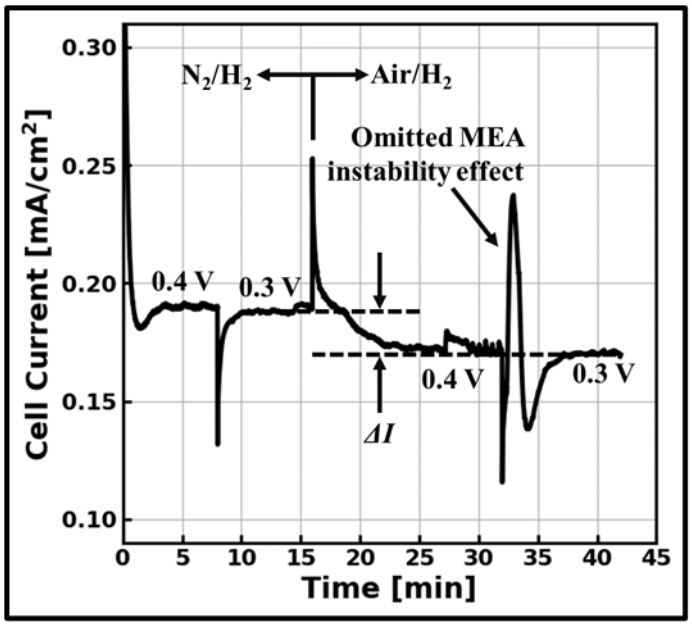

Figure 2.4: Raw current data from the experimental procedure. The current difference (ΔI) between the N_2/H_2 and air/H_2 environments at 0.3 V represents the current produced due to O_2 permeation through the ionomer.[73] Used with permission from the Journal of the Electrochemical Society ©2019.

2.3 Results

First, we present the results for the Co^{2+} contaminated membranes with the contamination levels shown in Figure 2.1. We tested at least 3 membrane samples per contamination level, and the data for each water activity (low, medium, high) was averaged once a steady state current was achieved. The data for each contamination level is shown in Figure 2.5.

Figure 2.5 shows that while the R_{O2} increases with decreasing water activity, the R_{O2} increase is significantly higher with increasing Co^{2+} contents. This was supported by the MEA testing results [40] that observed an increase in R_{O2} with Co^{2+} cation contamination, especially under dry operation. Another study (19) showed an increase in moduli for cation-exchanged membranes exposed to low activity water, indicating that the increase in their modulus and our R_{O2} could be related to the increased interactions between the sulfonate groups and cations for conditions where less water is available to shield the cation/anion pair interactions, as studied by others.[75, 76, 77, 78, 79, 80]

Further examination of the R_{O2} increases shows that there was little change in R_{O2} for Co^{2+} contents below 30% and that the high Co^{2+} contamination (48% and above) results were consistent with the fully contaminated results. This bimodal grouping of the R_{O2} results is further examined in Figure 2.6, where we present the R_{O2} as a function of the Co^{2+} contamination levels. Between the indicated low and high contamination regimes, a sharp increase in R_{O2} is present, which suggests a critical concentration (ca. 50% exchange) where

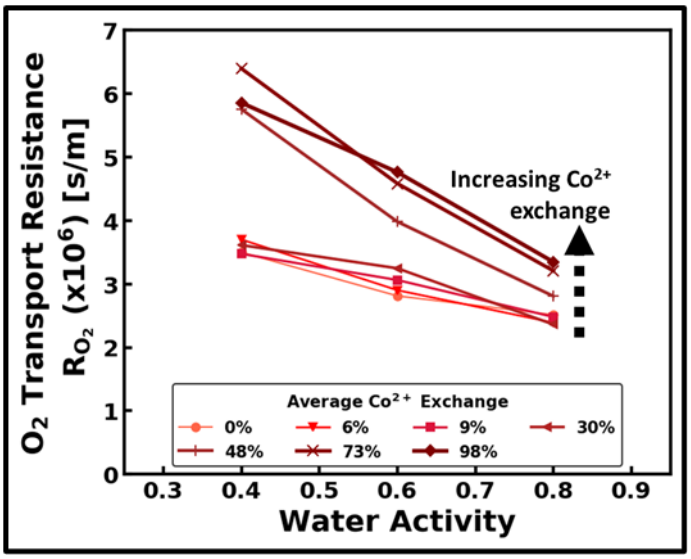

Figure 2.5: Averaged R_{O2} results for all Co^{2+} contamination levels over a range of water activities at 80°C and 1 atm. Note that the Co^{2+} exchange percentage reflects the percentage of sulfonate groups occupied by Co^{2+} cations.[73] Used with permission from the Journal of the Electrochemical Society ©2019.

the Co^{2+} cations could begin to cause significant structural changes to the membranes' hydrophilic domains, similar to the effects characterized by others.[41, 69, 81] The hydration state of the membranes plays a role in suppressing these structural changes, as illustrated by the difference in the R_{O2} increase between the low and high contamination regimes for each hydration state.

To further explore and decouple the phenomena affecting the membrane samples' hydrophilic domains, we performed experiments with fully exchanged membranes using cations of varying radius and valency under various water activities. The results from this study are shown in Figure 2.7. We acknowledge the importance of water uptake on the membranes' hydrophilic domain structures, but due to the lack of uptake data available for our cationic-form membranes at 80°C (or a similarly high temperature), we have decided to plot Figure 2.7 only as a function of water activity and not membrane water content.

The data in Figure 2.7 shows several trends. First, the divalent and similarly sized Ni^{2+} and Co^{2+} cations had much the same effect on O_2 transport, as expected. However, the results for the monovalent Na^+ and Li^+ samples differ significantly between each other. The Na^+ results were similar to the dual valency Co^{2+} and Ni^{2+} results, whereas the Li^+ was more similar to the proton form membranes under high water activities (80 and 100% RH) and the Na^+, Co^{2+}, and Ni^{2+} results at low water activities (40% RH). However, it is important to note that due to the valency of Ni^{2+} and Co^{2+}, the concentration of these two cations is half that of Na^+ and Li^+, per electroneutrality in the samples. The 5% Ce^{3+} exchange had little to no impact on the R_{O2}, validating the uncontaminated (proton form) base case and demonstrating the R_{O2} impact of a Ce^{3+} loading consistent with its addition to the

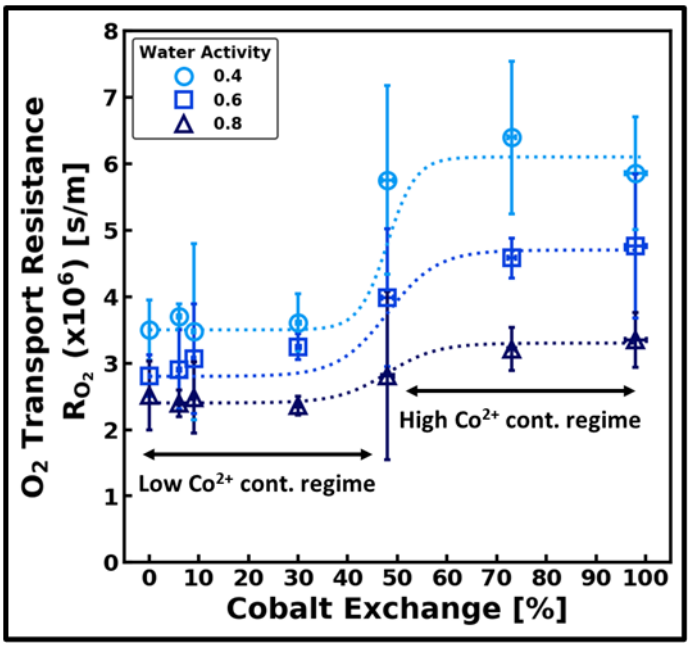

Figure 2.6: Average R_{O2} as function of sample Co^{2+} content for each water activity tested at 80°C and 1 atm. The vertical error bars correspond to a 95% confidence interval on the averages of the R_{O2} data, and the horizontal error bars correspond to the standard deviation of the ICP-OES measurements. The dotted sigmoidal functions are shown to guide the eye.[73] Used with permission from the Journal of the Electrochemical Society ©2019.

membrane for radical scavenging purposes.[71, 72]

The data illustrated and discussed in the previous figures and paragraphs provided a basis from which we can compare the effects of each R_{O2} mechanism: reduced water uptake, ion pair strength, and ionic cross-linking. In the following paragraphs, we will use our experimental results to postulate on the structural changes of ionomer membranes contaminated with cations of various radius and valency and their effect on overall fuel cell performance.

The comparison between the Na^+ and Li^+ form membranes (Figure 2.7) allowed for the separation of the reduced water uptake effect. As before, the concentration of protons, Li^+, and Na^+ are all the same in the membrane and no cross-linking is possible. The difference in R_{O2} results between the Li^+ and Na^+ form membranes can then be attributed to the effects of a reduction in water uptake, since Na^+ causes a greater reduction in water uptake than Li^+.[41, 68, 69, 70] We suspect that the reduced water uptake has two effects: an overall reduction in hydrophilic domain volume and stronger ion pairing from reduced shielding. Both of these could impair the transport of O_2 by increasing the tortuosity of the hydrophilic domain, leading to the decrease in O_2 transport seen for lower water content membranes.[35, 36, 37] Figure 2.8 illustrates this increase in tortuosity due to reduced water volume and stronger ion pairs for monovalent cations like Na^+.

Studying the results of the membranes in proton and Li^+ form allows for the evaluation of

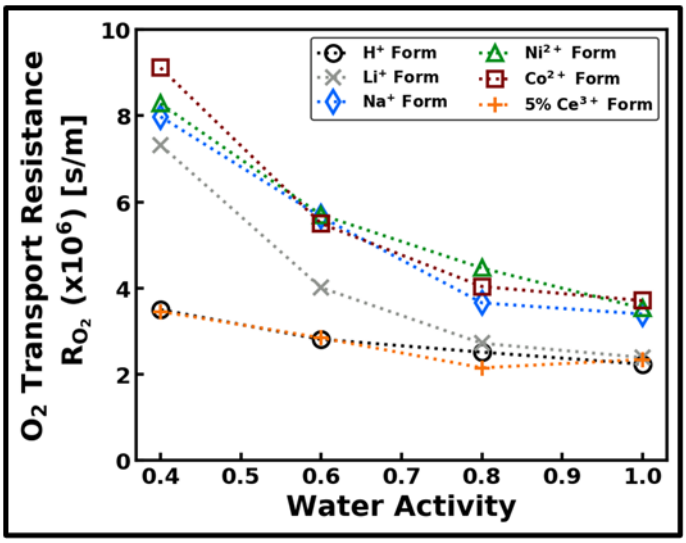

Figure 2.7: R_{O2} of various cation-form Nafion N117 membranes over various water activities at 80°C and 1 atm. [73] Used with permission from the Journal of the Electrochemical Society ©2019.

the impact of ion pair strength. Using the proton form membrane as a baseline (Figure 2.7), the increase to the Li^+ results is largely the result of stronger ion pairs, as Li^+ is known to have little impact on the water uptake of the membrane.[41, 68, 69, 70] In addition, it cannot cause cross-linking due to its monovalency. As a result, the difference can be attributed to stronger ion pairs. This is further supported by the magnitude of the change in R_{O2} for low and high water activities. At low water activity, the R_{O2} increases by nearly two-fold, and at a fully saturated activity, the R_{O2} is not impacted. At lower hydration states where less water exists to dissociate the cations, we expect the ion pair interactions to become stronger, leading to the increase in modulus for Li^+ form membranes shown by other works [40, 41] and the corresponding compression of the hydrophilic domain leading to increased tortuosity for the O_2 diffusion path.

Since the Li^+ and divalent cation form ionomers have comparable water uptakes [41, 68], we used the Li^+, Ni^{2+}, and Co^{2+} data sets to compare the effect of cross-linking. The Co^{2+} and Ni^{2+} membranes have half the concentration of cations that the Li^+ membranes have, yet their impact on O_2 transport is much greater, at all water activities greater than and equal to 0.6. This change is due to the cross-links that form between Ni^{2+} and Co^{2+} and the sulfonate groups. We postulate that the multivalent cations' pairing with multiple sulfonate groups causes large-scale deformation of the side chains and backbones of the PFSA polymer, resulting in a severely compressed hydrophilic domain and an increase in tortuosity of the O_2 pathway, as illustrated in Figure 2.9. The change in R_{O2} due to cross-linking is comparable to that caused by the dehydration and stronger ion pairing caused by Na^+ and the stronger ion pairs caused by Li^+ at low water activity.

The intermediate Co^{2+} loading study allowed us to examine these structural phenomena as

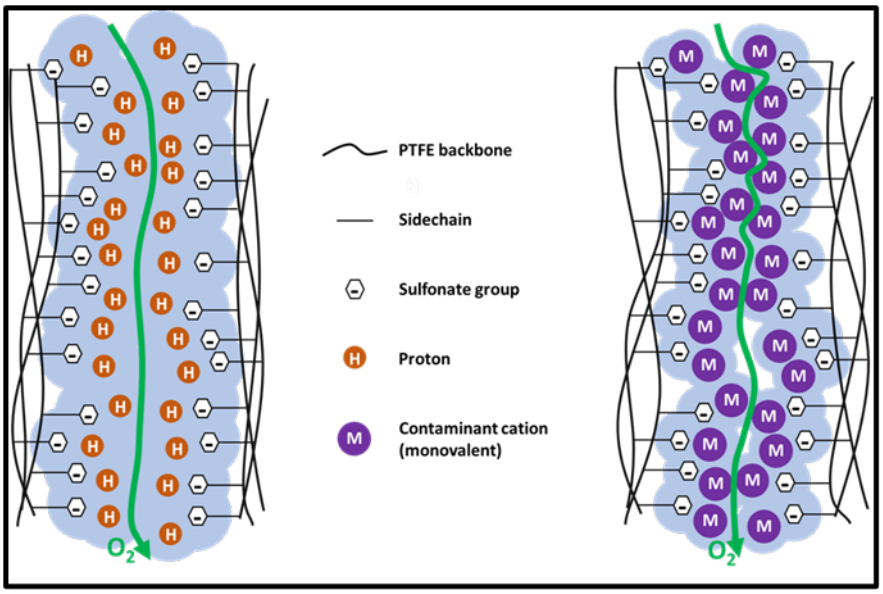

Figure 2.8: Fully humidified proton-form ionomer (left) versus fully humidified monovalent contaminant cation-form ionomer (right). Note the distortion of the PTFE backbone of the contaminant cation-form ionomer due to the stronger ion pairs (i.e. the distance between the cations and the sulfonate groups).[73] Used with permission from the Journal of the Electrochemical Society ©2019.

a function of cation level in the membrane. From the data we presented in Figures 2.5 and 2.6, we show that distinct contamination regimes exist above and below a contamination threshold, where the impact of the contaminant cations on the R_{O2} is large and small, respectively. For Co^{2+}, we showed that this threshold is near 50%, as shown in Figure 2.6. At this exchange level, we suggest that the hydrophilic domain structure undergoes significant distortion, leading to longer diffusion paths for O_2 and a corresponding increase in the R_{O2}. In addition, we show that increased hydration states can suppress these effects by weakening the ion pair strengths and allowing for expansion of the hydrophilic domains.

The last effort of our work sought to evaluate the impact of Co^{2+} on the R_{O2} of a real fuel cell cathode using the limiting current test described in (27, 28). This series of experiment were performed at different gas pressures to differentiate the pressure dependent and pressure independent components of the R_{O2}. As expected, the pressure dependent R_{O2} (primarily from the gas diffusion media), were unaffected by the Co^{2+} level. Knudsen diffusion in the microporous layer and electrode [64] was accounted for within the pressure independent resistances, leaving only the resistance local to the Pt surface $R_{O_2}^{Pt}$. Figure 2.10 summarizes this measured $R_{O_2}^{Pt}$ as a function of Co^{2+} exchange level.

It is clear that increased Co^{2+} levels result in increased $R_{O_2}^{Pt}$, and that the resistance appears to reach a plateau. MEAs with higher Co^{2+} levels were also tested, but unfortunately, high electrode proton resistance caused a non-linear limiting current vs O_2 concentration correlation; hence, this data was omitted. While the true origin of the $R_{O_2}^{Pt}$ remains unclear, the

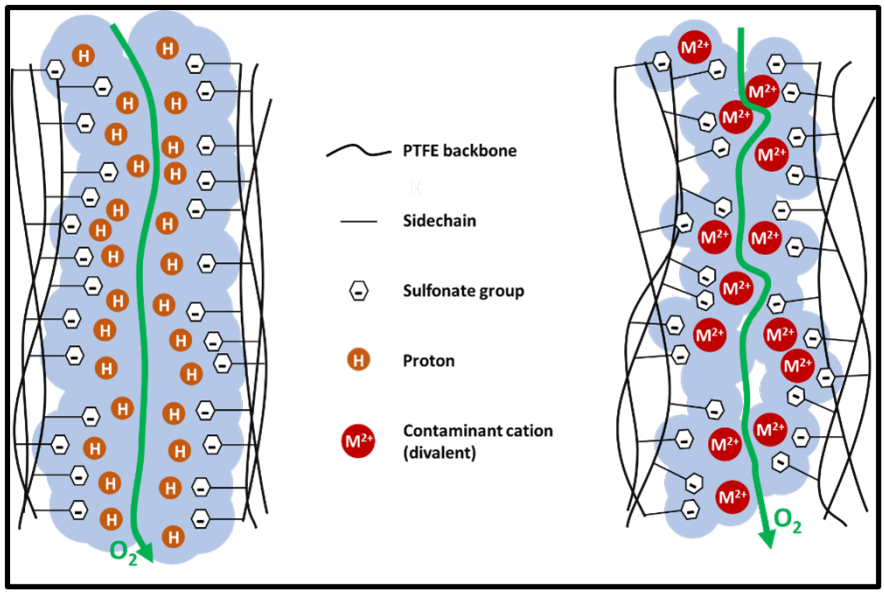

Figure 2.9: Fully humidified proton-form ionomer (left) versus fully humidified divalent contaminant cation-form ionomer (right). Note the distortion of the PTFE backbone of the contaminant cation-form ionomer due to the cross-linking of adjacent sulfonate groups.[73] Used with permission from the Journal of the Electrochemical Society ©2019.

resistance has been shown to be strongly related to how the ionomer interacts with the Pt surface.[19] Therefore, it is understandable for contaminant cations to affect the $R_{O_2}^{Pt}$.

Comparing the $R_{O_2}^{Pt}$ with the R_{O2} results in Figures 2.5 and 2.6 shows that the increase in resistances occurs at a much lower Co^{2+} level for $R_{O_2}^{Pt}$. To understand this, one must recognize the differences between the two cases. First, the limiting current test requires polarization of the MEA, resulting in Co^{2+} migration and accumulation in the cathode. As a result, the Co^{2+} levels in the cathode are higher than the nominal doped levels. Second, the ionomer in the electrode is very thin (<10 nm) and is in contact with either the Pt surface or carbon, while in the bulk membranes it is much thicker (>100 µm). Thinner ionomer films have a less-developed hydrophilic-hydrophobic segregated structure due to confinement effects and are more prone to the effects of contaminant cations.[17]

In a state-of-the-art fuel cell MEA, with Pt_3Co (0.1 mg_{Pt}/cm^2) and a 14 µm thick membrane, the Co^{2+} exchange is expected to be in the range of 3 to 10% throughout its life.[6] As current is applied, the electric field gradient can cause migration of cations to the cathode and the redistribution of water throughout the MEA can also cause cation concentrations to be nonuniform locally. These impact not only gas permeability, but also proton conduction and ORR activity. As shown in this work, the impact of a full or near-full Co^{2+} exchange in the CCL resulting from high current density operation can cause a significant increase of the local O_2 transport resistance.

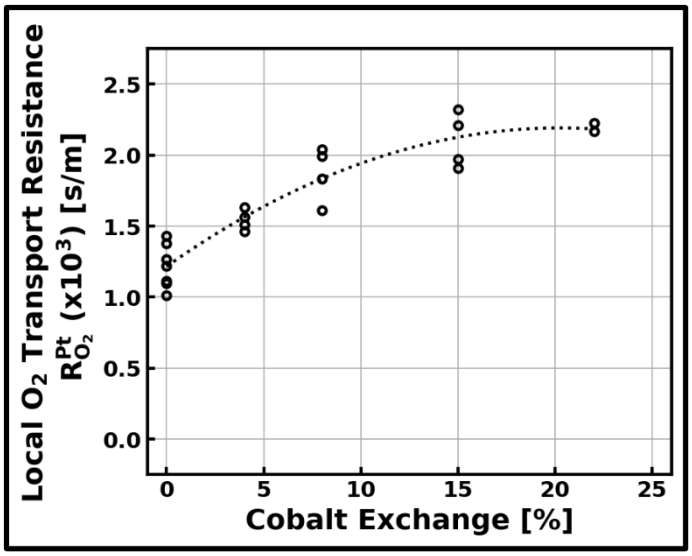

Figure 2.10: Local O_2 resistance of a Pt/Vu CCL as a function of Co^{2+} exchange in the membrane. The resistances were determined at 80°C, 62% RH. The MEA was fabricated with an 18 µm thick PFSA membrane with a 0.05 mg_{Pt}/cm^2 Pt/Vu cathode with an ionomer/carbon ratio of 0.8.[73] Used with permission from the Journal of the Electrochemical Society ©2019.

2.4 Conclusion

In this work, we successfully characterized the effects of monovalent (Li^+ and Na^+) and divalent (Ni^{2+} and Co^{2+}) cations on the O_2 transport properties of bulk ionomer membranes. We found that for full exchanges of these cations, the increase in the R_{O2} for low water activity was at least 100% and was less than 50% under saturated water activity conditions. We analyzed the O_2 transport impacts of the various cations in terms of the structural changes to the ionomer caused by reduced water contents, ion pair strengths, and cross-linking on the structure of the membrane's hydrophilic domains. We suggest that the increase in R_{O2} we observed for membranes contaminated with these cations corresponded to compression of the hydrophilic domain, resulting from dehydration, stronger ion pairing, the formation of cross-links between sulfonate groups, or a combination of these. We believe that the compression of the hydrophilic domain causes an increase in tortuosity of the O_2 diffusion path, which manifests as an increase in the R_{O2}. In addition, our intermediate Co^{2+} loading analysis indicated that a critical concentration exists where these phenomena begin to impact the membrane's hydrophilic domains. The last effort of our work demonstrated these effects (for Co^{2+}) in an operating fuel cell cathode. The results were consistent with our expectations; increasing the level of Co^{2+} exchange increases the R_{O2}, but a maximum R_{O2} exists due to Co^{2+} migration and accumulation in the cathode.

The results of this work will help inform the design process of PEMFCs as well as their operating conditions. PEMFC designers would do well to minimize the number of contaminant cations in the ionomer, to prevent full exchanges at the catalyst surfaces under high current densities, and to ensure that the fuel cells are operated under medium water ac-

tivity conditions (60% RH) or greater in order that the effects of any contaminant cations are minimized. In addition, these results provide design insights for future ionomers with less susceptibility to increased R_{O2} with cation contamination. With the knowledge of the effects of these contaminant cations on O_2 transport, we hope that they can be accounted for, allowing for a further reduction of the catalyst loading and ultimately mass-market penetration by PEMFC technology.

Chapter 3

Operando Analysis of Cesium Migration in the Catalyst Layers of PEMFCs

3.1 Motivation

As discussed previously, Pt alloy catalysts degrade during voltage cycling, leaching the transition metal alloying element into the ionomer where it becomes a mobile specie, competing with protons as they are transported under the electric field of the ionomer and accumulate at the cathode during PEMFC operation. As these mobile contaminant cations aren't consumed in any reaction, they have a protonic choking effect, essentially increasing the local ohmic resistance of the ionomer films of the CLs. In addition, contaminant cations are known to adversely affect O_2 transport as described in Chapter 2, especially at high concentrations. To mitigate these transport losses, it is first necessary to understand the process of contaminant cation migration and accumulation.

The migration process and its effect on performance have been studied extensively with modelling efforts [47, 48] and electrochemical characterization, i.e. polarization curves, limiting current analysis, etc. [33, 34, 54, 82, 83, 84]. Further, experimental works have examined the migration and accumulation of contaminant cations including cerium (Ce^{3+}) [85] and Co^{2+} [82] under the electric field of the membrane macroscopically with XRF techniques. While these efforts have indicated migration to and accumulation at the reducing electrode (cathode), the phenomena has never been confirmed within the CL of a PEMFC in-operando as we sought to do in this effort.

The focus of this work was to confirm migration of a cationic specie within a real PEMFC CL in-operando. To achieve this, we used our nano-CT facility's absorption contrast X-ray capability to monitor the change in concentration of cesium cations (Cs^+) through X-ray attenuation measurements as is common in chemical concentration analyses using the Beer-Lambert law [86, 87, 88, 89]. We also developed a model in COMSOL to corroborate our experimental setup and to estimate the diffusivity and mobility of the cation of interest, i.e. Cs^+. We chose Cs^+ due to its high atomic mass and single valency, as X-ray attenuation

increases with atomic mass and concentration.

3.2 Experimental

3.2.1 Hardware Design and MEA Fabrication

X-ray analysis of PEMFC processes in-operando is notoriously difficult due to the planar nature of MEAs, their overall thickness in relation to the attenuation length of the X-rays in MEA materials, and finally, the metallic flow plates used for gas diffusion media compression that completely prevent X-ray penetration and transmission. To circumvent these issues, we designed a modified fuel cell hardware with an elongated MEA structure sealed in Kapton with an X-ray imaging port cut into the compression plates to allow for X-rays to penetrate the CL/membrane interface of our elongated MEA.

The elongated MEA structure is shown in Figure 3.1. The flow plates and supporting hardware with a fabricated elongated MEA are shown below in Figure 3.2. The X-ray viewing port is positioned directly over the overlap between the CL and the membrane that stretches between the X-ray viewing port and the water reservoir at the bottom of the left flow plate. The two flow channels were milled into the aluminum frame and connected to gas lines with steel tubulations. Wires were routed through the center of each flow channel to the front of the flow plate where they could be connected to a potentiostat for electrochemical cycling.

The Cs^+-doped membrane was hot-pressed to a decal-backed, Vu-supported low Pt (0.1 mg_{Pt}/cm^2 loading) CL that functioned as the working electrode. Here we will use the terms reference and working electrode instead of anode and cathode, as we are dynamically switching the electrodes during the course of the experiment. The decal fabrication technique has been reported elsewhere [20] and was performed by the General Motors Fuel Cell Division in Pontiac, MI. The Pt loading was intentionally kept low to hinder the generation of H_2 during H_2 pumping, as H_2 bubbles were observed in early experiments and hindered the direct observation of contaminant cation migration. The reference electrode was not elongated like the working electrode and consisted of a high Pt content (2 mg_{Pt}/cm^2) Pt black cloth GDE (FuelCellStore, College Station, TX) compressed against the Cs^+-doped Nafion 211 strip. The Cs^+ occupation fraction (12%) was determined by ICP-OES (RJ Lee Group, Monroeville, PA). Toray paper was used as the working electrode's GDL. Silicone gaskets were used to seal around the electrodes and flow channel/diffusion media and a PTFE coated fiberglass perimeter gasket was used to ensure approximately 30% compression of the diffusion media. The front plate was sealed with Kapton and bolted to the backplate before being installed on the nano-CT sample stage and attached to the gas distribution lines and potentiostat as shown in Figure 3.3. Gold fiducials were placed at the edge of the CL/Nafion 211 strip for use in aligning the CL/Nafion strip interface in the nano-CT as well as for image registration in subsequent processing.

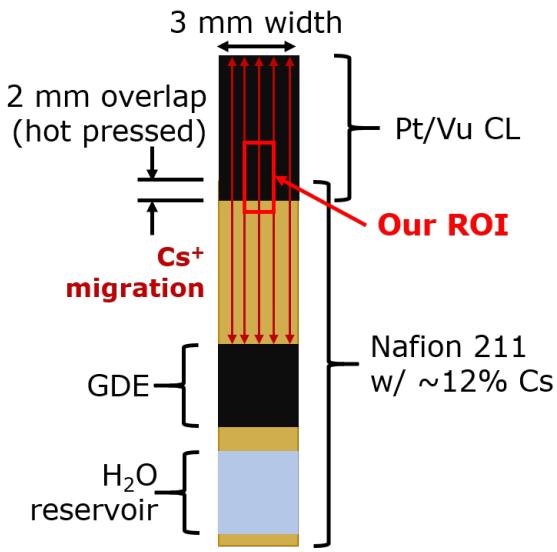

Figure 3.1: Elongated MEA geometry. Note the red box representing the X-ray region of interest, or ROI, used in the nano-CT imaging.

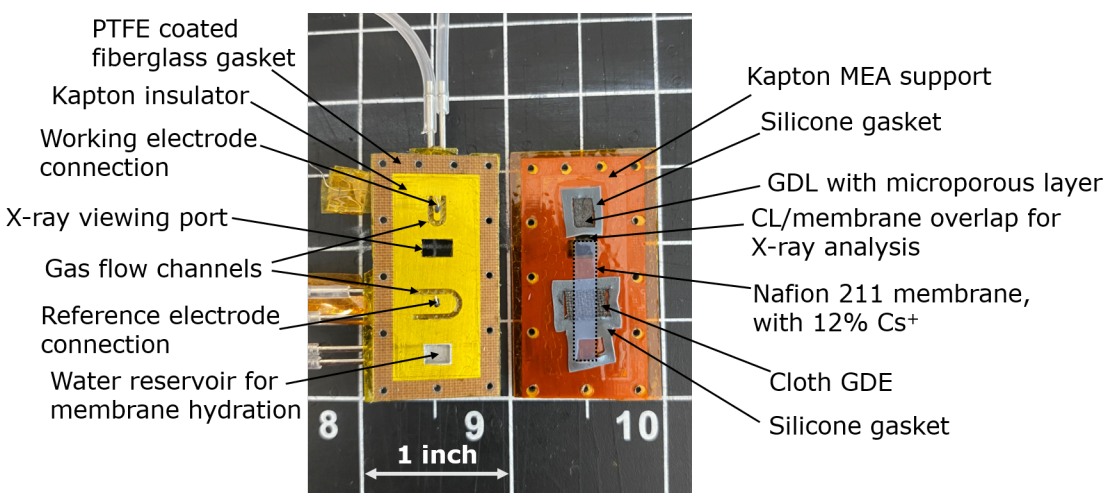

Figure 3.2: Labeled cell hardware and MEA components

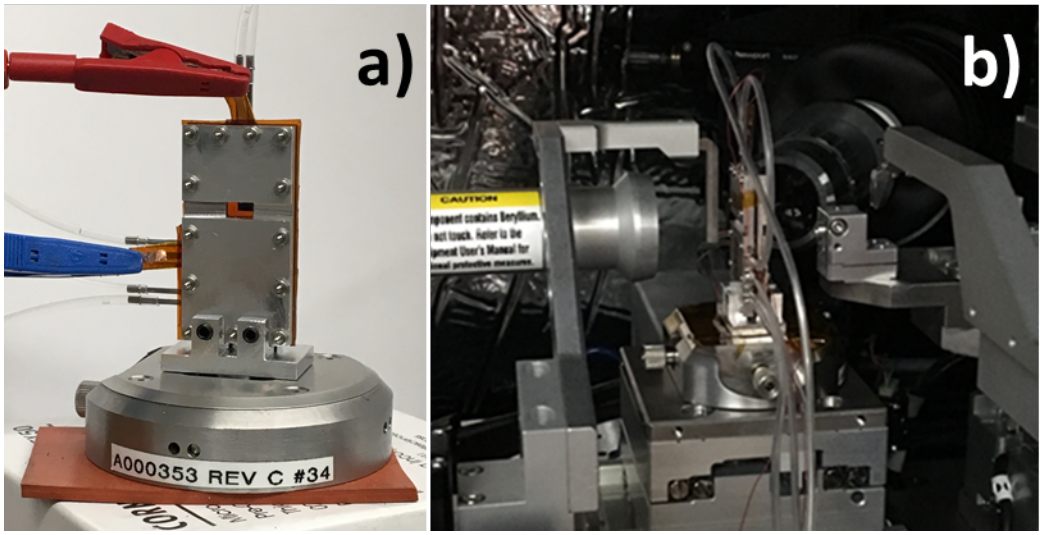

Figure 3.3: a) Assembled cell with attached electrode clips and b) installed in the nano-CT chamber with gas lines and electrode wiring.

3.2.2 Operando Analysis Procedure

The migration cell was operated under a H_2 pumping configuration at standard temperature and pressure. With the nano-CT instrument's sensitivity to temperature changes, we didn't perform analyses at elevated temperatures that could have affected the nano-CT hardware. H_2 was supplied to the electrodes in series, which allowed for the direction of the applied currents to be switched mid-experiment without manual switching of gases. The H_2 gas was slowly bubbled through a bottle humidifier at 25°C to provide the cell with sufficiently humidified gases to ensure the full hydration of the Nafion 211 strip that was in direct contact with the water reservoir, i.e. λ=22 for the Nafion strip. The gases were equilibrated for 12 hours until the OCV of the system had been reduced to near zero, i.e. all O_2 in the gas lines, electrodes, etc. had been displaced.

The Kapton-sealed X-ray window was aligned with the X-ray beam of the nano-CT, which was operated in traditional ABS mode. The interface of the CL/Nafion strip was centered in the focal length of the nano-CT by stepping the stage position in the Z-direction (forward and backward relative to the nano-CT optics) while taking consecutive images of areas with many gold fiducials. For each of these images, the standard deviation of the ABS radiograph was computed and plotted as a function of Z-position, as shown in Figure 3.4. The standard deviation increased from both directions as it approached the focal length of the nano-CT's optics, allowing us to locate our CL/Nafion overlap within the 130 μm focal length of the nano-CT.

In addition to the focal length alignment, we located the LFOV (65 µm square) X-ray beam on the topmost extremity of the Nafion strip, equidistant from the right and left edges of the CL. This location allowed X-ray access to the pure CL above the Nafion 211 strip, as shown in Figure 3.5. During the operando experiment, we took vertical mosaics of 10 radiographs,

covering 650 µm of CL length, giving us significant spatial resolution over which to perform image processing and analysis.

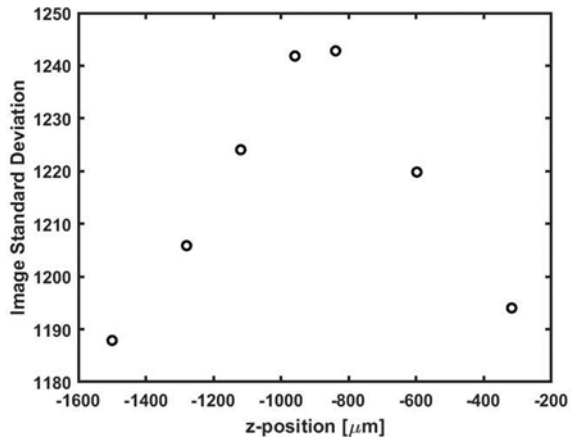

Figure 3.4: Alignment of sample in the nano-CT's X-ray focal length.

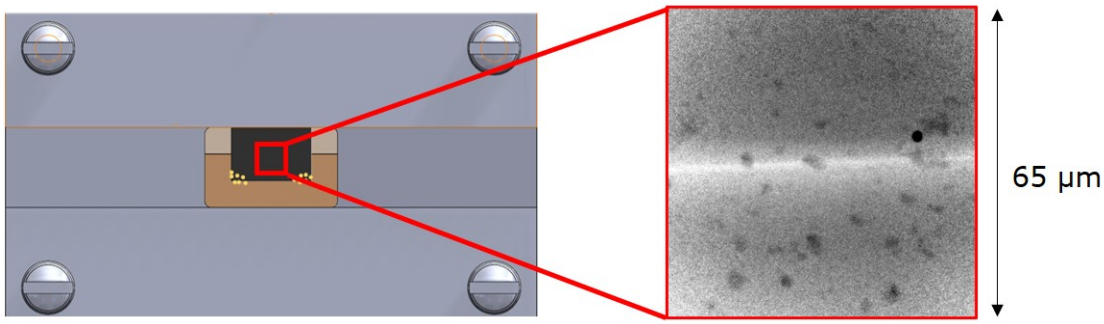

Figure 3.5: Zoomed in ABS view of CL/Nafion strip overlap within the X-ray imaging port. Note the gold fiducials on the edges of the CL in the X-ray port that were used for the alignment process shown in Figure 3.4.

Once aligned within the focal length of the nano-CT optics and equilibrated under the humidified gas supply, we began the operando imaging. A zero current (OCV) equilibration was established for one hour, followed by current pulls of 2.5 μm from the reference electrode to the working electrode and then reversed to demonstrate back-and-forth polarization and corresponding migration of the Cs^+ cations. The back-and-forth pumping relies upon reversing the electrochemical reactions, hence the use of reference electrode and working electrode instead of anode and cathode. The electrode potentials were monitored during the current pulls and the voltage was prevented from exceeding ± 2.0 V to minimize carbon corrosion and electrolysis.

During each stage of the electrochemical testing, the nano-CT collected 10 vertically stacked radiographs, each collected for 60 seconds in ABS binning 2. The nano-CT technique has

been described elsewhere [57] but it must be noted that within the scope of this analysis, we utilized only the 2D X-ray radiographs as compared to typical analyses that reconstruct 3D volumes corresponding to series of angle-varied 2D radiographs. The 60 second radiograph/10 minute mosaic imaging timescale was determined to be sufficient for the transient process being studied, i.e the migration of Cs^+ over the lengthscale of interest (order centimeters) was orders of magnitude slower than the minutes required for each radiograph mosaic.

The initial OCV equilibration provided a reference from which we could evaluate Cs^+ migration, since the initial zero current pull should theoretically not cause changes in X-ray attenuation. We used the first radiograph of the OCV sequence as the reference mosaic, which was subtracted from each subsequent mosaic, yielding spatially averaged intensity differences between mosaics in time as shown in Figure 3.6. The nano-CT exports data in percent transmittance, %T, expressed from the Beer-Lambert law as [86, 87, 88, 89]:

$$\%T = 100\left(\frac{Q}{Q_0}\right) \tag{3.1}$$

where Q is the measured X-ray incidence and Q_0 is the reference X-ray incidence taken from imaging of pure air without the migration cell sample in place. We can then express changes in transmittance as:

$$\Delta\%T\,(t) = \%T_{t>0} - \%T_0 \tag{3.2}$$

where $\%T_0$ is the reference transmittance from the first mosaic of the operando set under OCV conditions. Subtracting this initial transmittance from each subsequent mosaic during the 2.5 μm current pulls to and from the X-ray field of view (FOV) allowed us to compute an average $\Delta\%T$ in time, quantifying the migration of Cs^+ into and out of the FOV. To corroborate our experimental findings, we also developed a numerical model with a representative 2D geometry.

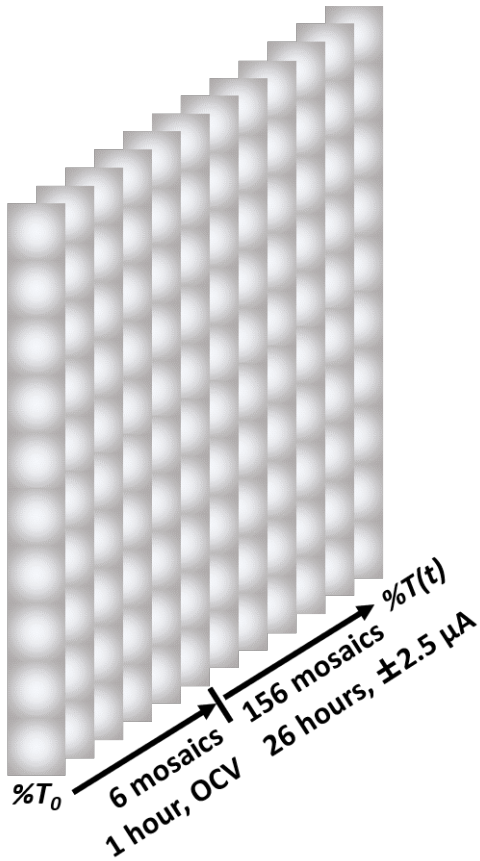

Figure 3.6: Mosaic X-ray stack in time for operando cation migration experiment. The transmittance from the first mosaic, $\%T_0$, subtracted from subsequent mosaics yields $\Delta\%T\,(t)$ as in Equation 3.2.

3.3 Modeling

3.3.1 Cation Transport Model

To compare with our experimental setup, we designed a representative 2D model as shown in Figure 3.7. We modeled the overlap of our experimental system with equilibrium water fluxes at the extremities to account for the full length of the electrodes and ionomer strip. An equilibrium proton source was placed at the ionomer strip extremity to account for proton generation/removal from the reference electrode. The model included two intersecting domains: a continuous ionomer domain to represent the Nafion strip and a porous CL. The Poisson-Nernst-Planck equation was applied over both domains using COMSOL (Stockhom, Sweden). The basic Nernst-Planck equation for specie diffusion and electromigration is below, along with the coupled Poisson equation, which reduces to Laplace's equation under electroneutral space charge density conditions:

$$J_i = -D_i \nabla c_i - c_i \nu_i \nabla \Phi \tag{3.3}$$

$$\kappa_r \kappa_0 \nabla^2 \Phi = 0 \tag{3.4}$$

where J_i is the flux of each specie, D_i is the diffusivity of each specie, c_i is the concentration of each specie, ν_i is the mobility of each specie, and Φ is the electric potential. κ_r and κ_0 are the relative permittivity of the medium (Nafion in this case, value of 20 [90]) and the permittivity of free space, respectively.

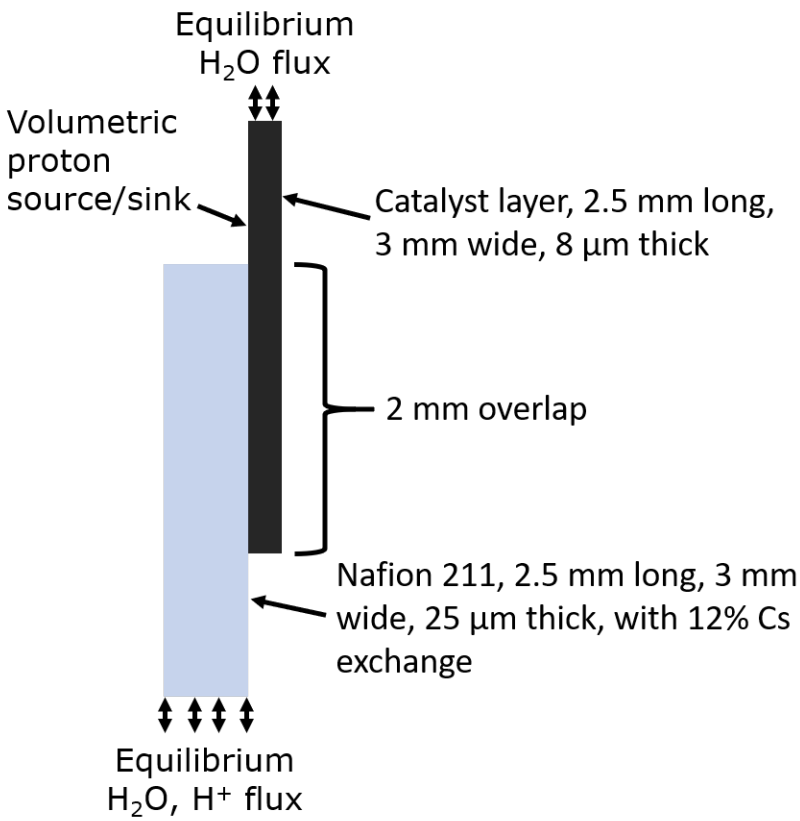

Figure 3.7: Geometry of 2D migration cell model. Represents the CL/Nafion strip overlap of the experimental setup.

The diffusivity and mobility of the protons were related through the Einstein relation as described below. The diffusivity and mobility of Cs^+ were user controlled and were not defined to be relatable through the Einstein mobility relation.

$$D_{H^+} = \frac{\nu_{H^+} RT}{z_{H^+} F} \tag{3.5}$$

where z_{H^+} is the charge number on the proton, R is the universal gas constant, T is the temperature of the system, and F is Faraday's constant. To enforce electroneutrality of

both domains while preventing the migration of the negatively charged sulfonate groups, we created a zero space charge density relation as defined below:

$$\rho = F\left(c_{Cs^+} + c_{H^+} - c_{SO_3^-}\right) = 0 \tag{3.6}$$

where the concentration of sulfonate groups, $c_{SO_3^-}$, was held constant at 1800 mol/m^3 [91] and the initial concentration of Cs^+ in the model is defined as the Cs^+ occupation fraction, r_{Cs^+}, of the sulfonate (SO_3^-) groups from the ICP-OES analysis (12%).

$$c_{Cs^+,0} = r_{Cs^+} * c_{SO_3^-} \tag{3.7}$$

Since we are modeling cation transport within the ionomer that is bulk-like in the Nafion 211 strip but hindered by the ionomer domain's tortuosity within the CL, we used a Bruggeman relation for the tortuosity as a function of the overall porosity. Note that the 'porosity' described here is the volume fraction of ionomer with respect to the overall volume of the CL.

$$\tau = \epsilon_p^{-\frac{1}{2}} \tag{3.8}$$

where τ and ϵ_p are the tortuosity and porosity of the ionomer medium. The specie diffusivity, D_i, within this domain can also be corrected using the following relation:

$$D_{i,eff} = \frac{\epsilon_p}{\tau} D_i = \epsilon_p^{1.5} D_i \tag{3.9}$$

During MEA polarization, dipole oriented water can be transported by protons and other cations during migration to the reducing electrode in a process called electroosmotic drag. For thick or long membranes, as we have in our experimental setup, electroosmotic drag contributes significantly to water accumulation at the reducing electrode. In our early iterations of this experiment, we found electroomostic drag to have a significant impact on water accumulation and X-ray attenuation. Thus, we integrated an electroosmotic drag effect into our model using the scaling of the proton flux as below:

$$j_{H_2O} = n_{drag}\left(\frac{I}{F}\right) = n_{drag} j_{H^+} \tag{3.10}$$

where n_{drag} is the number of water molecules dragged per proton (2.5 under saturated water conditions [92]) and I is the current driven from proton migration. Thus, we can set up a mobility ratio between water and protons, ultimately allowing us to assign a polarization-driven mobility to the water in our system:

$$\nu_{H_2O} = n_{drag}\nu_{H^+}\left(\frac{c_{H^+}}{c_{H_2O}}\right) \tag{3.11}$$

This relationship allowed us to account for the water in our system migrating to and from the X-ray FOV. It is important to note that we accounted only for the drag of water due to proton transport and not Cs^+ transport, which to the best of our knowledge, has not been studied in the literature. However, since the overall sulfonate group occupation by Cs^+ is low (12%), along with the order of magnitude mobility difference between protons and Cs^+, we can expect the effect of this phenomenon to be small.

To model the H_2 evolution and oxidation reactions, i.e. HER and HOR, we implemented a reaction source/sink in the CL. Since the HER and HOR reactions happen at equilibrium on Pt at STP in acidic media, the activation energy is low and we can model the rate of proton generation/removal as a function of the current draw (I) and the volume of the CL V_{CL}:

$$R_{H^+} = -\frac{I}{V_{CL}F} \tag{3.12}$$

where I is the specified current (± 2.5 μA in this case). This equation was applied in the CL domain where Pt is accessible for the HOR/HER reactions. At the ionomer extremity, where no Pt is available but protons are accessible in bulk, we used an equilibrium condition to add/remove protons from the system.

$$j_{H^+} = -k_{H^+}\Delta V \tag{3.13}$$

where k_{H^+} is an equilibrium constant and ΔV is the voltage at the equilibrium boundary condition (BC). It is important to note that with the low currents used in our analysis, the magnitude of the equilibrium constant k_{H^+} does not have a significant impact on the results of the analysis.

With our simplified geometry (i.e. shorter than the overall length of the CL and ionomer strip), we modeled the equilibrium of water at the CL extremity with the following relation:

$$j_{H_2O} = -\frac{D_{H_2O}}{\Delta x_{CL}}\left(c_{H_2O,local} - c_{H_2O,sat}\right) \tag{3.14}$$

where Δx_{CL} is the distance between the CL equilibrium BC to the gas delivery channel held at 100% RH, $c_{H_2O,local}$ is the water concentration at the equilibrium BC, and $c_{H_2O,sat}$ is the saturated concentration at the gas delivery channel. The same BC was applied at the extremity of the ionomer domain using the distance from the ionomer equilibrium BC to the reference electrode gas flow channel, Δx_{naf}:

$$j_{H_2O} = -\frac{D_{H_2O}}{\Delta x_{naf}}\left(c_{H_2O,local} - c_{H_2O,sat}\right) \tag{3.15}$$

3.3.2 X-ray Attenuation Model

From the transport model in COMSOL, we get the concentrations of Cs^+ cations and water as a function of position and time. To compare the modeled concentrations with the experimental transmittance, $\%T$, we can use published values of absorptivity coefficients of water and Cs^+ at 8 keV (the X-ray energy of the nano-CT system) [93] to calculate the molar absorptivities, a_i, which we can use with the Beer-Lambert Law [86, 87, 88, 89] to calculate the total Absorbance, A, of the CL:

$$A = l \sum_{i=1}^{N} a_i c_i \tag{3.16}$$

where l is the thickness of the medium (thickness of the CL), a_i is the molar absorptivity of each specie, and c_i is the concentration of each specie. Note that we are accounting for both Cs^+ and water in this analysis.

From the total absorbance, A, we can calculate the transmittance, %T as:

$$\%T = 100 * 10^{-A} \tag{3.17}$$

Tracking the transmittance in time, we can subtract the reference transmittance, $\%T_0$, yielding $\Delta\%T\,(t)$ as in Equation 3.2 and allowing us to compare our experimental results with our model.

3.3.3 Model Constants

The COMSOL and attenuation modelling parameters are listed below in Table 3.1, along with their origin or reference, as needed.

Table 3.1: COMSOL and attenuation model parameters.

Variable	**Model Parameter**	**Value [units]**	**Reference/Origin**
a_{Cs}	Cs absorption coefficient, 8 keV	310 [cm^2/g]	Hubbell et al., 1995 [93]
a_{H_2O}	H_2O absorption coefficient, 8 keV	10 [cm^2/g]	Hubbell et al., 1995 [93]
$c_{SO_3^-}$	Sulfonate group concentration	1800 [mol/m^3]	Peron et al., 2010 [91]
D_{Cs^+}	Cs^+ diffusivity in Nafion	2.5E-11 [m^2/s]	Tuned in model
D_{H^+}	Proton diffusivity in Nafion	8.5E-10 [m^2/s]	Peron et al., 2010 [91]
D_{H_2O}	Water diffusivity in Nafion	2.0E-10 [m^2/s]	Yeo et al., 1977 [94]
Δx_{CL}	Distance from CL equil. BC to flow channel	5 [mm]	Measured via micrometer
Δx_{naf}	Distance from Nafion equil. BC to flow channel	10 [mm]	Measured via micrometer
ϵ_P	Ionomer volume fraction in CL	0.11 [-]	Makharia et al., 2005 [95]
κ_r	Permittivity of Nafion	20 [-]	Paddison et al., 1998 [90]
k_{H^+}	Proton equilibrium constant	-10,000 [$\frac{\mathrm{mol}}{\mathrm{m^2-s-V}}$]	Tuned in model
l	CL thickness	8 [μm]	Measured via micrometer
λ	Water to sulfonate group ratio	22 [-]	Zawodzinski et al., 1993 [92]
n_{drag}	Electroosmotic drag factor	2.5 [-]	Zawodzinski et al., 1993 [92]
ν_{Cs^+}	Cs^+ mobility in Nafion	2.13E-14 [$\frac{\mathrm{s-mol}}{\mathrm{kg}}$]	Tuned in model
r_{Cs^+}	Cs^+ occupancy fraction	0.12 [-]	ICP-OES analysis

3.4 Results

3.4.1 Experimental Results and Discussion

After temperature and H_2 flow equilibration in the nano-CT chamber, X-ray mosaic collection began from bottom to top (membrane overlap to pure CL), with 10 radiographs collected for each mosaic, requiring a duration of 10 minutes per mosaic. For the first hour of imaging, no current was applied, allowing the establishment of a consistent reference transmittance from the X-ray radiograph mosaic analysis. After the first hour, a 2.5 µA current was applied to the CL/membrane overlap, driving protons, Cs^+, and water into the X-ray FOV. After 10 hours of the current applied to the CL/membrane overlap, the current direction was flipped, driving protons, Cs^+, and water to the reference electrode and out of the X-ray FOV. After 10 hours under the flipped 2.5 µA current, the current was once again reversed for 6 hours. The current and voltage profiles for this experimental sequence are shown in Figure 3.8. During each current pull, 6 radiograph mosaics were collected per hour, yielding a total stack of 162 mosaics from which total transmittance was calculated, as show in Figure 3.6. The first radiograph (air reference corrected - %T data) produced during the imaging sequence is shown in Figure 3.9.

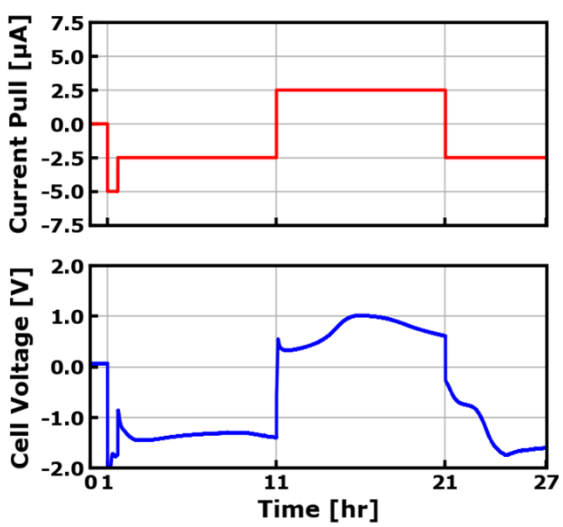

Figure 3.8: Experimental current and voltage profiles of 12% Cs^+-doped elongated MEA.

Since regions of higher attenuation appear darker in X-ray radiographs, we can clearly distinguish the pure CL from the membrane/CL overlap in Figure 3.9, since the membrane is significantly thicker than the CL (3x thicker) and has significantly more sulfonate groups occupied by Cs^+ than in the CL. The darkest region of Figure 3.9 is near the bottom and corresponds to the edge of the silicone gasket that intruded into the X-ray FOV and thus was eliminated in subsequent data processing.

Once the electrochemical testing and imaging were complete, we imported the X-ray data into ImageJ [96] for 2D visualization of each mosaic in time. While cycling through the

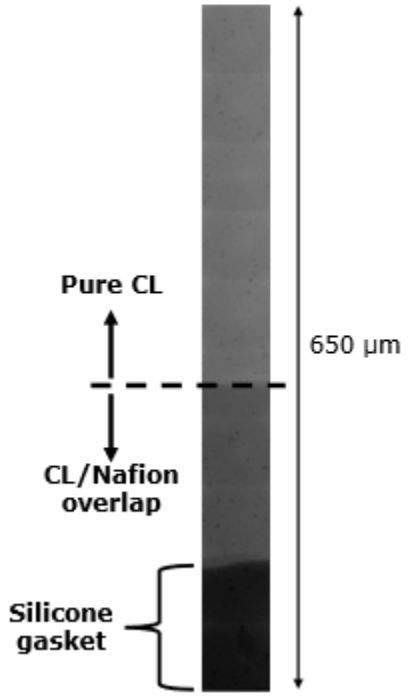

Figure 3.9: Referenced-corrected X-ray mosaic from operando nano-CT imaging.

mosaic stack, we discovered that the X-ray ROI shifted during imaging. To correct for the shift, we tracked distinguishable features of the image set in time and determined that the shift acted linearly between vertical position and time. Thus, we applied a numerical shift to counteract the effect of the experimental shift, effectively registering the stack of mosaics.

From the registered stack, we cropped off all but the pure CL ROI, leaving us with an unadulterated CL X-ray signal. We then applied the change in transmittance equation (Equation 3.2), giving us the change in transmittance over the duration of the experiment. The pure CL transmittance color map and corresponding averaged change in transmittance data versus experiment time are shown in Figure 3.10. From the color map of Figure 3.10a, we observed changes in attenuation during the back-and-forth H_2 pumping experiment due to water and Cs^+ migration into and out of the X-ray FOV. We captured the discrete transient nature of the transmittance change, $\Delta\%T$, with the plot shown in Figure 3.10b, which includes the corresponding H_2 pumping currents and voltages for comparison with the transmittance trend. Comparing the color map data with the bottom plot of Figure 3.10b, we see good agreement of the overall trend of change in transmittance and corresponding Cs^+ concentration from 3.10a. It is important to note that the brief uptick in change in transmittance in Figure 10b at 1 hour is likely due to H_2 bubble generation from HER near the FOV from a higher initial 5 µA pull. During the experimental set, this larger current was quickly changed to 2.5 µA to reduce the voltage of the cell, which had exceeded 2 V. With this change, we then saw a reduction in transmittance, i.e. an increase in attenuation due to Cs^+ and water accumulation within the CL ROI. Thus, after 10 hours of the reduced current and less H_2 generation, we observed a consistent decreasing trend in the transmittance change.

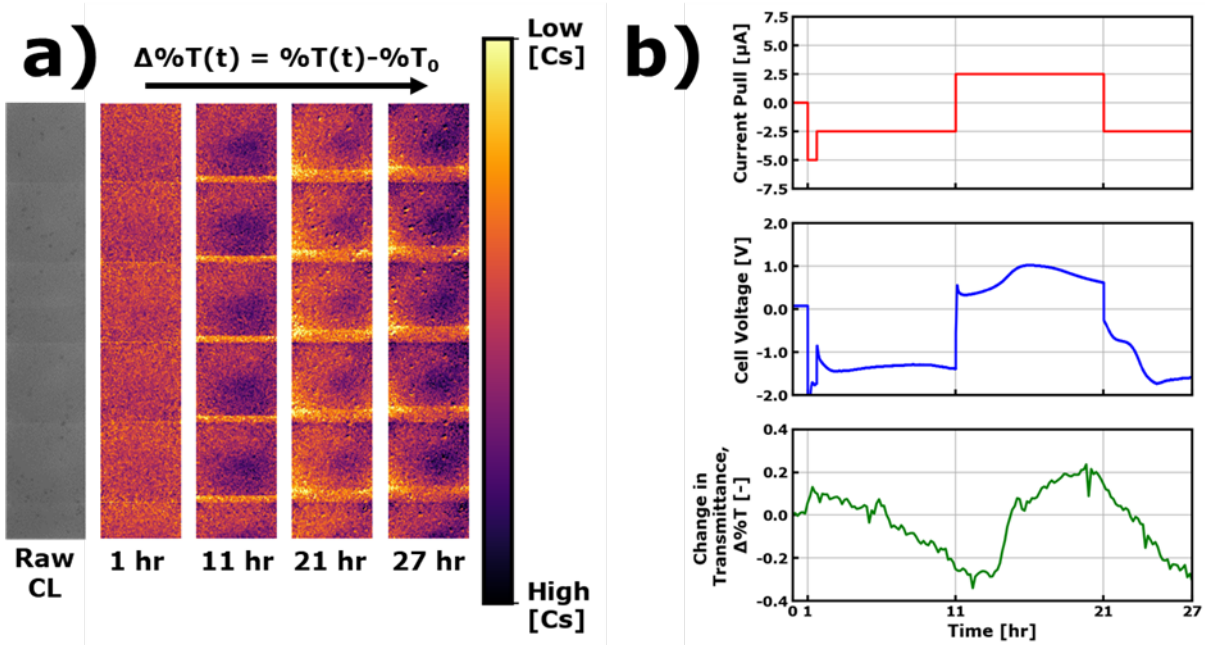

Figure 3.10: a) Color-mapped change in transmittance, $\Delta\%T$, at discrete times in the b) electrochemical cycling with the change in transmittance as a function of time, $\Delta\%T(t)$.

After the 2.5 µA was flipped to pull Cs^+ cations and water away from the FOV, we observed an inversion in the transmittance change profile, nearly reaching a stable $\Delta\%T$ at 21 hours. This change was due to Cs^+ and water migrating out of the FOV, reducing the attenuation of the ROI and thus increasing the transmittance (+ change in $\Delta\%T$). At 21 hours, the current was again flipped, causing migration back to the CL FOV, an increase in X-ray attenuation, and a decrease in transmittance (- change in $\Delta\%T$). With this alternating direction of current set, we successfully demonstrated back and forth Cs^+ and water migration, capturing the transience of the migration process.

3.4.2 Modeling Results and Discussion

To corroborate our experimental findings, we equilibrated our model with a 12% Cs^+ occupation for 12 hours of simulation time without a modeled current, after which all quantities (Cs^+, water, protons) had reached stable concentrations throughout the CL and ionomer domains. We then applied the volumetrically generated currents from the experimental set, i.e. ±2.5 µA, into and out of the CL for the duration of the experiment (10, 10, and 6 hours). The Cs^+ migration profiles from the forward, reverse, forward H_2 pumping simulations are shown in Figure 3.11, along with the inset directions of proton, Cs^+, and water transport corresponding to the negative potential gradient within the modeled system.

From Figure 3.11, we can see the change in Cs^+ concentration through the CL as a function of time, starting from an initial constant concentration and transitioning to a near-steady

state gradient achieved after 10 hours of simulated current. With the initial 2.5 µA pull into the CL/FOV, the Cs^+ concentration increases in time towards the leftmost extremity of the system, with a significant jump in concentration in the pure CL (x<0.5 mm). This sharp increase is the result of the increase in potential within the CL compared to the bulk ionomer from the reduced mobility of the protons in the ionomer films of the CL. With the increased potential gradient, the Cs^+ cations are pulled further into the CL, increasing the concentration gradient compared to the bulk ionomer.

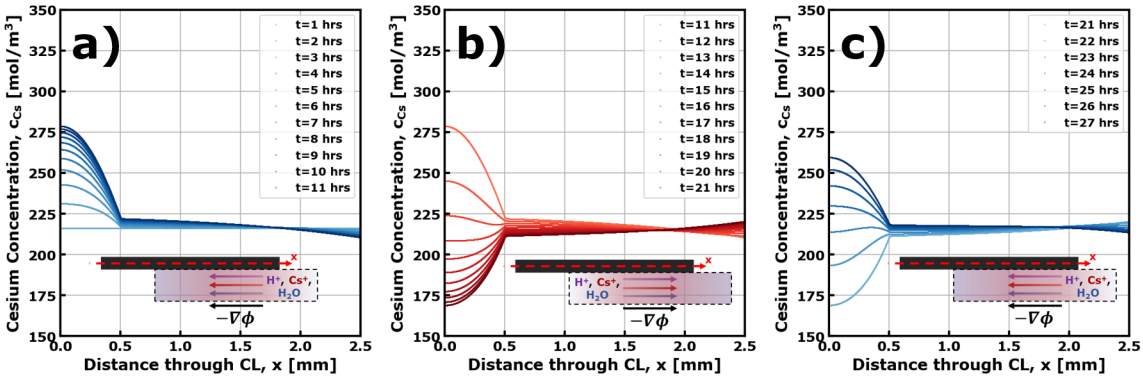

Figure 3.11: Cs^+ concentration as a function of position through the CL for a) the 2.5 μA pull into the CL/FOV, b) the 2.5 μA pull from the CL/FOV, and c) the 2.5 μA pull into the CL/FOV. Inset figures show the modeled CL/ionomer system, the slice position through the CL (x), and the migration direction of the mobile species due to the potential gradient.

After the first 2.5 µA pull into the CL, we numerically flipped the sign on the volumetric current density, reversing the direction of the migration process. Figure 3.11 b shows the corresponding inversion of the Cs^+ gradient through the length of the CL, again nearly reaching a steady-state accumulation at the leftmost extremity of the CL. The modeled current's sign was once again flipped, driving the mobile species back into the CL with the negative gradient in potential. With the last 6 hour current applied, steady-state accumulation was never truly reached, as is consistent with the experimental analysis' last step, where the X-ray attenuation changed with the flipped current at 21 hours but didn't reach a steady-state of accumulation.

From the concentration profiles in Figure 3.11, we applied the absorbance and transmittance formulas using published NIST values for the absorptivity of Cs^+ and water at our X-ray beam energy (8 keV) [93]. From these values and Equations 3.16 and 3.2, the transmittance was calculated as a function of time from the simulated concentration profiles. Subtracting the initial transmittance, $\%T_0$, we obtained the change in transmittance as a function of time, $\Delta\%T(t)$, for the water, Cs^+, and the combination of both, allowing us to compare our numerical analysis with our experimental results, as is shown in Figure 3.12. For the modeled results, we used the $\Delta\%T$ value at x=0.325 mm into the CL from the left extremity, representing the effective center of the X-ray mosaic of the experimental setup.

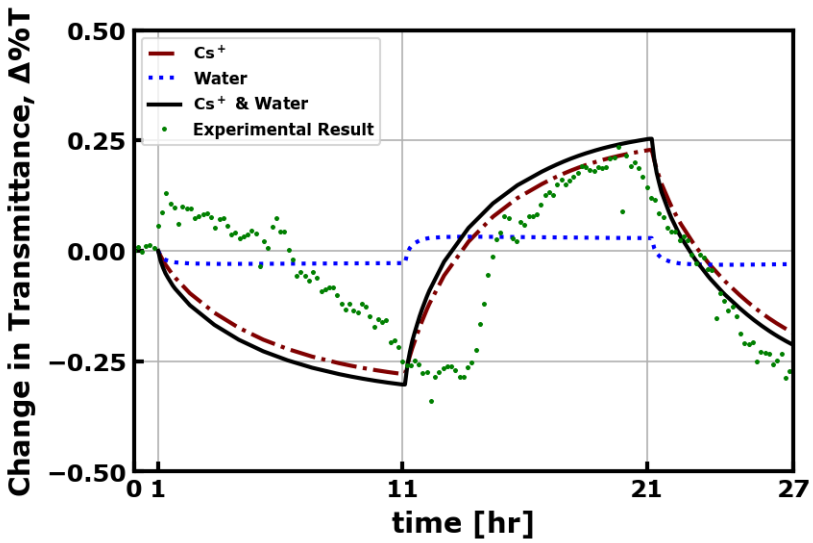

Figure 3.12: Comparison between experimental and modeled results.

From Figure 3.12 we can see that while the water's migration did impact the change in transmittance, the total change in transmittance is dominated by the Cs^+ contribution. This is due to the much larger attenuation coefficient of Cs^+ (310 cm^2/g) compared with water (10 cm^2/g) and confirms that the attenuation signal we measure with the nano-CT is primarily due to Cs^+ migration. It is also interesting to note that the water's change in transmittance reached its equilibrium state much earlier in the simulation, compared with Cs^+. This is due to the larger diffusivity and mobility of water compared with Cs^+ in Nafion (see Table 3.1) and shows that the dynamic behavior measured with X-ray attenuation at later times in the experimental set is again mostly due to Cs^+ migration.

Overall, the modelled total change in transmittance shows relatively good agreement with the experimental data, especially for the more stable 11-21 hour and 21-27 hour intervals. The experimental 1-11 hour interval corresponds poorly to the modeled result, due to the sharp increase at 1 hour when the 5 µA current was applied. The change in transmittance from 1 hour to 12 hours decreased linearly, which is inconsistent with overall migration trends, which are exponential in nature. Again, this discrepancy is likely the result of a high HER rate due to the initial 5 µA application and corresponding H_2 generation shifting the X-ray field of view. As a result of this experimental discrepancy with the expected dynamics of similar systems, we focused on the 11-21 and 21-27 hour durations for tuning the modelled Cs^+ diffusivity and mobility parameters to match the experimental results.

The values for Cs^+ diffusivity and mobility resulting from tuning of the model were 2.5E-11 m^2/s and 2.13E-14 s-mol/kg, respectively. These values are within an order of magnitude for the published experimental values for Cs^+ diffusion in Nafion (5.2E-12 m^2/s) [97] and the corresponding mobility from the Einstein mobility equation (Equation 3.5, 2.13E-15 s-mol/kg). These values are considered within the range of expected values for experimental measurements of diffusivity and mobility in a highly variable material like Nafion or

similar ionomer, which vary substantially with water uptake. Within the literature, even well-studied species like protons, O_2, H_2, water, etc. show significant variation in diffusivities from different experimental techniques and even duplicates of the same technique. To frame the upper bound on Cs^+ diffusivity, we can use the diffusivity of Cs^+ in liquid water, 2E-9 m^2/s [98]. Compared to our value of 2.5E-11 m^2/s and the lower bound from Yeager et al. [97] that was defined at a lower water content than we used in our experiment, we can see that our estimate is within the bounds of expected values, giving credence to our modeling of the physical phenomena occurring within our miniature H_2 pumping PEMFC.

In terms of quantifying the accumulation of Cs^+ within the CL, we can plot the Cs^+ concentration, normalized by the total sulfonate group density to get the Cs^+ occupation percentage. The modeled results of this for the forward and reverse H_2 pumping simulations are shown below.

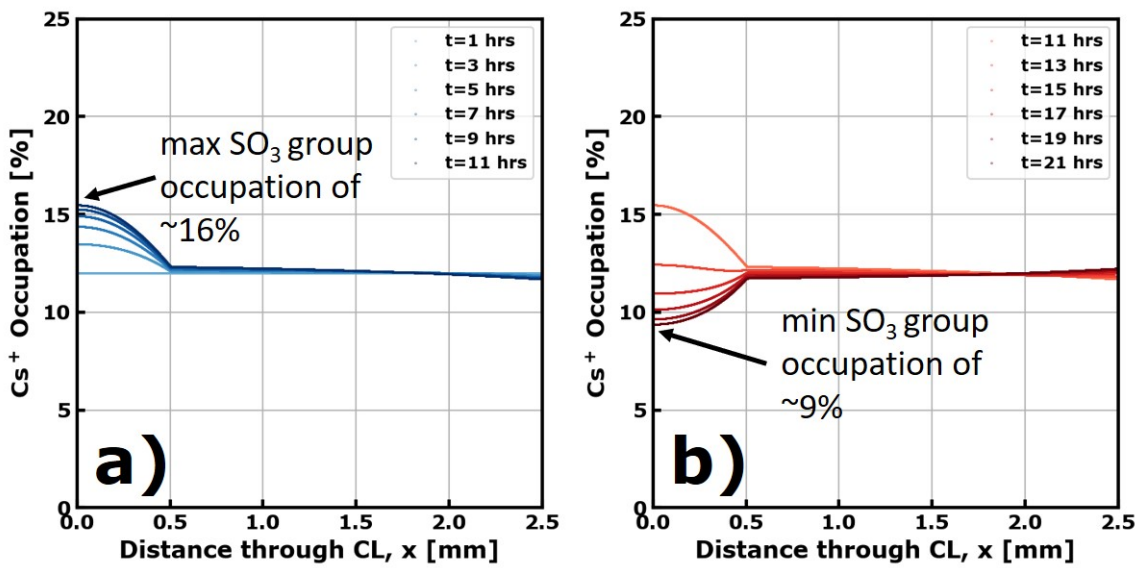

Figure 3.13: 10 hour a) forward and b) reverse H_2 pumping simulated results for local Cs^+ occupation. Note that this is the same data presented in Figure 3.11, but normalized by the sulfonate group concentraton, $c_{SO_3^-}$ to show sulfonate group occupation by the Cs^+.

Figure 3.13 shows that over the course of the 10 hour H_2 pumping current into the CL/X-ray FOV, the sulfonate group occupation increases to around 16% in the CL from the initial nominal doping of 12%. This low total sulfonate group occupation by Cs^+ is expected, due to the low current density being passed through the MEA. Typical MEAs operating with air and H_2 can operate at 1 A/cm^2; with our setup, we are operating at around 10 mA/cm^2. Due to the low current density, we don't expect high exchanges within the catalyst layer or any of the performance degradation associated with high exchanges. This is consistent with our experimental data, where we saw no real evidence of protonic choking, which would have been obvious if higher exchange percentages had occurred.

3.5 Conclusion

In this combined experimental and modeling study, we examined the dynamics of Cs^+-cation migration and accumulation within the CL of an operating PEMFC using an operando X-ray analysis cell. We performed H_2 pumping experiments with a custom fabricated and Cs^+-doped MEA to measure X-ray transmittance as a function of time. This X-ray transmittance was enabled through our nano-CT facility in ABS mode, which took radiograph mosaics during H_2 pumping currents to and from the X-ray FOV, allowing for computation of the transmittance and change in transmittance over time. To verify our experimental findings, we developed a cation transport model in COMSOL, where we simulated our H_2 pumping experiments using a simplified geometry. From the combined model and experimental results, we estimated an experimental diffusivity and mobility of the Cs^+ cations and found them to be consistent with the range of values reported in the literature for similar conditions. Finally, we used our model to estimate a maximum sulfonate group occupation in the CL under the currents applied to the system. For the low current densities studied in this analysis, i.e. 10 mA/cm^2, our model predicted very low local exchanges (less than 16% for a nominal initial exchange of 12%), causing little to no performance degradation.

Overall, this analysis highlights the capability of the nano-CT facility to measure PEMFC processes in electrodes in-operando, which to date has been exceptionally difficult due to traditional PEMFC geometries and materials. This novel platform has potential to be used for further transport and degradation studies, allowing operando observation of processes of high interest to the porous electrode communities. With further development of methodology and supporting modeling, this platform can be a powerful tool to leverage in the development and analysis of electrochemical sytems.

Chapter 4

Measurement of Oxygen Transport Through Water-filled Nanopores

4.1 Motivation

HSC supports are a recently developed fuel cell technology that have enabled enhanced catalyst access and activity and improved catalytic retention, facilitating the reduction in overall Pt loadings while improving performance and durability [8, 9, 59]. These carbon supports are unique in that their primary carbon particles contain micro- and mesopores (pores in the range of 1-10 nm) [9, 99] that contain the Pt nanoparticle catalysts required for the ORR reaction. Traditional supports like Vu carbon or graphitic carbon have Pt buried in the interior of the carbon support, but due to a lack of primary particle porosity, don't allow O_2 to access the internal Pt particles, making them electrochemically inaccessible and financially squandered. Figure 0.2b in Chapter 0 of this dissertation showed the cryo-STEM CT comparison of the new state-of-the-art HSC compared with the traditional state-of-the-art Vulcan (Vu) support, highlighting the percentage of the Pt that is internal for the HSC versus external for the Vulcan [9].

This internal porosity is important, as it allows the Pt catalyst to be accessible to the ORR reaction via O_2 and proton diffusion via the water channels formed by the micro- and mesopores, as shown in Figure 4.1 but prevents sulfonate group poisoning by the ionomer binder in the CCL. With the small size of the micro- and mesopores, the ionomer chains are unable to infiltrate these small pores, preventing direct ionomer coverage of the Pt and reducing sulfonate group poisoning for improving catalytic activity, as has been documented in the literature [100, 101, 102, 103].

At high current densities, the O_2 permeability of the transport medium limits the rate of the ORR reaction and ultimately the output current. In recent years, much effort has focused on the O_2 permeability properties of ionomer films and ionomer film/catalyst surface interfaces, as can be expected with the use of Vu or other LSAC supports with significant Pt/ionomer interactions. However, with HSC supports, the Pt particles are no longer in contact with the ionomer film, eliminating any interfacial resistances yet not eliminating permeation through the ionomer films covering the pores. The diffusion through these water-filled pores, as illus-

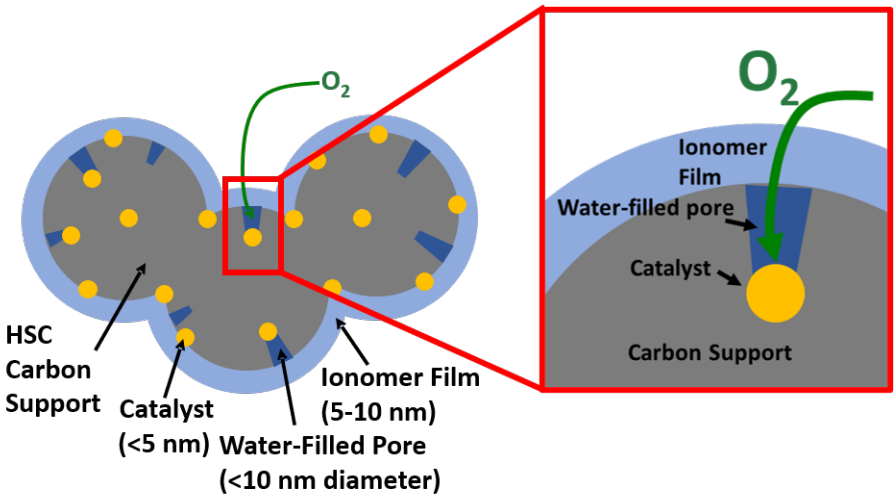

Figure 4.1: Schematic of O_2 transport through water-filled micropore of HSC carbon support from Figure 0.2b.

trated in Figure 4.1, is of interest to the fuel cell community, as the confined water presents an additional transport barrier to O_2 delivery.

These pores fill with water at the operating relative humidities of PEMFCs (60-100% RH) and add an additional permeation resistance to the delivery of O_2 to the catalyst surface. This permeation resistance has been documented by Ramaswamy and colleagues [99], where they studied the non-Fickian O_2 transport resistance (R_{NF}) of different HSC supports with varying fractions of micropore volume (defined by their study as pores < 2 nm diameter). The R_{NF} is synonymous with non-pressure dependent resistances as defined by Baker et al. [74] and results from O_2 transport resistances arising from transport through ionomer films, water, or Knudsen diffusion, all of which are unaffected by changing the partial pressure of O_2 in the gas phase; thus they are labeled non-pressure dependent or non-Fickian resistances.

The work by Ramaswamy and colleagues has shown that with increasing volume fraction of micropores, a greater R_{NF} is witnessed [99]. This result is inconsistent with the current knowledge of O_2 transport through bulk water, as the resistance would then be independent of pore size given constant areal flux through the water domains. Thus, this hindrance result indicates deviation from bulk water permeation, similar to how diffusion through confined gases is less than that of the bulk, as described by Knudsen diffusivity. Due to the difficulty in measuring transport through nano-domains, the literature is scarce for experimentally measured liquid-confined gas transport. Some molecular dynamics (MD) analyses have predicted increased gas solubilities and hindered diffusivities for confined liquid shale-gas systems [104, 105, 106], but no literature exists on water-confined O_2 transport that is of interest for fuel cell CLs. In this work, we sought to measure the O_2 permeability of confined water using our O_2 transport apparatus described in our previous work, as described in Chapter 2 [65, 73].

4.2 Mathematical Formulation

Prior to experimentally evaluating O_2 transport for confined water, it is useful to predict the dry and wet permeabilities for comparison against the experimental measurements. In the following sections, we provide the well-studied fundamentals of gas diffusion through small pores and bulk water that we used for comparison with our experimental results.

4.2.1 Dry Transport Theory

Knudsen diffusion is well-described in the literature and can be simply defined as diffusion where the effective diameter of the diffusion media's pores is on the same length order as the mean free path of the gas molecules, resulting in significant gas molecule/wall interactions that aren't present in transport through larger pores or bulk gases. The onset of Knudsen diffusion's applicability is a function of the pore diameter and the mean free path of the gas and is expressed through a ratio known as the Knudsen number [107], presented below:

$$Kn = \frac{\delta}{d} \tag{4.1}$$

where δ is the mean free path of the gas and d is the characteristic length scale or effective diameter of the pore. The mean free path is described as [107]:

$$\delta = \frac{\mu}{P}\sqrt{\frac{\pi k_B T}{2M}} \tag{4.2}$$

where μ is the viscosity of the gas, P is the pressure of the gas, k_B is the Boltzmann constant, T is the temperature of the gas, and M is the molecular mass of the gas specie.

Knudsen numbers higher than 10 represent full Knudsen regime diffusivity, i.e. the interactions between the gas molecules and the pore walls are much more important than molecule-molecule interactions. Knudsen numbers less than 0.01 correspond to the bulk regime, where molecule-molecule interactions dominate and wall-molecule interactions become negligible. Knudsen numbers between these two regimes correspond to a named transition regime, with a Knudsen number greater than 0.01 but less than 10. Within this transition regime, the diffusivity can be expressed through the Bosanquet equation. The equations for pure Knudsen diffusivity [107] and transition regime Bosanquet diffusivity [108, 109] are expressed below:

$$D_{Kn} = \frac{d}{3}\sqrt{\frac{8RT}{\pi M}} \tag{4.3}$$

$$D_B = \left(\frac{1}{D_{Kn}} + \frac{1}{D_M}\right)^{-1} \tag{4.4}$$

where M is the molecular mass of the gas being analyzed, R is the universal gas constant, T is the temperature in Kelvin, and d is the diameter of the pore. For the Bosanquet equation,

D_M is the molecular diffusivity or bulk diffusivity corrected for the temperature of interest using the following relation for dry, non-polar gases [110]:

$$D_M = D_{ref} \left(\frac{T}{T_{ref}} \right)^{1.82} \tag{4.5}$$

where D_{ref} is the experimental or table value of the diffusivity corresponding to the reference temperature, T_{ref}.

For 21% O_2 in N_2 at STP, the mean free path, δ, is approximately 70 nm, corresponding to Knudsen numbers of 7 and 3.5 for pore diameters of 10 and 20 nm and transition regime diffusion, near the edge of pure Knudsen diffusion. Thus, we can use Equation 4.4 to benchmark our dry diffusivity measurements.

4.2.2 Filled Pore, Wet Transport Theory

In the case of O_2 transport through confined water, we must consider two-phase transport, i.e. sorption of O_2 into the confined volume of water, subsequent diffusion through the liquid water, and desorption from the water back to the gas phase. To express this transport mathematically we must use permeability. Permeability is defined as the product of the diffusivity (D) and solubility (S), expressed below as ε since the variable P is traditionally used to denote pressure:

$$\varepsilon = SD \tag{4.6}$$

The solubility, S, reflects the O_2 sorption/desorption processes from water and is synonymous with a Henry's law constant. The diffusivity, D, reflects the diffusivity of the O_2 through the liquid water. Combined in this manner, they allow for the calculation of the theoretical value of O_2 permeability through bulk water.

Ito et al. [111] and others [35, 36] have studied the bulk solubility and diffusivity of O_2 in water and have modelled the solubility and diffusivity processes with the following empirical relations from [112] and [113], respectively:

$$S = \left(5.08 * 10^6 \exp\left(-500/T\right)\right)^{-1} \left[\frac{\text{mol}}{\text{cm}^3 - \text{atm}}\right] \tag{4.7}$$

$$D = 4.2 * 10^{-2} \exp\left(-E_D/RT\right) \left[\frac{\text{cm}^2}{\text{s}}\right] \tag{4.8}$$

where E_D is 13.368 kJ/mol [113]. Combining equations 4.7 and 4.8 as described in equation 4.6 yields an O_2 permeability of water at 50°C of 4.1E-14 mol/m-s-Pa.

4.2.3 Combining Dry and Wet Theory

To allow for comparison between our experiments and the theoretical trends of wet permeation and dry diffusion, we chose to express the wet transport as a dry-transport-normalized value. This normalization allowed us to eliminate the pore geometry of our transport medium from the calculation and express the transport process as a transport enhancement or hindrance factor, K. This factor K was expressed as:

$$K = \frac{\varepsilon_{wet}}{\varepsilon_{dry}} \tag{4.9}$$

where ε_{wet} is the filled-pore permeability of water and ε_{dry} is the pseudo dry permeability we can extract by dividing the dry diffusivity by the universal gas constant R and the temperature T, as is shown below:

$$\varepsilon_{dry} = \frac{D_{dry}}{RT} \tag{4.10}$$

For bulk water permeability and bulk air diffusivity, the K value can then be calculated to be 4.6E-6 (unitless). We can also account for the theoretical reduction in dry diffusivity, using the Bosanquet formulation from Equation 4.4. Since the wet permeability of confined water is of interest in this study, the following theoretical formulation leaves ε_{wet} unchanged:

$$K_{theo} = \frac{\varepsilon_{wet}}{\frac{\left(\frac{1}{D_{Kn}} + \frac{1}{D_M}\right)^{-1}}{RT}} \tag{4.11}$$

We can then compare our experimental K values with K_{theo}, indicating either enhanced wet transport ($K > K_{theo}$) or hindered wet transport ($K < K_{theo}$).

4.3 Experimental

To measure the permeability of nanoscale confined water, we used anodic aluminum oxide (AAO) membranes from InRedox (Longmont, CA). These AAO membranes provided uniform pore diameters in nominal 10 nm and 20 nm pore diameters as shown in Figure 4.2. We assembled them into testable samples by mounting them onto Kapton blanks with an 8 mm hole removed from the center using two-component epoxy as shown in Figure 4.3. The epoxy did wick into the 8 mm diameter cutout area, so the areas were adjusted with a correction factor derived from segmentation and pixel statistics with ImageJ [96]. Prior to each experiment, the Kapton/AAO samples were dried in a vacuum oven at 100°C for at least 12 hours before testing to drive off any absorbed or adsorbed water.

After drying, the samples were immediately installed in the O_2 transport cell (shown in Figure 4.4), as has been described in our previous work [73]. The system was brought up to 50°C with dry N_2 flowing to the sample to ensure a dry state with which to measure the dry

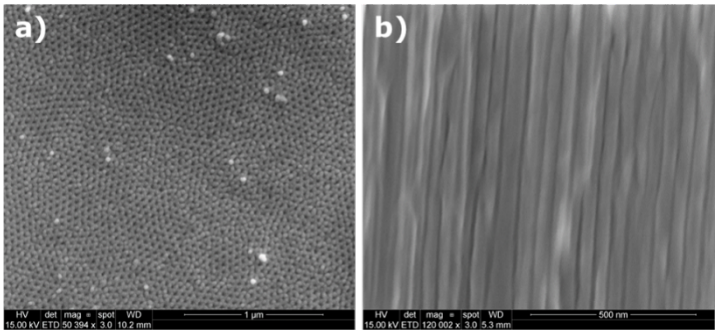

Figure 4.2: SEM images of a) top and b) cross-section of an AAO membrane with 20 nm pores. Note that the AAO membranes were coated with 2 nm of gold to prevent charging during imaging.

Figure 4.3: AAO sample assembly with Kapton blank and epoxy sealant.

diffusivity before proceeding to the filled-pore measurement with humidified gases. The flow to the anode was held at a low relative humidity, i.e. less than 50% in order to generate a concentration-driven water flux to the anode to prevent flooding from water generation from ORR on the cathode side of the MEA. Two different types of fuel cell test stand were used; a Biologic FCT-150S (Biologic Instruments, Sessinet-Pariset, France) test stand was used to supply dry gases to the test cell using the humidifier bypass capability and humidified gases were supplied via a Scribner 850e (Scribner and Associates, Southern Pines, NC) test stand, which also controlled the test cell's temperature and total pressure.

One improvement to our O_2 transport setup from our previous work [73] was the addition of an O_2 sensor below the sample. In our previous work, the O_2 concentration was assumed to be zero below the sample under the limiting current condition (a very good assumption when output currents are less than 1 mA), but due to the porous nature of the AAOs under dry conditions, it was necessary to register the O_2 concentration below the sample from which to extract the dry diffusivity. The O_2 sensor system we chose was a PreSens OXY-1 SMA system with a PSt3 dipping probe coupled with a Pt100 temperature probe, all from PreSens Precision Sensing Gmbh (Regensburg, Germany). With the temperature and concentrations of O_2 below the sample, we were able to set up relations for the extraction of the differences in O_2 partial pressure (ΔP_{O_2}) and concentration (Δc_{O_2}) for use in our permeability and diffusivity expressions.

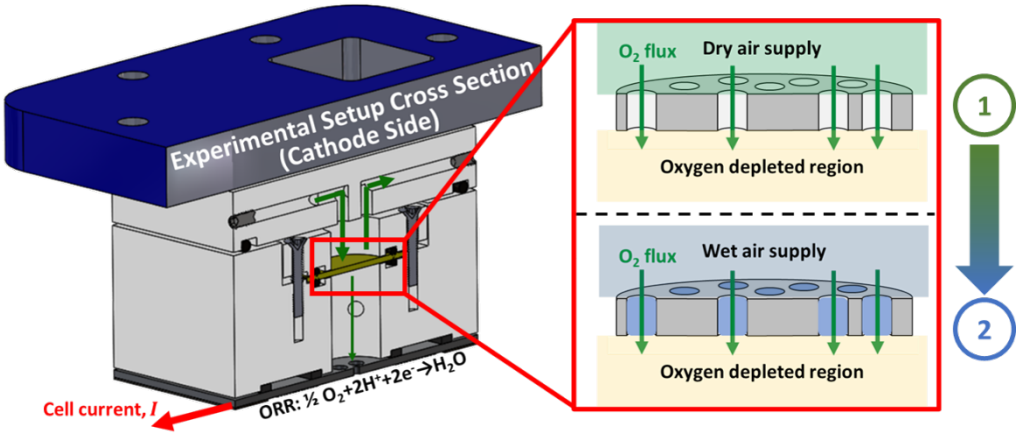

Figure 4.4: Cross-section of experimental cell with zoomed in view of dry and capillary condensation-filled AAO membrane sample.

4.3.1 Dry Diffusivity

To measure the dry diffusivities of the AAO samples, a background current was established under dry N_2 flow to the sample on the cathode side of the MEA and 1% H_2 to the anode at an RH of 35%. The 1% H_2 was used to minimize the H_2 crossover current, allowing for improved current resolution with the potentiotstat at the very low currents generated under filled-pore conditions. Once the current and concentration of O_2 below the sample had stabilized, the cathode gas supply was switched to air, driving a flux of O_2 through the sample due to a concentration difference from the ORR current reducing the O_2 to water at the MEA of our test cell. The N_2 and air currents and O_2 concentrations measured below the sample are shown in Figure 4.5. It is important to note the non-zero O_2 concentration measured by the O_2 sensor under air supply conditions. It was for this reason that we needed the sensor below the sample in order to accurately calculate the change in concentration across the sample needed for the diffusivity calculation.

From the steady-state ORR current generated in our cell, I, we can calculate the O_2 flux through the sample from Faraday's law of electrolysis:

$$J_{O_2} = \frac{I}{nF} \tag{4.12}$$

where n is the number of electrons transferred per mole of O_2 and F is Faraday's constant (96485 Coulombs/mole e-).

Then, we can calculate the concentration of O_2 above the AAO sample ($c_{O_2,top}$) using the ideal gas law:

$$c_{O_2,top} = \frac{P_{O_2,top}}{RT} \tag{4.13}$$

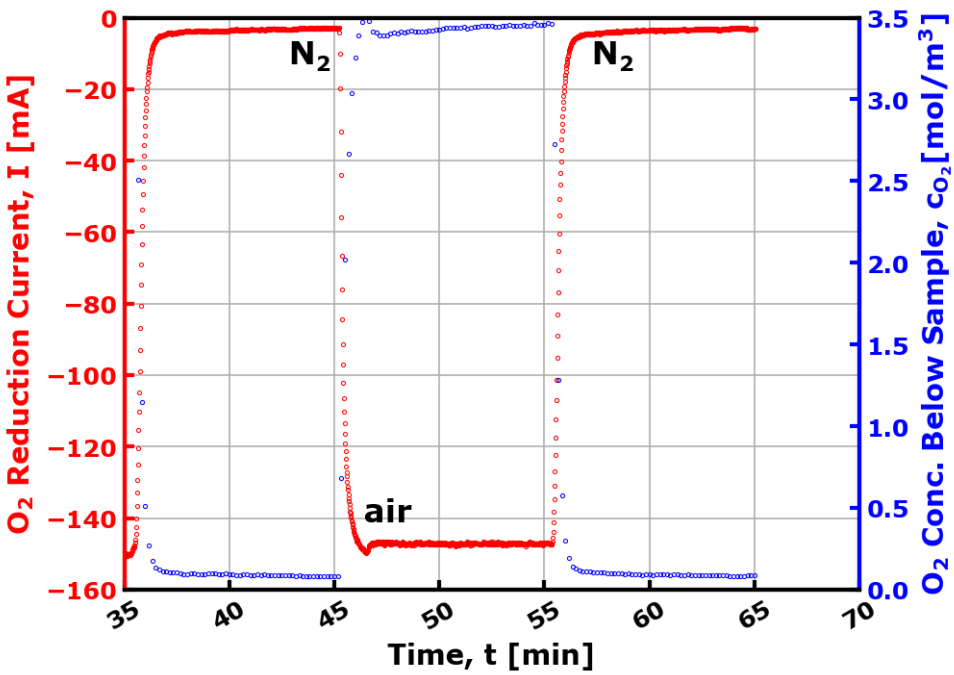

Figure 4.5: N_2/air switching currents and O_2 concentration measured below the sample. Experiment performed at 50°C, 1 atm total pressure, and 0% RH (sample).

where $P_{O_2,top}$ is the partial pressure of O_2 in the dry gas supply, and R and T are the universal gas constant and temperature, respectively.

The concentration of O_2 below the sample required extrapolation from the measured concentration of O_2 from the sensor as well as the knowledge that under limiting current conditions, the O_2 concentration at the cathode/membrane interface of the MEA is zero. These two position and concentration datapoints, as well as the known O_2 transport resistance of the full cathode catalyst layer allowed for the calculation of the concentration of O_2 directly below the sample, as shown by the O_2 concentration profile from the bottom of the AAO sample to the CCL in Figure 4.6.

With a constant O_2 flux through the system shown in Figure 4.6, and known resistance between the surface of the GDL and the CCL ($R_{cathode}$) as measured with limiting currents for R_{O2} extraction [74], we can calculate the concentration of O_2 at the GDL from the below relation, noting that $c_{O_2,CCL}$ is reduced to zero under limiting current conditions:

$$c_{O_2,GDL} = c_{O_2,CCL} + R_{cathode} J_{O_2} = R_{cathode} J_{O_2} \tag{4.14}$$

The calculated O_2 concentration at the GDL surface can be used, along with the measured O_2 concentration from the sensor $c_{O_2,meas}$, as:

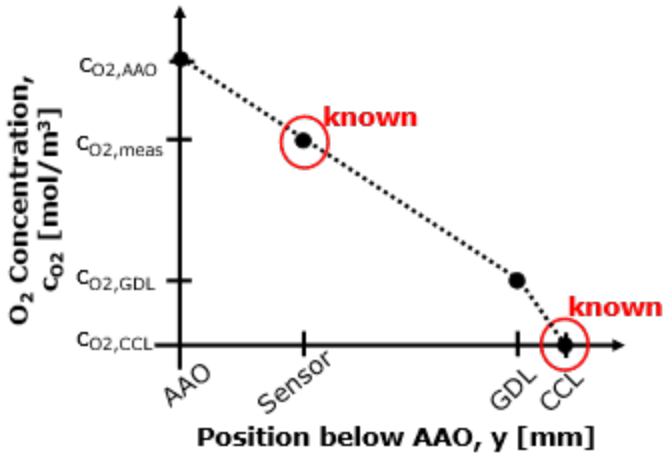

Figure 4.6: O_2 concentration profile below AAO sample. Note that the slopes of the lines between the AAO and GDL and GDL and CCL are different. This is due to the different effective diffusivities of the gas between the AAO and the GDL and from the GDL to the CCL, i.e. through the cathode of the test cell's MEA.

$$c_{O_2,AAO} = \left(\frac{c_{O_2,meas} - c_{O_2,GDL}}{y_{GDL} - y_{sensor}} \right) (y_{GDL} - y_{AAO}) + c_{O_2,GDL} \tag{4.15}$$

With the concentrations of O_2 known directly above and below the sample, as well as the flux through the sample from the current, the dry diffusivity can be calculated as:

$$D_{dry} = \frac{Il}{4AF\Delta c_{O_2}} \tag{4.16}$$

where l is the thickness of the AAO and A is the total pore area calculated from the total diameter of the sample, the pore density, and pore diameter, and Δc_{O_2} is the change in O_2 concentration across the AAO. This calculated dry diffusivity can be compared with the Bosanquet formulation of the diffusivity as described by equation 4.4.

4.3.2 Filled Pore, Wet Permeability

For the measurement of the water-filled pore case, we brought up the dewpoint of the cathode humidifier and corresponding sample gas stream incrementally from 30% RH. The incremental increase in the dewpoint and the relative humidity of the gas stream to the sample allowed us to observe the capillary condensation process dynamically by monitoring the current output of the test cell. Figure 4.7 shows this process for a 20 nm porous AAO membrane.

As shown in Figure 4.7, there is little change in current due to the relative humidity changes below 46% RH. These minimal changes in current are due to the lowering of the partial pressure of O_2 in the gas stream corresponding to the increase in water partial pressure. Once

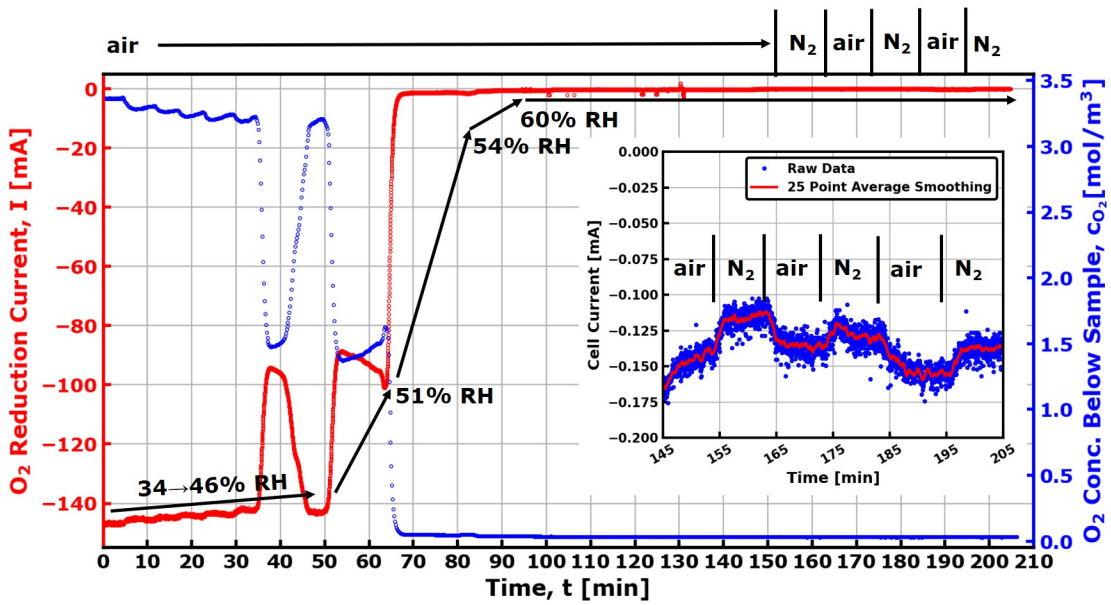

Figure 4.7: Current and O_2 concentration profiles for the 20 nm AAO capillary condensation process for whole experimental duration and (inset) filled-pore currents corresponding to N_2 and air switching. Note the difference in ORR current going from dry or un-condensed pores (up to 46% RH) compared to the filled case (60% RH). Experimental data was collected at 50°C, 1 atm total pressure, and sample RH ranging from 34 to 60%.

the RH reaches the critical value for capillary condensation (ca. 46-60% RH for the 20 nm case), the pores fill with water, severely restricting the rate of transport of O_2 to the MEA for the ORR reaction. This restriction corresponds to a massive reduction in output current (hundreds of mA to tens of μA). Once a stable air current had been established for the filled-pore case, the cathode gas supply was switched back and forth between air and N_2, establishing a difference between the background N_2 current and the current due to O_2 permeation. From the differences between the N_2 and air currents, we can calculate the permeability of the water-filled pores from the relation:

$$\varepsilon = \frac{Il}{4AF\Delta P_{O_2}} \tag{4.17}$$

where I is the test cell MEA's current output, l is the thickness of the AAO membrane, A is the area of the pores as before, and ΔP_{O_2} is the partial pressure difference across the AAO as calculated from the same methodology as the concentration profile shown in Figure 4.6 and calculated in Equation 4.15.

The wet and dry results from each experiment were then combined into the dimensionless wet to try transport ratio, K, via the following relationship in terms of experimental parameters, noting the elimination of the geometric constansts l and A:

$$K = \frac{\varepsilon_{wet}}{\varepsilon_{dry}} = \frac{\frac{Il}{4AF\Delta P_{O_2}}}{\frac{Il}{4AF\Delta c_{O_2}RT}} = \frac{\frac{I_{wet}}{\Delta P_{O_2,wet}}}{\frac{I_{wet}}{\Delta P_{O_2,dry}}} \tag{4.18}$$

4.4 Results

After baking the samples at 100°C in the vacuum oven for 12 hours, we transferred the assembled AAO wafers (Figure 4.3) to the test cell shown in Figure 4.4 and warmed up the test cell and sample under dry gas flow to the cathode (0% RH) and slightly humidified gas (35%) RH to the anode. Pure N_2 was supplied to both the anode and cathode. The dry gas equilibration of the AAO sample prevented any volumentric absorption of water and prevented monolayers of water from forming on the pore surfaces from adsorption. Once the sample temperature reached 50±0.3°C, we began the experiment.

First, we performed the dry experiment for the extraction of the dry diffusivity of the pores. Just as in the warmup, we supplied 0% RH N_2 to the AAO sample and 1%H_2 to the anode (30% RH) to establish a background current. Again note that the 1%H_2 was used to lower the H_2 crossover current of the fuel cell, enabling the improved resolution limit of our potentiostat at low current. Once the background current had stabilized, we switched the cathode gas supply to air, again flowing it through the humidifier bypass. The current change under these dry conditions was substantial (see Figure 4.5). We allowed the current to stabilize along with the measured O_2 concentration below the sample with the PreSens O_2 sensor. From the difference between the background and air currents, we calculated a current due to O_2 diffusion through the pores of the AAO, yielding an experimentally measured O_2 diffusivity. The dry diffusivities from these measurements are shown in Figure 4.8 along with the bulk value of O_2 diffusivity in air and the Bosanquet corrected diffusivity from Equation 4.4.

We can see from Figure 4.8 that our measured values of dry diffusivity sit below the projected Bosanquet prediction for both 10 and 20 nm pore sizes. For both pore sizes, the dry diffusivities are around a factor of two lower than the prediction. However, the combined vertical and horizontal error bars that originate from the uncertainty in the AAO sample's area, A, in Equation 4.16, from specified tolerances on the pore diameters and pore densities show that intersection of the data and the predicted values are possible for diffusivities estimated from the lower end of pore diameters and pore densities. This intersection of the predicted and measured values for smaller (but within specification) pores indicates that the pores of our AAO samples were less than their nominal values.

After the dry experiment, we engaged the Scribner fuel cell test stand's humidifier and flowed our cathode supply gases through it at an initially low relative humidity (30%). Again, we established a background current with N_2 supplied to the sample/cathode and once stabilized, switched to air. Just as with the pure dry case, we saw dramatic change in the output current of our test cell, showing that the pores were in fact open at this low RH. We again calculated the dry diffusivity (accounting for the reduction in O_2 concentration due to the gas RH) and found the diffusivity measurements to be comparable to the purely dry

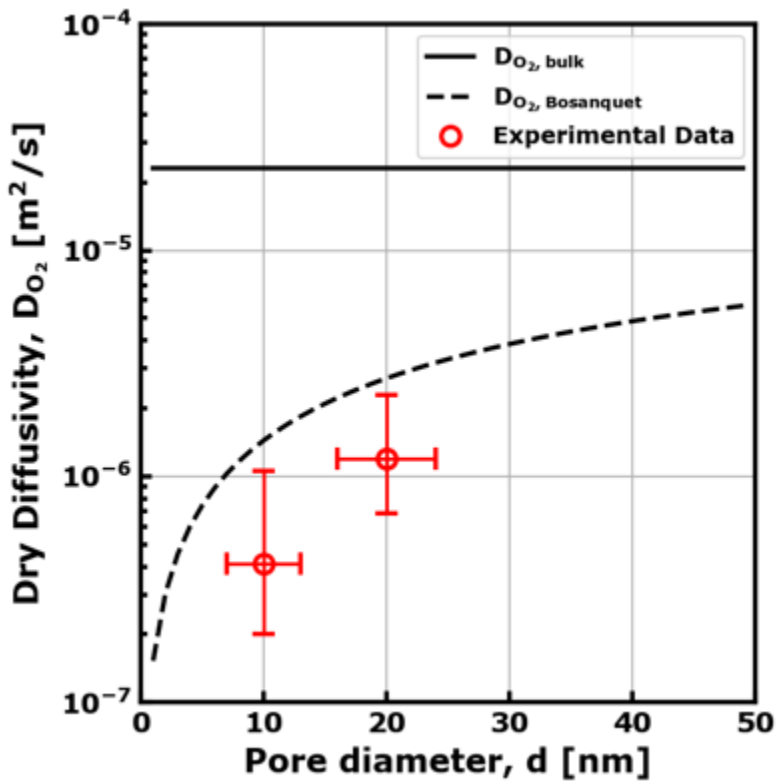

Figure 4.8: Averaged dry diffusivity measurements for isotropic AAO membranes with 10 and 20 nm pores. Note that the vertical error bars on the experimental data points correspond to the high and low limits on the diffusivity measurements resulting from the combined tolerances on the pore size and pore density. The horizontal error bars correspond to the tolerance on the diameter of the pores.

case. We incrementally increased the RH of our sample/cathode gas supply (2% RH per 10 minutes) until the poor filling dynamics shown in Figure 4.7 occurred. The dramatic falloff in output current during the humidified experiment shows the orders of magnitude drop in permeation rate through the porous AAO from the unfilled dry case to the filled case.

Once the pores were completely filled by observing no change in current with increasing RH (all pores are filled), we switched between N_2 and air on the cathode/sample gas supply. The impact of this gas switching can be seen in the inset figure of Figure 4.7, where the current output changes as we switched between N_2 and air. The wet permeabilities measured from the filled-pore experimental sets set are shown in Figure 4.9.

From Figure 4.9, we can see that the measured values of O_2 permeability through the pore-confined water was within an order of magnitude of the bulk water permeability, with the 10 nm sample's vertical error bars (from the same uncertainty in pore area as Figure 4.8) encompassing the bulk value. However, the value for the nominal AAO pore size of 10 nm was slightly larger than the value for the nominal pore size of 20 nm. This is interesting, given that we expected reduced permeabilities for smaller pore sizes, similar to the effect

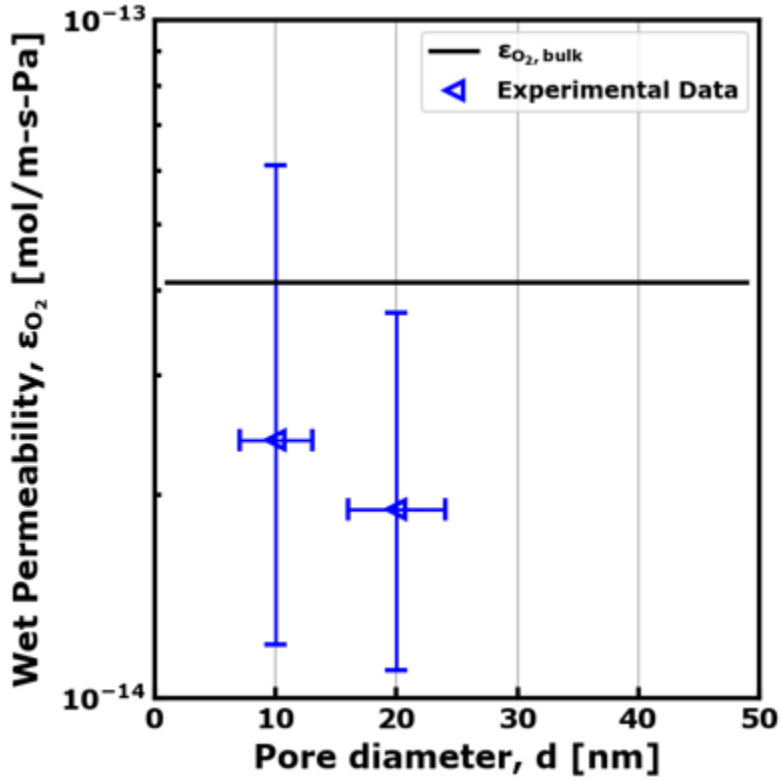

Figure 4.9: Averaged wet (filled pore) permeation measurements for isotropic AAO membranes with 10 and 20 nm pores. Note that the vertical error bars on the experimental data points correspond to the high and low limits on the permeability measurements resulting from the combined tolerances on the pore size and pore density. The horizontal error bars correspond to the tolerance on the diameter of the pores.

of Knudsen diffusivity for dry transport through smaller pores. We will further discuss this increase and its origins in the latter sections of this analysis.

To eliminate the impact of the samples' pore geometries, i.e. the pore size and density, we divided the wet or filled permeabilities by the dry permeabilities, as described by Equation 4.18. This tranport factor, K, is shown for both nominal AAO pore diameters in Figure 4.10.

Expressing the measurements as a ratio of the wet and dry permeabilities allowed for the negation of geometric impacts and the direct comparison of the O_2 transport properties of confined air and water. Clearly, the ratio is much less than one, demonstrating the multiple order of magnitude reduction in permeability going from air to water. Figure 4.10 shows that the 20 nm isotropic AAO sample agrees well with the predicted K value from the bulk permeability of water and Bosanquet formulation of dry diffusivity, showing that the deviation from the expected values of diffusivity and permeability are the same for wet and dry transport.

In contrast, the 10 nm sample deviates from the expected transport ratio value, sitting above

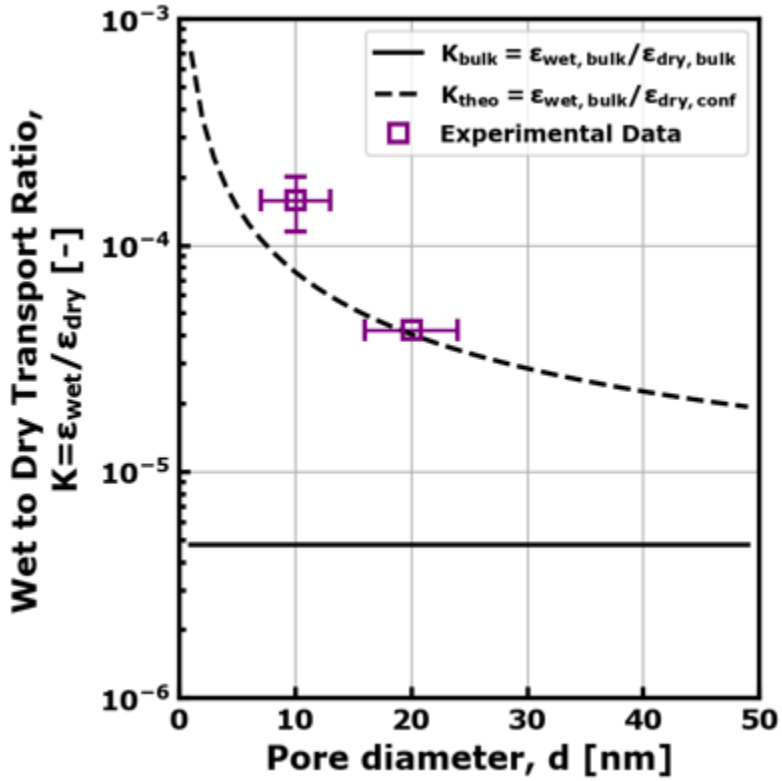

Figure 4.10: Averaged transport ratio between filled (wet) and dry pores. Note that the vertical error bars on the 10 nm experimental data point correspond to the standard deviation from multiple experiments. The horizontal error bars correspond to the tolerance on the nominal diameter of the pores.

K_{theo}. While the 20 nm sample's deviation from the expected trends was consistent between the wet and dry transport measurements, the 10 nm sample's higher permeability and slightly lower diffusivity resulted in placement of the measured transport ratio above the theoretical value. This deviance indicates a change in wet transport properties for this reduced pore size.

There are a couple of possible explanations for the higher transport ratio for the 10 nm AAO sample. The first is the effect of pore wall roughness on the dry diffusivity measurement. The measured dry diffusivity of the 10 nm sample (shown in Figure 4.8) is slightly further from the expected value of the diffusivity from the Bosanquet approximation than the 20 nm dry diffusivity. This could be due to the effect of surface roughness of the AAO membranes' pores. The impact of pore roughness on dry transport has been reported throughout the literature [114, 115, 116], showing hindered self-diffusivities due to increased residence time (effective adsorption) on the surface of the pore wall. To separate this effect from our measurements, we would need to perform experiments with AAO samples with pores in the 1-5 nm range, which at this time are not available commercially in the same configuration as the 10 and 20 nm isotropic AAO membranes used in this study. If the diffusivity deviated in a greater manner for these samples, the roughness effect would be clear and would shed light on the deviation of the 10 nm sample from the expected diffusivity.

The second explanation for the discrepancy in transport ratio for the 10 nm sample is the effect of O_2 adsorption on the pore walls for the water-filled case. The literature on O_2/water interactions in nanoporous media is scarce, but preliminary molecular dynamics (MD) simulations (currently unpublished) have shown preferential adsorption of O_2 to the pore walls in a representative configuration, similar to the studied adsorption of methane to earthen pores [104, 106, 117, 118]. This likely adsorption could increase the overall solubility of the confined water as has been experimentally shown for H_2 in various confined liquids [119], boosting the overall permeability, even if a reduction in the overall diffusivity of O_2 in confined water exists, as has been predicted by MD simulations of similar systems [104, 105, 106, 118]. Further experiments and MD simulations targeted at separating the diffusivity and permeability of O_2, specifically in aluminum oxide confined water would help the understanding of the mechanisms at play in this system.

Comparing our results to the system of interest, i.e. O_2 transport through confined water in carbon micro- and mesopores, we did not observe the vast reduction in permeability expected from the fuel cell limiting current analysis [99]. This is likely due to the different systems; graphitized and ungraphitized carbon in the CLs versus our aluminum oxide system. Ideally, we would have preferred to perform our experiments on carbon porous media, but to the best of our knowledge, well-controlled pore size carbonacious media does not exist. Thus, we had to examine permeation on a system that had well-controlled pores - anodically grown aluminum oxide. With the difference in material, it is not unexpected to see differing permeability trends. Surface adsorption of O_2 is different for different surface structures, roughnesses, etc. Since surface O_2 adsorption directly impacts solubility, it is highly likely that changes in permeability measured experimentally will vary with increasing or decreasing adsorption trends. Again, experimental and numerical work targeted at separating the impacts of diffusivity and solubility of O_2 in confined water would go a long way towards understanding the mechanisms at play in our system.

4.5 Conclusion

In this work, we experimentally analyzed the transport of O_2 through transition-regime pores (10 and 20 nm) using our novel O_2 transport apparatus and AAO membranes with well-controlled pore distributions. We studied both the dry transport through the AAO pores as well as transport through the same pores, filled with water from capillary condensation. We found that the dry transport of our porous AAOs was less than the value predicted from the Bosanquet approximation, likely due to pores that were smaller than expected, but within the AAO's range of pore diameter tolerance. For the wet transport through the water-filled pores, we observed reduced permeation values compared to the bulk value of O_2 permeation through water. However, the 10 nm AAO was found to have a larger permeability than the 20 nm AAO, indicating some mechanistic increase in O_2 transport through the water-filled pores. Combining the wet and dry transports into a dimensionless transport ratio showed excellent agreement between the expected trend and the 20 nm dataset. The

10 nm dataset deviated above the expected trend, indicating improved wet transport. This increase in apparent wet transport properties are likely the impact of O_2 adsorption to the pore walls, which would increase the solubility of the confined water and increases the overall permeability through the product of diffusivity and solubility. Further experimental and modeling analyses are needed to understand this increase in O_2 permeation through confined water-filled pores.

Chapter 5

High Oxygen Permeable Ionomer Integration with State-of-the-Art Catalyst Layers

5.1 Motivation

While recent advances in PEMFC technology have focused on catalyst activity [8, 9, 20, 21] and stability [27, 28, 59], the development of improved carbon supports [8, 9, 59], and membrane degradation mitigation through mechanical [120, 121] and chemical stability additives [66] among many others, little work has been performed to develop CL-specific ionomers. To frame the need for this novel material, we must first compare the functions of the ionomer constituting the PEM and compare it with the ionomer used in the CLs. The purpose of the PEM ionomer is to electrically insulate the ACL from the CCL, conduct protons between the CLs, and prevent gas crossover between electrodes, which lowers the operating voltage of the cell. In the CLs, the ionomer is again responsible for transporting protons, but in contrast to the PEM ionomer, the CL ionomer should promote gas transport to enable high rates of reaction and current generation. While both ionomers are responsible for conductivity, there exists a clear discrepancy in terms of the ionomer and its impact on reactant gas transport, yet the same ionomer (Nafion) has traditionally been the ionomer of choice for both the membrane and CL ionomers.

The use of Nafion as the binder ionomer in PEMFC CLs has had significant performance implications. Two such impacts are the effect of ionomer adsorption poisoning of the catalyst surface [100, 103, 122] and the establishment of a dense region of ionomer in the local vicinity of the Pt [19], both having significant performance impacts at both low and high current densities. At low current densities, ionomer poisoning of the catalyst surface reduces the mass activity, hindering the efficiency of the PEMFC. At high current densities where performance is mass transport limited, the dense ionomer layers near the surface of the Pt catalayst cause significant O_2 transport losses, or R_{O2}'s that inhibit high power performance [30, 63, 64, 74].

These two cases illustrate well the need for CL-specific ionomers, specifically designed for

improved mass activity and permeability. These types of ionomer have undergone research and development in recent years [123, 124, 125], culminating in the rollout of the first generation of high oxygen permeable ionomers, or HOPIs. While these new HOPIs, of which there are several variants made by several companies, have been shown to improve both mass activity and high current density performance [124, 125], little work has been done to study or optimize their integration with state-of-the-art catalysts and carbon supports. This work addresses these key implementation barriers through optimization-driven fabrication and analysis of HOPI-enhanced CCLs.

When considering the impact of an ionomer's O_2 permeability on PEMFC performance, it is important to consider the fundamental processes occurring during permeation. Permeability is defined as the product of a medium's solubility of a solute as well as that solute's diffusivity within the medium. For the case of polymers and more specifically O_2 permeation through an ionomer film, the permeability can be expressed as defined previously (Equation 4.6 from Chapter 4):

$$\varepsilon_{O_2} = S_{O_2} D_{O_2} \tag{5.1}$$

where S_{O_2} is the solubility of O_2 in the ionomer, usually treated as a Henry's law constant and D_{O_2} is the diffusivity of O_2 within the ionomer. Each of these variables has been studied for ionomers within the PEMFC literature [35, 36, 37, 111].

The literature [35, 36, 111] has broken down the interplay of solubility and diffusivity of O_2 in Nafion ionomer systems along with the impact of water uptake on each property. It has been shown that at low water contents, Nafion behaves similarly to raw PTFE; the bulk solubility and diffusivity of O_2 in dry Nafion collapse to the bulk value of PTFE. At high water contents, the solubility and diffusivity approach the bulk value of water and at intermediate water contents, intermediary values of solubility, diffusivity, and overall permeability have been observed. This dependence on water content illustrates the interplay of the hydrophilic and hydrophobic domains' impact on O_2 transport. As the water content is reduced, the hydrophilic domains shrink, causing the ionomer's structure to be dominated by the hydrophobic PTFE backbone structure. With water uptake, the hydrophilic domains swell, causing the structure of the ionomer to then be dominated by the water domain. Thus, the O_2 transport properties follow these phase segregation trends, impacting the ORR rate and performance.

The new HOPI class of ionomers are designed to prevent ionomer domain collapse by integrating blocky monomer units with the backbone of the ionomer chains [124, 126, 127]. These blocky units result in a stiffer hydrophobic matrix that resists chain packing and hydrophilic domain suppression. Preventing collapse of the hydrophobic domain is important as it expands the domain that has been shown to have a high O_2 solubility compared with the hydrophilic domain [111]. The blocky monomers in the backbone of the HOPI also help prevent collapse of the hydrophilic domains that are the primary O_2 diffusion pathway[111].

We can project the impact of the HOPI structure on the individual effects of O_2 solubility

and diffusivity on PEMFC performance within the specific operating ranges of interest, i.e. low current, high efficiency and the high current, high power operating points. Consider the schematic of O_2 concentration as a function of position above the catalyst surface in Figure 5.1 a), with b) and c) representing the idealized O_2 concentration profiles under low and high current densities, respectively.

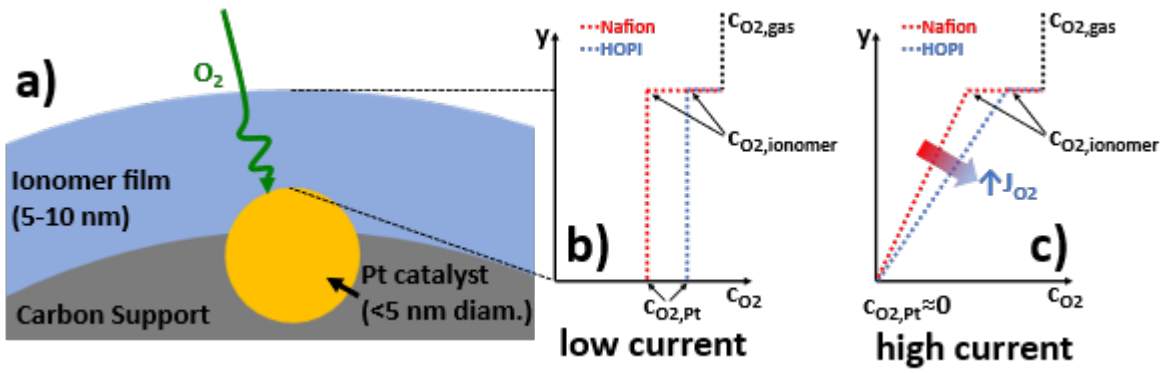

Figure 5.1: a) Schematic of O_2 transport through the ionomer in PEMFC CCLs and corresponding O_2 concentration profiles through the ionomer for b) low currents and c) high currents.

For the low current operation case shown in Figure 5.1b where the mass transport of O_2 is not significantly hindered, the O_2 concentration across the ionomer is uniform. Thus, with a higher solubility of O_2 through the use of the HOPI (smaller drop in O_2 concentration from the gaseous phase), a higher O_2 concentration is available at the Pt surface. This increase in local O_2 concentration results in an apparent increase in mass activity, with no inherent structural change to the catalyst, causing an increase in the current output at a specific voltage. The increase in current resulting from the increased solubility of O_2 can be shown with a simple expression for reaction rate [128] where an increase in the concentration of the reactant at the reacting surface, c_i^*, increases the current, I:

$$I = nFc_i^* f_i \exp^{-\Delta G^{++}/RT} \tag{5.2}$$

where n is the number of electrons transferred in the reaction, F is Faraday's constant, c_i^* is the concentration of the reactant specie at the electrode surface, f_i is the rate of the activated specie producing product, ΔG^{++} is the activation energy of the process, and R and T are the universal gas constant and temperature, respectively.

For the high current region shown in Figure 5.1c, the rate of O_2 delivery to the surface of the Pt becomes significantly more important than in the low current case. Thus, an increase in the diffusivity of O_2 through the ionomer, in addition to the improved solubility, increases the overall O_2 flux to the surface of the Pt (J_{O_2}) and increases the rate of reaction/current. With an increase in permeability of O_2, we anticipate improved performance through the full range of the polarization curve due to improved solubility and an additional improvement

at high current density due to the reduced diffusive resistance.

Several experimental studies have demonstrated these improvements, notably the work by Uchida's group at the Fuel Cell Nanomaterials Center in Japan [125]. In their work, they have shown the development of two different HOPI ionomers as well as their performance in operating fuel cells, which showed significant performance improvement at both the low and high current density regions. Further, they correlated their improved polarization data with measured increases in the apparent mass activities for both HOPIs and improved oxygen transport at high current densities as shown in their high frequency resistance (HFR)-free air/H_2 polarization curves.

In our work, we are using the HOPI developed by our project partner, Chemours [127]. Again, this novel material consists of a bulky monomer backbone aimed towards preventing backbone collapse and chain packing for the improvement of O_2 solubility. This chain packing prevention is also suspected to positively impact diffusion through suppressing of hydrophilic domain collapse at low RH, cation contamination, or local confinement effects. In addition, Chemours' HOPI utilizes a short side chain chemistry as opposed to traditional Nafion's long side chain chemistry. Long side chain chemistries have been shown to cause adsorption to the Pt surface, essentially poisoning the catalyst and preventing ORR at those locations [100, 103, 122]. Reducing the length of the side chain with the HOPI seeks to address this concern [101, 102], ideally improving Pt utilization and mass activity, in addition to the O_2 permeability impacts. Our efforts were aimed at evaluating and optimizing the performance of this new ionomer with in-situ PEMFC electrochemical testing and diagnostics.

5.2 Experimental

5.2.1 MEA Fabrication

The CCL inks were prepared by mixing the carbon-supported Pt with a combination of water and alcohol (isopropanol or n-propanol) and then adding the ionomer dispersion drop by drop to the vial. The catalysts used were a Johnson Matthey HiSPEC 4000 (40 wt % Pt on Vulcan carbon, Pt/Vu) and a TKK EA50 (45.6 wt % Pt on low surface area carbon, Pt/LSAC). Pt/Vu and Pt/LSAC were chosen as the catalyst/supports of choice for these preliminary experiments, as they maximize the Pt/ionomer interfacial area, compared with Pt/HSC, which eliminates much of the contact [8, 9]. The ionomer dispersions used were D2020 (1000 EW, 20 wt % Nafion), DE2029 (800 EW, 20 wt % Nafion), and Chemours' HOPI (870 EW, 10 wt %). The quantities of each constituent were measured by weight to achieve specific solvent ratios, ionomer to carbon ratios (I/C), and solids weight percent (wt %) in the ink. Consistent with traditional fabrication methods [129, 130], we fabricated our inks with 10-15 wt % solids depending on the type of ionomer. During component addition, the inks were mixed with an IKA Lab Dancer vortex mixer (Staufen, Germany) and subsequently sonicated for 10 seconds with a Branson SFX250 tip sonicator (Brookfield, CT) at 15% power and then bath sonicated for 20 minutes [131]. During both sonication processes, the inks were held in temperature equilibrium with ice water to prevent Pt detachment and

ECSA loss.

Once finished sonicating, the inks were deposited on a microtextured silicone decal substrate from 3M (Saint Paul, MN) with film applicators of varying thickness (100-150 µm) and a low shear rate of 10-11 mm/s, with an MTI film coater (Richmond, CA). The CLs were dried under ambient conditions before being transferred to pre-manufactured catalyst coated membranes (CCMs) supplied by IonPower (New Castle, DE), consisting of a Nafion HP membrane with a 0.3 mg_{Pt}/cm^2 ACL with a 2.6 x 2.6 cm area. The decal transfer consisted of hot pressing a 5 cm^2 area of the decal-backed CL to the CCM at 2.7 MPa, 130°C for 8 minutes, rotating the MEA 90° every two minutes. A thick silicone sheet was used below the MEA during the hot-pressing process to distribute the pressure evenly over the full 5 cm^2 area. After 8 minutes in the press, the microtextured silicone decal backing layer was removed while the MEA was still hot, yielding consistent 100% transfers to the membrane. An example of the transfer after the hot-press is shown in Figure 5.2.

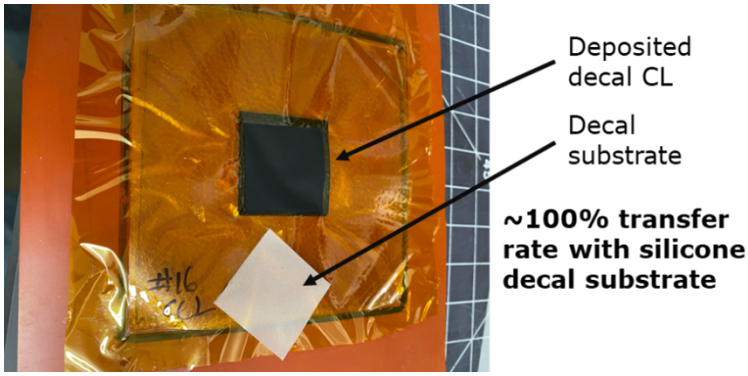

Figure 5.2: Freshly hot-pressed CL with empty decal substrate showing 100% transfer.

The fabricated MEA was supported with 4 mil (100 µm) adhesive-backed Kapton sheets from McMaster Carr (Elmhurst, IL) and gasketed with 3 mil PTFE from the Fuel Cell Store (College Station, TX). We used Sigracet 22 BB GDLs from the Fuel Cell Store, yielding a GDL compression of approximately 20%. For the cell hardware, we used a Scribner (Southern Pines, SC) 5 cm^2 single-channel serpentine flow plate for the anode and an in-house designed differential-style flow plate with 21 parallel channels for the cathode. The Scribner hardware was all torqued to 40 in-lbs before being tested on our Scribner 850e test stand.

5.2.2 Electrochemical Testing

To achieve peak performance with which to compare between MEAs, we utilized the detailed break-in and VR protocols from Kabir et al [132]. They showed that for Pt/Vu cathodes, peak mass activity and stable non-Fickian R_{O2}'s or R_{NF}'s were achieved after a wet/dry/wet break-in cycle and 2-3 subsequent voltage recovery (VR) cycles. These VR cycles are commonly used throughout the literature but were originally described by the General Motors patent [133]. In our experiments, we used wet (100% RH) and dry (32% RH) voltage cycling

at 80°C for the initial break-in sequence and low temperature (40°C), high relative humidity (150% RH) low voltage holds for the VR sequence. After these protocols, we took our anodic air and O_2 polarization curves using 4 minute holds at each current density (air) and voltage (O_2), followed by H_2 crossover measurements via linear sweep voltammetry (LSV) per the USFCC protocols [134], and electrochemical impedance spectroscopy (EIS) for the CCL resistance as described my Makharia et al [95]. After completing the aforementioned experiments, we cooled the cell down to 30°C, 100% RH overnight under low N_2/N_2 flow rates.

The following day, we took a cyclic voltammogram (CV) from which we calculated the ECSA and roughness factor (RF) for each CCL. After the CV, we warmed the cell up to 80°C to take limiting current measurements at 25, 50, 75, and 90% RH for the calculation of the R_{NF}'s as described by Baker et al. [74]. In addition, we took CV data at each limiting current RH to ensure that we were comparing the R_{NF} for consistent RFs, i.e. not losing access to Pt as a function of RH. The full experimental set, including electrochemical protocols and diagnostics for performance, characterization, and diagnostics are outlined in Figure 5.3.

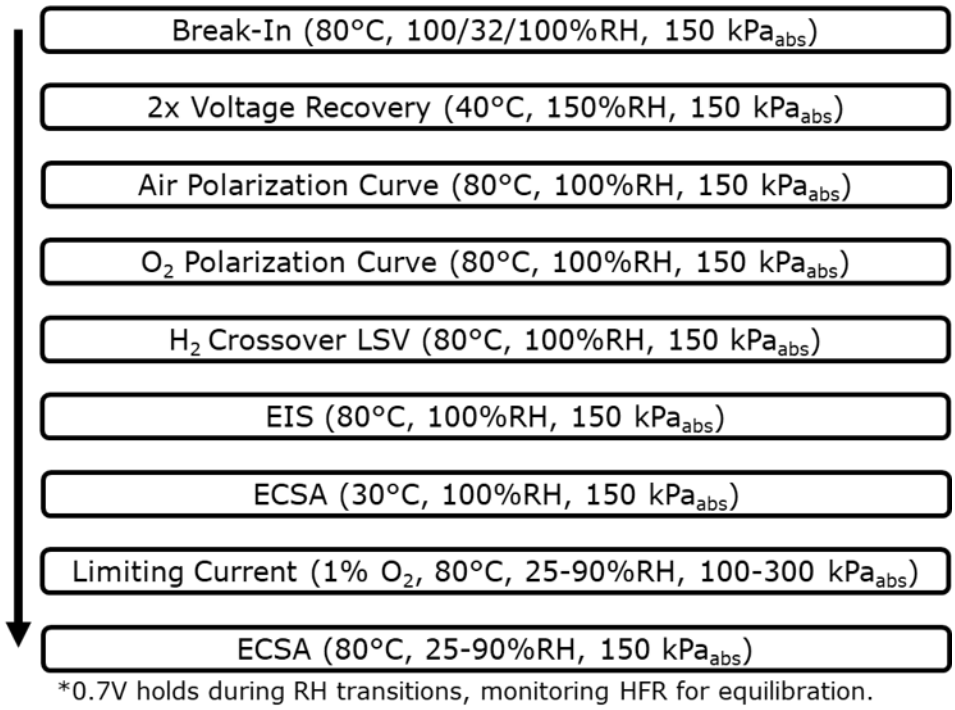

Figure 5.3: Full electrochemical conditioning and maximum performance protocol.

5.2.3 Effect of Break-In and Conditioning on Performance

We performed initial testing to evaluate the impact of our break-in and conditioning sequences on performance. Using the work of Kabir et al. [132], we subjected our cells to wet/dry/wet (100/32/100% RH) voltage cycling at 80°C. This initial cycling is shown in Figure 5.4. Clearly, the 0.6 V current increases during the initial wet cycling, followed by a marked increase post-dry-cycle and plateauing near 1.25 A/cm^2 at the end of the protocol.

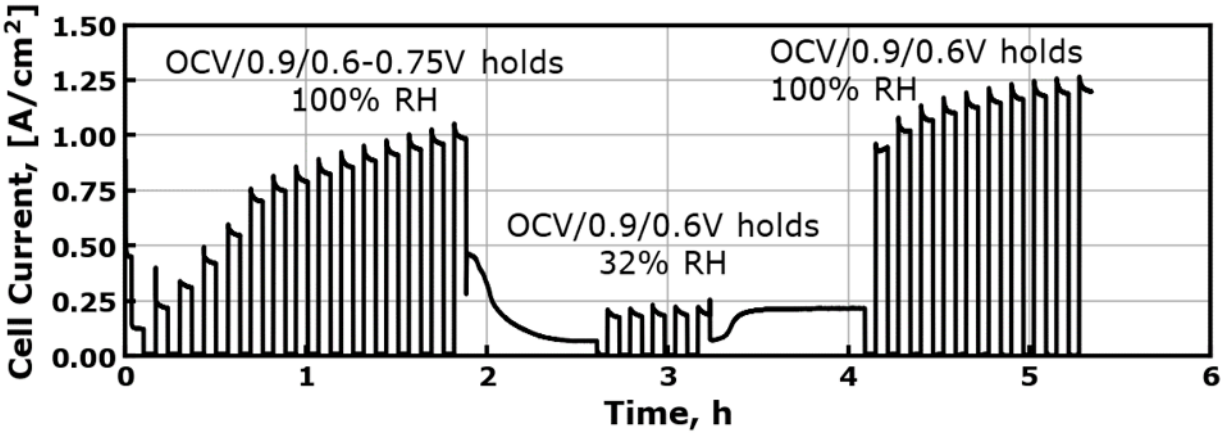

Figure 5.4: Wet/dry/wet voltage cycling during break-in protocol. Break-in protocol was performed at 80°C, 100/32/100% RH, and 150 kPa$_{tot}$ under air/H_2 at 2/1 SLPM.

After the break-in cycling, we cooled the cell down to 40°C and 150% RH for the VR cycles. The VR cycles consisted of a 5 minute 0.85 V hold, a 10 min 0.6 V hold, and a one-hour 0.1 V hold. Two of these sequences were considered a single VR cycle, i.e. one VR cycle consisted of two Voltage hold sequences. The Scribner fuel cell hardware's insulation was removed for the VR cycles to allow for heat dissipation, especially for the 0.1 V holds, where the specific current frequently exceeded 2.5-3 A/cm^2. CPU fans were also utilized to force convective heat dissipation from the hardware during these cycles. The current at each Voltage hold was recorded as a function of time and averaged over the last minute of each hold and the results are shown in Figure 5.5.

Our VR cycle currents stabilized after 2 full VR cycles (total of 4 Voltage cycling sequences), even while the overall ECSA decreased as shown by the CVs of Figure 5.6a and the RF calculations from integration of the H_2 underpotential deposition (UPD) regions of the CVs in Figure 5.6b. These results were consistent with the analysis of Kabir et al. [132] that showed maximum mass activity and stabilized R_{NF}'s were achieved for Pt/Vu CCLs after 2-3 VR cycles. We used these break-in and VR protocols to condition each of our MEAs for peak performance to allow for comparison between MEAs.

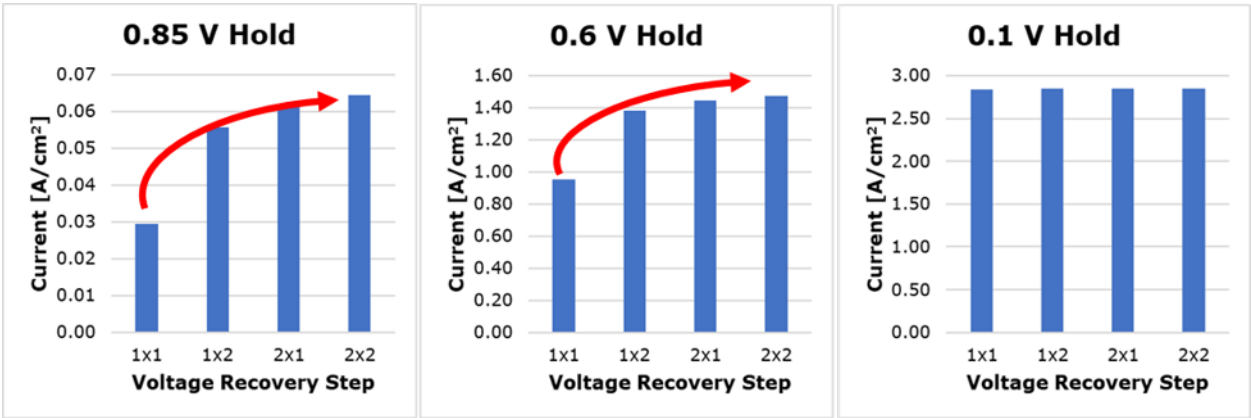

Figure 5.5: Example measured currents for each Voltage hold during the VR cycles for a Pt/Vu and HOPI CCL. Note the plateauing of the current densities with increasing VR steps, indicating maximum achieved mass activity. VR cycles were performed at 40°C, 150% RH, and 150 kPa_{tot} under air/H_2 flow at 2/1 SLPM.

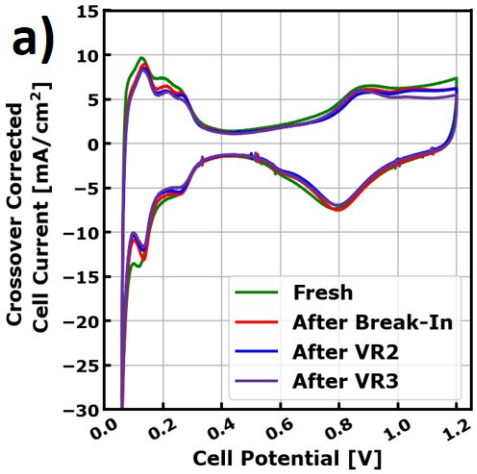

b)

Cell State	RF
Fresh	132
After Break-In	117
After VR2	110
After VR3	108

Figure 5.6: a) CVs of Pt/Vu and HOPI CCL as a function of break-in and VR protocols and b) calculated RFs from the UPD regions of the CVs. CVs were taken at 30°C, 100% RH, 150 kPa_{tot} under N_2/H_2 flow at 0.05/0.1 SLPM and a sweep rate of 50 mV/s.

5.3 Results

5.3.1 Benchmarking

The first set of comparisons we performed was between the HOPI-based CCLs and the traditional Nafion-based CCLs. We examined two different Nafion ionomers, one with 1000 EW (D2020) and one with 880 EW (DE2029) to compare with the low EW HOPI (870 EW). We held the ionomer to carbon ratio (I/C) constant at 0.6 and mixed the inks with high alcohol concentrations (IPA to water ratios greater than 5). We used the Johnson Matthey HiSPEC 4000 (40 wt % Pt on Vulcan carbon) for each ink and mixed them with 10 wt % solids (solid ionomer, carbon, and Pt). The MEAs were assembled as described in the Experimental section and the Pt loadings were determined gravimetrically to be 0.22 ± 0.02 mg_{Pt}/cm^2. Each MEA was tested according to the protocols outlined in Figure 5.3.

Figure 5.7 shows the CVs for the D2020, DE2029, and HOPI-based CCLs. From integration of the UPD regions of the CVs, we attained RF values around 100 for our loadings of 0.22 mg_{Pt}/cm^2. The O_2 and air polarization curves are shown in Figure 5.8. The specific activities were extracted from the HFR and H_2 crossover corrected 0.9 V holds of the O_2 polarization curve, as is common throughout the literature. Table 5.1 shows the measured specific activities as well as the RFs for each ionomer-based CCL.

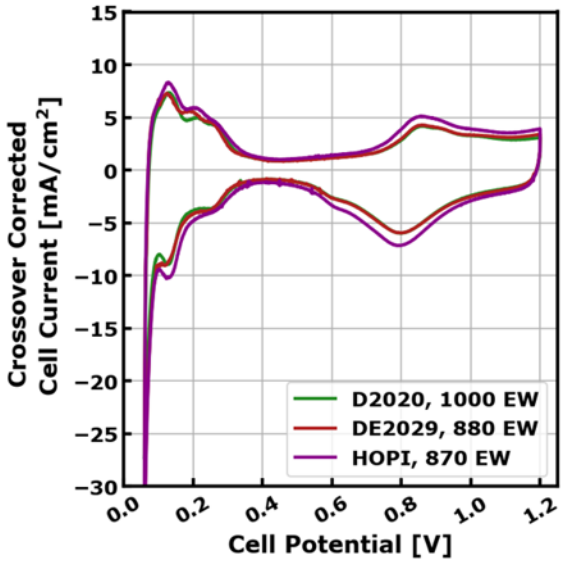

Figure 5.7: CV of D2020, DE2029, and HOPI-based CLs. CVs were performed after the second VR cycle at 30°C, 100% RH, 100 kPa_{tot}, and N_2/H_2 at 0.05/0.1 SLPM. Pt loadings were 0.22±0.02 mg_{Pt}/cm^2.

From Figure 5.8, we can see that the HOPI ionomer outperformed both configurations of the Nafion ionomer in both the activation region (low current – O_2 polarization curve) and at higher current densities with air, where we begin to see a divergence in the performance at 1-1.5 A/cm^2. While the HOPI did have the highest RF, corresponding to a slightly

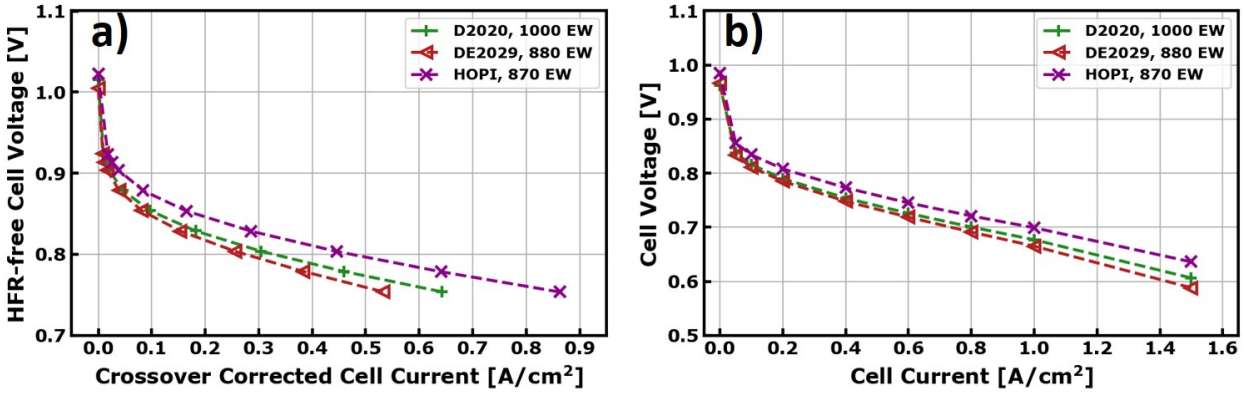

Figure 5.8: Benchmarking polarization curves for D2020, DE2029, and HOPI-based CCLs under a) O_2/H_2 and b) air/H_2. Both polarization curves were taken in the anodic direction (high current to low current). Polarization curves were taken at 80°C, 100% RH, at 150 kPa_{tot} under flow rates of 2/1 SLPM to the cathode and anode, respectively.

Table 5.1: Roughness factor (RF) and specific activity data for the CCLs using D2020, DE2029, and HOPI ionomers.

Cathode Ionomer, EW	RF	Specific Activity [mA/cm^2_{Pt}]
D2020, 1000 EW	95	0.21
DE2029, 880 EW	101	0.17
HOPI, 870 EW	111	0.35

higher overall Pt loading and ECSA, the specific activity was still greater than either the D2020 or DE2029 Nafion-based CCLs, as shown in Figure 5.9 where the RF-normalized 0.9 V currents, or specific activity, are plotted. This improvement in the apparent specific activity for the HOPI (67% increase, compared to D2020) carries through the full span of the polarization curve, out to high current density. While the origins of the increase in measured specific activity are most likely the interplay of the short side chain ionomer and improved O_2 solubility, further work is needed to explicitly decouple their impacts on activity.

Also important to note is the difference in performance between the two Nafion CCLs (D2020 and DE2029). The D2020 outperformed the lower EW DE2029 in the low current density region, as confirmed by the higher specific activity shown for D2020 compared to DE2029 in Figure 5.9. This is due to the lower EW DE2029 (more side chains and functional groups) causing more ionomer adsorption poisoning of the Pt surface compared with D2020, which has fewer side chains and functional groups per gram of total polymer. The lower specific activity of the 880 EW Nafion (DE2029) CCL translated through the full length of the polarization curve, performing worse than its higher EW counterpart.

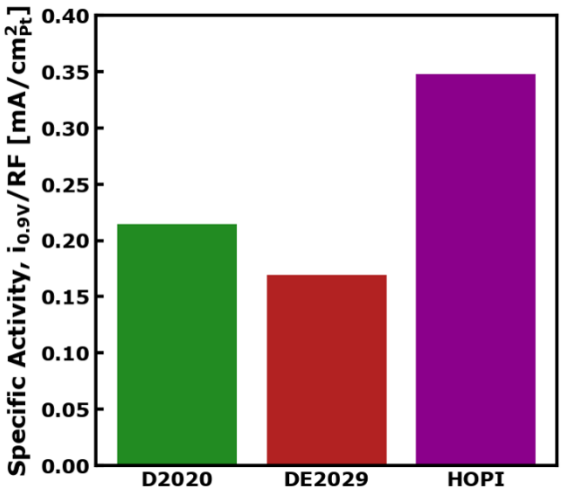

Figure 5.9: Specific activity of CCLs fabricated with D2020, DE2029, and HOPI ionomers. The specific activities were extracted from the corrected 0.9 V currents from the O_2 polarization curves in Figure 5.8a.

To confirm the improved R_{O2} for the HOPI CCL at high current density (Figure 5.8b), we took limiting current O_2 transport measurements using the method of Baker et al. [74] at RHs between 25 and 75%. These results are shown in Figure 5.10, along with the CVs at each RH (all at 80°C) to confirm that the CCLs weren't losing ECSA at lower RHs, which would have made comparisons between R_{NF}'s at different RHs incorrect. As can be seen in the CV data of Figure 5.10a-c, no observable loss in ECSA occurred at low RH for any of the CCLs we tested. This was also good confirmation that the ionomer was well-distributed for each of our CCLs, as with poor ionomer coverage, the Pt would have only been accessible under high RH operation where liquid water is present to allow protons to access the surface of the Pt catalysts.

Figure 5.10d shows the R_{NF} trends versus RH for each of the ionomers used in this study. As expected from the air polarization curve in Figure 5.8b, the HOPI ionomer exhibited a reduced R_{NF} across all RHs tested, demonstrating the improvement in O_2 permeability compared with its Nafion counterparts. For traditional ionomers like Nafion, the R_{NF} is extremely sensitive to the RH, again due to the expansion or contraction of the hydrophilic domains that are critical for O_2 transport. The two Nafion ionomers demonstrate this phenomenon well. The DE2029 ionomer is a low EW Nafion ionomer, meaning that there are a greater number of polar sulfonate groups per gram of ionomer compared with the higher EW D2020. As a result of the increased number of sulfonate groups, the overall phase segregation between hydrophilic and hydrophobic domains is greater for the DE2029 ionomer, helping to resist domain collapse with dehydration. This is confirmed by the DE2029 having a lower R_{NF} than the D2020 for all RHs tested even as the difference between R_{NF} values for D2020 and DE2029 is reduced at high RH as the hydrophilic domains of the D2020 expand to the limit of the DE2029. The HOPI resists this RH dependence, consistent with the overall rationale for implementing these ionomers, i.e. the bulky monomers prevent hy-

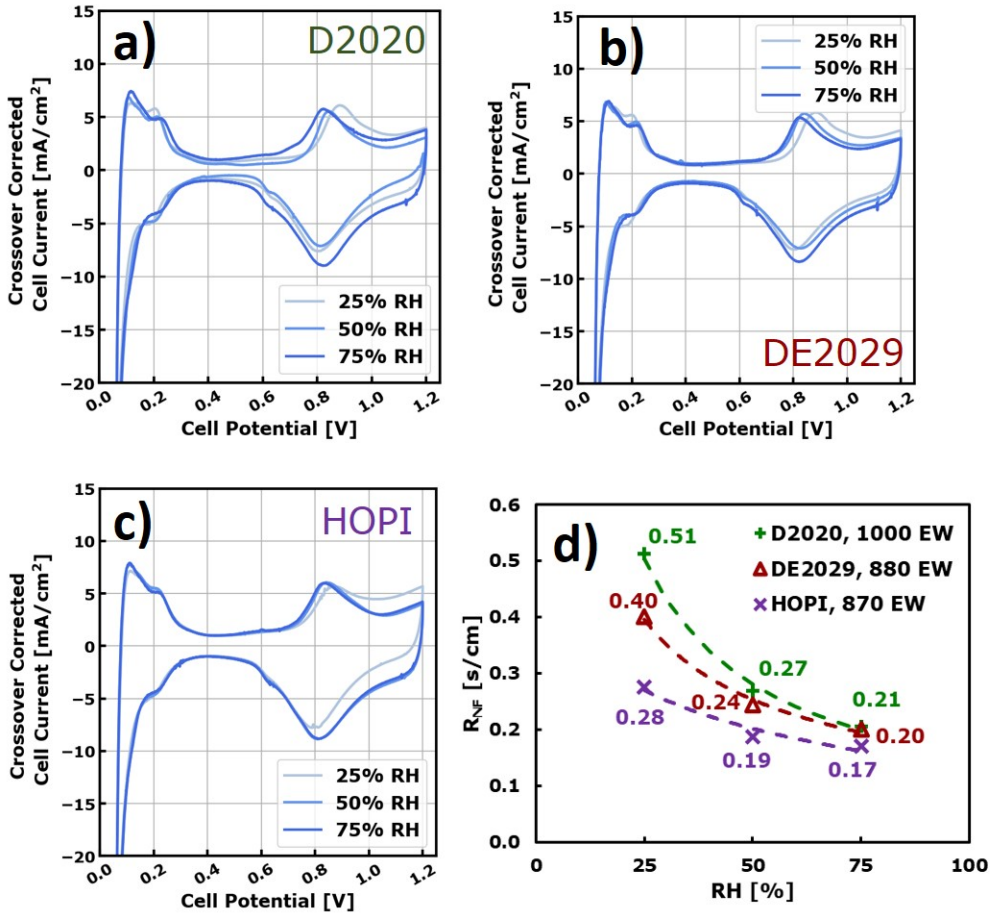

Figure 5.10: a-c) CVs of the D2020, DE2029, and HOPI-based CCLs at each limiting current RH. D) Non-Fickian O_2 transport resistance (R_{NF}) as a function of RH. Limiting current data was taken at 80°C, 25-75%RH, 100-300 kPatot under 1% O_2/H_2 at 2/1 SLPM. Note that the dashed lines of d) are intended only as a guide for the eyes and should not be interpreted to have physical meaning.

drophilic/hydrophobic domain collapse and thus prevent significant differences in the R_{NF} due to RH changes. This domain collapse resistance has important implications for automotive PEMFCs, as it would allow them to run at sub-saturated RH conditions that are optimal in other regards (i.e. water retention, humidification, etc.)

In addition to our electrochemical measurements, we also performed SEM analysis of the as-fabricated CCLs to examine the size of the carbon agglomerates and the ionomer distribution. The SEM images of the D2020, DE2029, and HOPI-based CLs are shown in Figure 5.11. We can see from the microstructure SEMs (Figure 5.11d-f) that the HOPI-based CL has the smallest and most uniform carbon agglomerate size and pore structure. The D2020 sample had slightly larger particles and less uniform pores, and the DE2029 had the largest and most irregular features. In terms of the ionomer distributions, no ionomer bridging features can be found in any of the SEMs, consistent with the CVs at each RH (Figure 5.10a-c)

that showed no loss in ECSA at lower RH. The macroscopic surfaces of the as-fabricated decal CLs (Figure 5.11a-c) showed significant mud-cracking for the HOPI, compared with the less-cracked D2020 sample, and nearly pristine DE2029 sample. These cracking features for the HOPI-based CL present a serious durability concern, as cracks are one of the primary features responsible for CCL degradation during AST cycling.

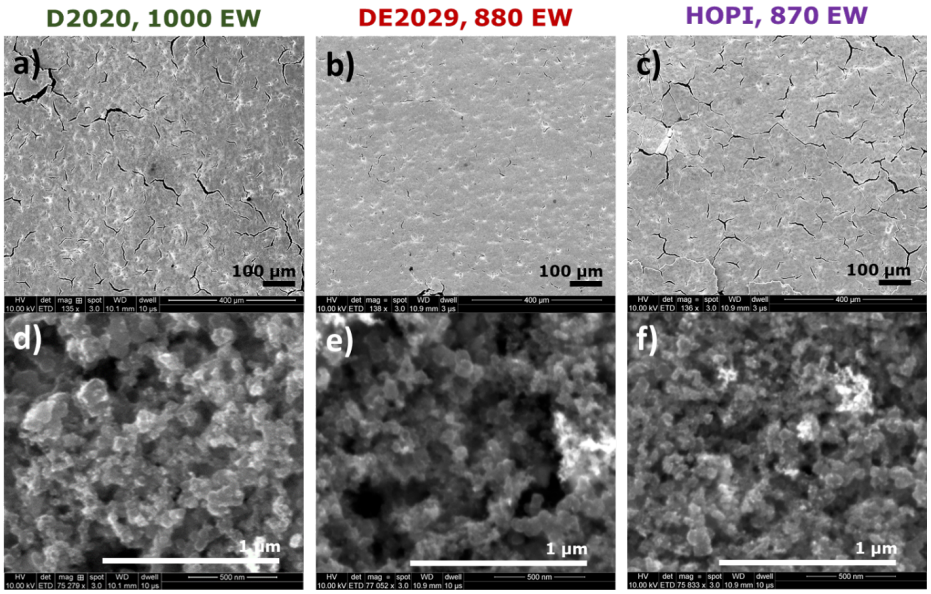

Figure 5.11: SEMs from the surfaces of as-fabricated decal CCLs. a-c) Macroscopic surfaces of D2020, DE2029, and HOPI-based CCLs, respectively. d-f) Microstructures of D2020, DE2029, and HOPI-based CCLs, respectively.

5.3.2 Ink Solvent Optimization

The literature on CCL ink fabrication and performance is considerable, with many variations of fabrication methods, material selections, etc. One variable that is oft considered when seeking peak performance is solvent composition. Within the literature, the two most commonly used solvents are alcohols (n-propanol or isopropanol) and water, as well as mixes of the two. Numerous works have characterized the impacts of varying ratios of these two solvents, ultimately indicating some 'optimal' configuration with regard to the property of interest, including carbon agglomerate size, ionomer distribution, degree of ionomer phase segregation, etc. In this portion of our study, we varied the n-propanol to water ratio of HOPI and D2020-based CCL inks to find the 'optimal' solvent for the HOPI system and compare it with similar CCLs fabricated from traditional D2020. It is important to note that in this analysis, we used the TKK Pt/LSAC catalyst/support combination instead of the HiSPEC Pt/Vu from the benchmarking study.

By changing the solvent's nPA to water ratios, we effectively changed the dielectric constant of the solvent, which has significant implications for the colloidal behavior of the ionomer, Pt, and carbon as well as the final dried structure of the CCLs. In this study, we chose nPA and water due to their prevalence in the literature. We used nPA to water ratios of 5:1, 2.3:1, and 1:1 for the HOPI and 5:1 and 1:1 for D2020, but didn't test any higher water content inks, due to their propensity to flaking off of the decal substrate. Figure 5.12 shows the CVs of each CCL corresponding to the abovementioned nPA to water ratios. The corresponding RF measurements are shown in Table 5.2, along with the specific activities calculated from the HFR and H_2 crossover corrected 0.9 V currents from the O_2 polarization curve shown in Figure 5.13a. Figure 5.13b shows the corresponding air polarization curve and Figure 5.14 contains the graphical data for specific activity.

From Figure 5.12 and Table 5.2, we can see that the RF values were consistent between cells prepared with the various solvent composition, showing little impact of the solvent on the ECSA/RF. The specific activities of the HOPI and D2020 CLs were also consistent within ionomer type, resulting in nearly identical low current density performance for each ionomer class from the O_2 polarization curves (Figure 5.13a). Between ionomers, the HOPI-based CCLs again outperformed the D2020-based CCLs with an 85% increase in the specific activity. This increase was consistent with the benchmarking analysis that showed roughly a 67% increase from the D2020 to HOPI specific activities. It is important to note that the specific activities of the TKK Pt/LSAC catalyst/support are lower than those of the HiSPEC Pt/Vu catalyst. This is likely due to the higher overall surface area of the Vu support and incorporation of some mesoporosity that protects the Pt from the ionomer. The LSAC support has less mesoporosity and all of the Pt catalyst sites are in direct contact with the ionomer. As a result, the percent increase in specific activity we see going from D2020 to the HOPI is greater for the LSAC support compared with the Vu. While we do see an improvement in specific activity and low current density performance, again, more work is needed to separate the impacts of the short side chain HOPI from the suspected increase in O_2 solubility.

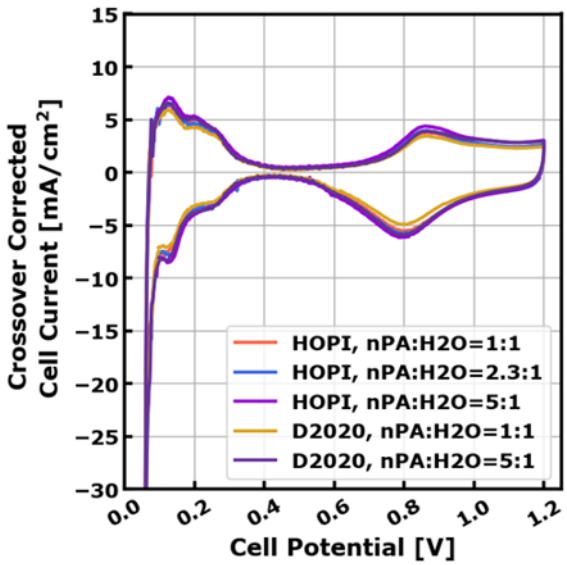

Figure 5.12: CVs of HOPI and D2020 CCLs fabricated with varying nPA to water solvent ratios. CVs were collected at 30°C, 100% RH, 150 kPa_{tot} under N_2/H_2 at 0.05/0.1 SLPM.

Table 5.2: Roughness factor (RF) and specific activity data for HOPI and D2020 CCLs fabricated from inks using various nPA to water solvent ratios.

Ionomer, Solvent Ratio ($nPA:H_2O$)	RF	Spec. Activity [mA/cm^2_{Pt}]
HOPI, 1:1	102	0.23
HOPI, 2.3:1	102	0.25
HOPI, 5:1	110	0.23
D2020, 1:1	96	0.12
D2020, 5:1	105	0.13

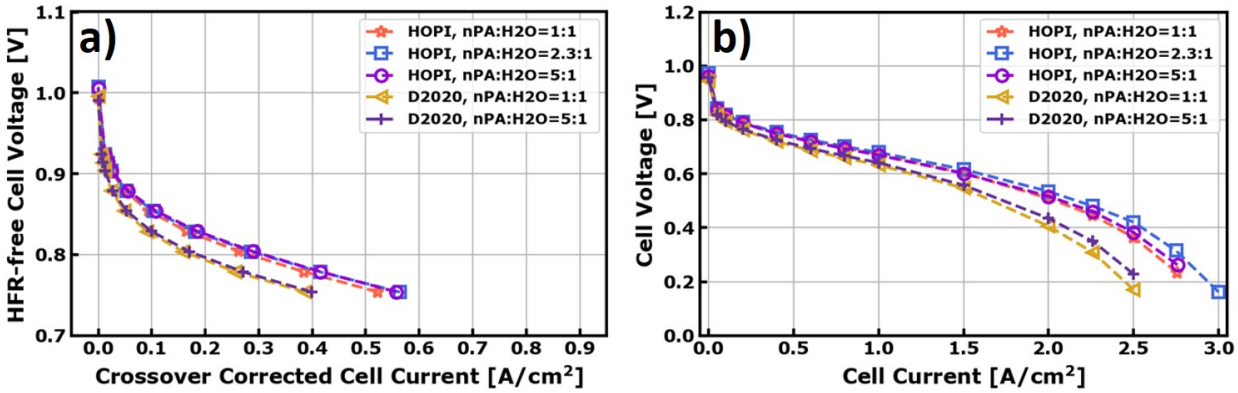

Figure 5.13: Polarization curves from varying solvent composition study under a) O_2/H_2 and b) air/H_2. Both polarization curves were taken in the anodic direction (high current to low current). Polarization curves were taken at 80°C, 100% RH, at 150 kPa_{tot} under flow rates of 2/1 SLPM to the cathode and anode, respectively.

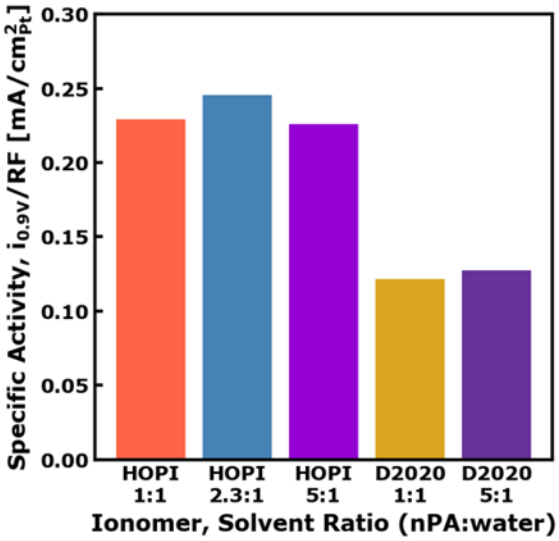

Figure 5.14: Specific activity measurements of HOPI and D2020-based CCLs with various nPA:water solvent ratios.

Examining the air polarization curve in 5.13b, we again observe the improvement in high current density performance with the HOPI-based CLs, for all solvent compositions. This is the result of the HOPI's improved specific activity as well as some apparent improvement in the R_{O2}. Within each group of CCLs, we saw consistent performance out to approximately 2 A/cm^2, consistent with each ionomer's similar measured specific activities. At higher current densities ($>$ 2 A/cm^2) we began to observe some deviation between the CCLs fabricated from the same ionomers, indicating changes in the R_{O2} resulting from the solvent composition. Overall, the nPA to water ratio of 2.3:1 for the HOPI CCL outperformed both the higher and lower alcohol content solvents and ultimately achieved 3 A/cm^2. The HOPI CCL with a high alcohol content solvent (5:1) performed better than the low alcohol content solvent

(1:1), consistent with the D2020 results where the 5:1 solvent performed better than the 1:1 solvent. These changes in performance at high current density indicated improvements in the O_2 transport. To further examine the changes in O_2 transport capability, we performed limiting current analyses as before, here varying the RH between 50 and 90% to better capture the R_{NF} trends near our polarization curve operating RH of 100%, without flooding the system. The R_{NF} versus RH results are shown in Figure 5.15.

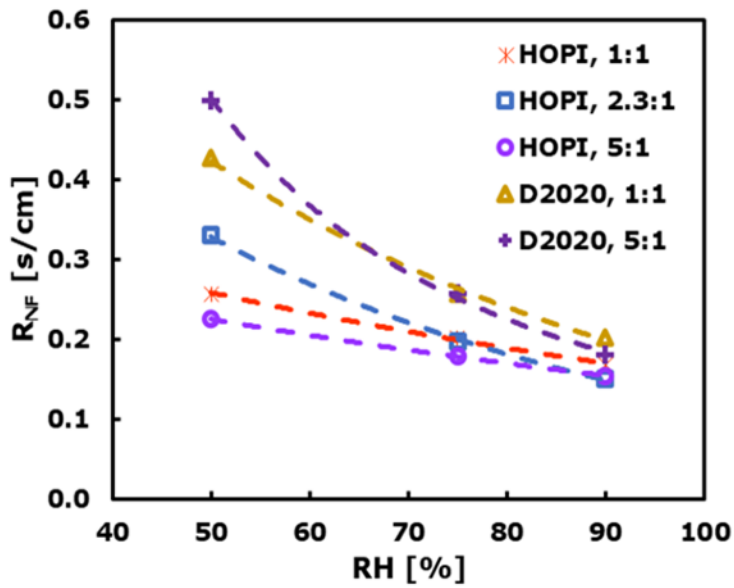

Figure 5.15: Non-Fickian O_2 transport resistance (R_{NF}) as a function of RH for CCLs prepared with varying solvents. Limiting current data was taken at 80°C, 50-90%RH, 100-300 kPa_{tot} under 1% O_2/H_2 at 2/1 SLPM. Note that the dashed lines are intended only as a guide for the eyes and should not be interpreted to have physical meaning.

From Figure 5.15, we can see that the trends in the R_{NF} are consistent with the air/H_2 polarization data for currents greater than 2 A/cm^2. The nPA:water ratio of 2.3:1 had the lowest R_{NF} at 90% RH (and overall trend projected to 100% RH) compared with the high and low alcohol contents. The HOPI with a solvent ratio of 5:1 performed better than the 1:1 at 90% RH, consistent with the D2020 CLs, for which the ratio of 5:1 performed better than the ratio of 1:1. The overall HOPI R_{NF} trends with RH were surprising, with the low and high nPA ratios having similar R_{NF} trends with RH, and the moderate nPA ratio having a significantly different, steeper trajectory. This indicates changes in the corresponding inks' colloidal interactions, impacting the final structure of the ionomer within the CCL. Further experimentation is necessary to determine the specifics of these colloidal interactions and their impact on overall ionomer and CCL structure.

For each RH at which the limiting current and R_{NF} data was collected in Figure 5.15, we collected the CVs (not shown) and observed no loss in ECSA within the range of RHs tested. This again indicated complete ionomer coverage of the Pt catalyst. To compare ionomer distributions, we took SEMs of the microstructures of each of the fabricated HOPI CCLs, as

shown in Figure 5.16a-c. From the SEM images, we can see consistent, small primary carbon particles and well-distributed ionomer. However, the lower alcohol content CCLs, i.e. 1:1 and 2.3:1 nPA:water ratios show some ionomer bridging (circled in red) that isn't present in the highest alcohol content solvent (5:1). This again indicates differences in colloidal properties that impact ionomer final distributions and agglomerations, even while the primary carbon particles retain consistent shape and size, regardless of solvent composition.

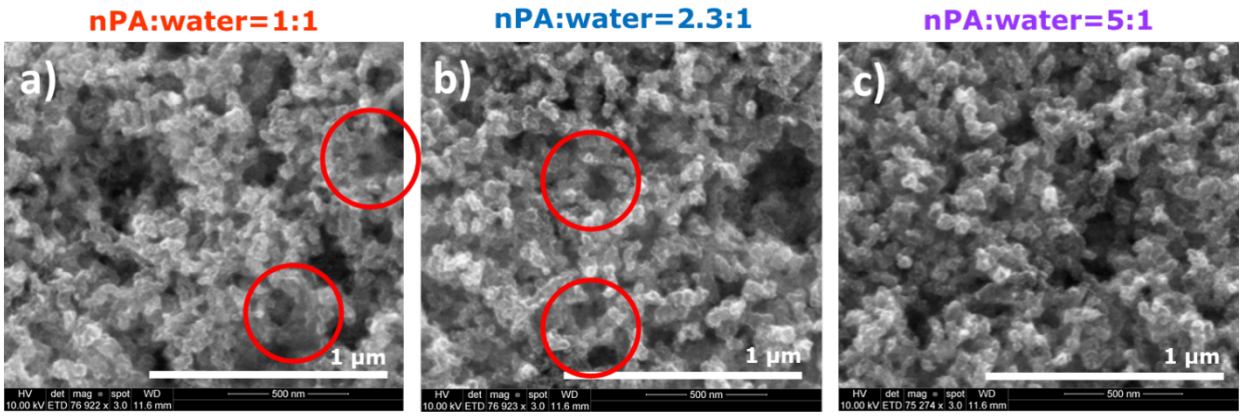

Figure 5.16: Microstructure SEMs of HOPI CCLs with nPA to water ratios of a) 1:1, b) 2.3:1, and c) 5:1. Note that the SEMs were taken from the as-fabricated decal CCLs.

With this analysis, we have shown that for our HOPI ionomer with an I/C of 0.6 and ink solvents containing nPA and water, the specific activity is largely independent of the alcohol to water solvent ratio, while O_2 transport is not. The nPA to water ratio of 2.3:1 showed improved O_2 transport capability and improved high current density performance, followed by the ratio of 5:1 and then 1:1. Further analysis is needed to determine the origins of the differences in colloidal properties that impact the final ionomer distributions and overall microstructures of the CCLs.

5.3.3 Ionomer to Carbon Ratio Optimization

With the peak performing solvent nPA:water ratio of 2.3:1 with the TKK Pt/LSAC catalyst/support, we performed an I/C optimization study, varying the I/C between 0.4 and 0.9 (mass ratios of polymer to carbon). These ionomer loadings corresponded to mass fractions of 18, 24, and 33% within the CCL. The CVs for each I/C are shown in Figure 5.17. The corresponding RF, specific activity, and CCL ohmic resistance are shown in Table 5.3. The CCL resistance was extracted from transmission line modeling of the EIS data shown in Figure 5.18 and the specific activities shown in Figure 5.19 were again extracted from the HFR and H_2 crossover corrected O_2 polarization curves shown in Figure 5.20a, along with the air polarization curve in 5.20b.

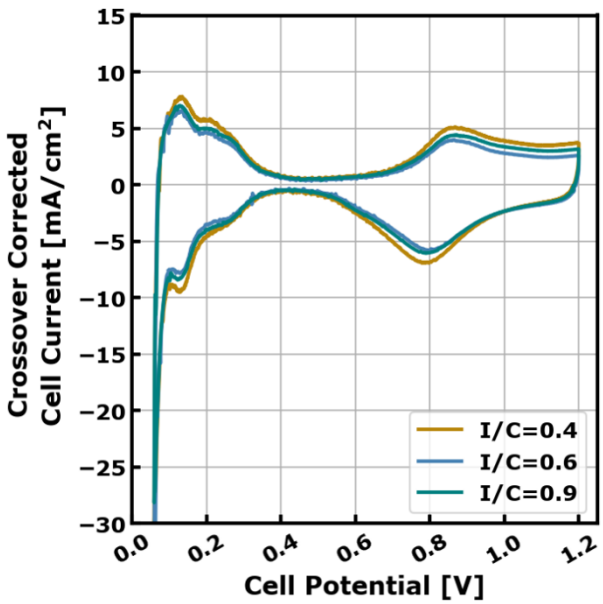

Figure 5.17: CVs of various I/C for HOPI-based CLs fabricated with 2.3:1 nPA:water ratios. CVs were taken at 30°C, 100% RH, 150 kPa_{tot} under N_2/H_2 at 0.05/0.1 SLPM.

Table 5.3: Roughness factor (RF), specific activity, and CL resistance (Ω_{CL}) data for HOPI CLs with various I/C ratios.

I/C	RF	Specific Activity [mA/cm^2_{Pt}]	Ω_{CL} [$m\Omega \cdot cm^2$]
0.4	121	0.13	136
0.6	102	0.25	50
0.9	109	0.17	25

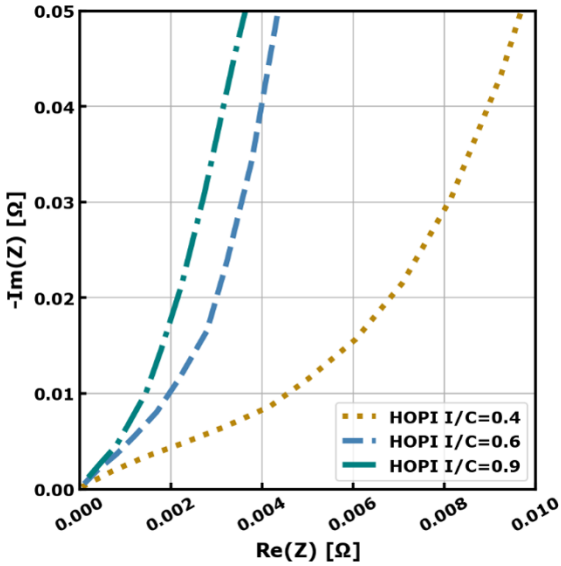

Figure 5.18: EIS data for HOPI I/C study. EIS was performed at 80°C, 100% RH, 150 kPa_{tot} under N_2/H_2 flow at 0.2/0.2 SLPM at a voltage of 0.5 V with a perturbation of 0.002 V.

From Figure 5.17 and the extracted RFs in Table 5.3, we can see that there was greater variation in overall Pt loading compared with previous analyses. The I/C of 0.6 had the lowest RF of the cohort (102) corresponding to the lowest Pt loading, and the I/C of 0.4 had the highest RF (120) and loading. Yet from the polarization curves in Figure 5.20a and 5.20b, the CCL with the I/C of 0.6 performed best, both in the low current density region (O_2 polarization curve - Figure 5.20a) and the mass transport region at high current densities with the higher loaded I/C of 0.4 performing poorly in the low current density region and worse throughout the entirety of the air polarization curve. The lackluster performance for the I/C of 0.4 is attributed to the lack of activity, as it had the lowest specific activity within the I/C study, even while performing better than the I/C of 0.9 at high current densities, where the reduced ionomer loading aided in overall O_2 transport. In contrast, the I/C of 0.9 had better specific activity than the I/C of 0.4, helping it to perform better in the O_2 polarization curve but saw performance loss at high current densities where the additional ionomer hindered O_2 delivery to the Pt surface, reducing the achievable current. The I/C of 0.6 attained the best of both cases, achieving a high specific activity and showing improved O_2 transport at high current density.

In terms of CCL ohmic resistance, the I/C of 0.4 had the highest CCL resistance, contributing to significant ohmic losses and hindering its performance from moderate to high current densities. As expected, the I/C of 0.9 had the lowest CL resistance from more connected proton conduction pathways, and the I/C of 0.6 was between the two, albeit closer to the I/C of 0.9. These values of CCL resistance are lower than typical Nafion-based CCLs, i.e. values around 100 mΩ-cm^2 for Nafion I/Cs of 0.6. This lowering of the CCL resistance is primarily due to the low EW of the HOPI compared with D2020 (870 vs 1000). With lower EWs, more sulfonate groups are present to conduct protons, enhancing the overall conductivity.

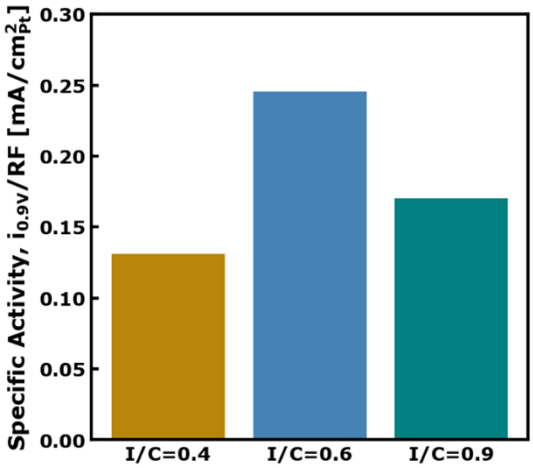

Figure 5.19: Specific activities of HOPI CCLs with various I/C ratios.

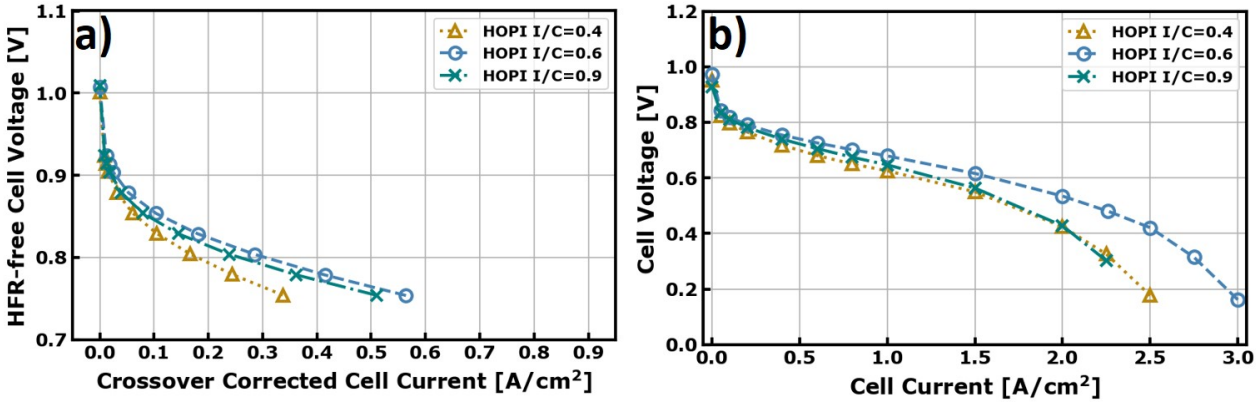

Figure 5.20: Polarization curves for HOPI I/C study under a) O_2/H_2 and b) air/H_2. Both polarization curves were taken in the anodic direction (high current to low current). Polarization curves were taken at 80°C, 100% RH, at 150 kPa_{tot} under flow rates of 2/1 SLPM to the cathode and anode, respectively.

Thus, some of the performance losses witnessed in Figure 5.20b for the I/C of 0.4 can be attributed to high CCL ohmic resistances.

To examine the impact of I/C on the R_{NF} and corresponding high current density performance, we again ran limiting current protocols at RHs of 50, 75, and 90% for the extraction of the R_{NF}'s as a function of RH as shown in Figure 5.21. We took CV's at each RH (not shown) and observed no appreciable decrease in ECSA at lower RH, allowing for comparison of the R_{NF} results between the different RHs. Figure 5.21 shows that while the I/C trends of 0.6 and 0.9 were similar, the I/C of 0.4 trend deviates significantly, experiencing a very high R_{NF} at low RH but then dropping off at high RH to achieve the lowest R_{NF}. This is consistent with the air performance data in Figure 5.20b, where the I/C of 0.4 suffers from poor performance at low current density due to low specific activity but recovers at

high current density to surpass the performance of the I/C of 0.9 that had higher specific activity. This performance increase for the I/C=0.4 is due to improved O_2 permeance that is achieved with thinner ionomer layers. Again, we can see that the I/C of 0.6 achieves the best of both worlds, benefiting from a high specific activity and good O_2 transport. Thus, with an I/C of 0.6, overall performance is maximized.

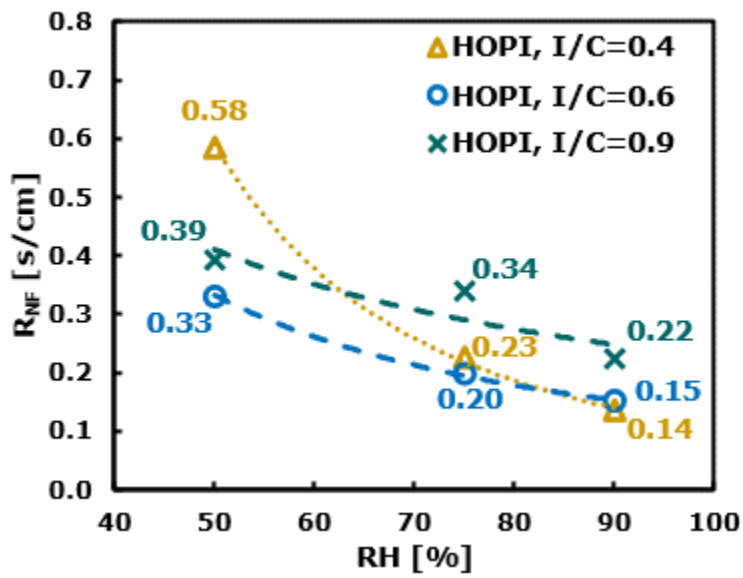

Figure 5.21: Non-Fickian O_2 transport resistance (R_{NF}) as a function of RH for CCLs prepared with varying I/Cs. Limiting current data was taken at 80°C, 50-90%RH, 100-300 kPa_{tot} under 1% O_2/H_2 at 2/1 SLPM. Note that the dashed lines are intended only as a guide for the eyes and should not be interpreted to have physical meaning.

5.4 Conclusion

In this analysis, we performed a preliminary examination of a high oxygen permeable ionomer (HOPI) made by our project parnter, Chemours, and compared it with current state-of-the-art Nafion ionomers in high and low EW configurations, i.e. 1000 EW D2020 and 880 EW DE2029. From these datasets, we showed higher specific activities for the HOPI in the low current density regions of the polarization curves and improved performance at high current densities resulting from improved O_2 transport, as confirmed by limiting current O_2 transport measurements. While the improved R_{NF}'s for the HOPI confirm improvements in O_2 permeability, further fundamental research must be done to decouple the effects of the HOPI's short side-chain chemistry from the suspected improvement in O_2 solubility on the measured improvement in specific activity.

In addition, we performed preliminary optimization studies, considering ink solvents and ionomer loading through I/C variation. Through these analyses, we determined that the HOPI achieves peak performance with the TKK EA50 (45.6 wt%) Pt/LSAC catalyst with an I/C ratio of 0.6 in a moderately alcohol-heavy solvent, specifically a 2.3:1 nPA:water weight ratio. We found that while the nPA:water ratio had overall little impact on the specific activity or Pt utilization and correspondingly little impact on low current density performance, the moderately alcohol-heavy solvent (2.3:1) contributed to an O_2 transport optimized structure allowing for improved high current density performance. The overall trends of O_2 transport performance as a function of RH for the various solvent compositions and I/Cs varied, likely due to changes in colloidal properties that affected the final morphologies of the CCLs. To examine the dependence of O_2 transport on ionomer morphology with HOPI-integrated CCLs, more research is required, specifically quantitative characterization of colloidal properties like carbon and ionomer aggregate size, zeta potential measurements, etc., and correlation with the fabricated CCLs and their electrochemical performance.

Overall, the new HOPI class of ionomers shows incredible potential for Pt-based PEMFCs to address the electrification of heavy-duty vehicles for reduced greenhouse gas emissions and the transition to an overall greener auto fleet. HOPIs are well-suited to improve efficiency due to their ability to boost apparent specific activity and improve high current density (high power) performance for vehicles needing occasional high power capability in addition to high efficiency. With our efforts in this study, we hope to promote this promising novel class of ionomers and enable the next generation of state-of-the-art PEMFC cathodes.

Chapter 6

Summary, Contributions, and Future Work

6.1 Studying Pt-Based Fuel Cell Electrode Degradation with Nanoscale X-Ray Computed Tomography

6.1.1 Summary

In this chapter, we used our nano-CT imaging technique to study CCL degradation resulting from a catalyst-specific AST and discussed the impacts of degradation within the context of the samples' electrochemical performance degradation. For the two state-of-the-art CCLs examined in this study (0.1 mg_{Pt}/cm^2 Pt/Vu and PtCo/HSC), we found that both underwent catalyst degradation, resulting in the formation of a Pt band at the cathode/membrane interface. For the Pt/Vu CCL, the Pt loss was greater, as confirmed by the electrochemical ECSA measurements. This significant loss in Pt resulted in significant performance loss through the full length of the performance curve due to severe O_2 transport limitations, in contrast with the PtCo/HSC CCL which degraded less and retained performance through much of the polarization curve. We also analyzed the effect of the AST on the carbon support structure and found that the Vu support fared better than the HSC support, which underwent compaction and loss of porosity during the cycling, which affected the PtCo/HSC's performance at high current densities.

6.1.2 Contributions

The key contributions of this work are listed below.

- We demonstrated a high-throughput analysis technique for evaluating degradation over a larger, more spatially representative volume than is possible with traditional TEM or SEM, and without processing artifacts.

- We demonstrated a porosity estimation technique for ultra-thin CCLs that resolves pores and solids on a scale that captures the unique properties of specific carbon supports that is difficult for traditional methods, i.e. BET or mercury porosimetry.

6.1.3 Future Work

The following efforts would improve the quality of our combined imaging and electrochemical degradation analysis as well as the overall state of PEMFC technology.

- PFIB-SEM of the CCLs would enable void/solid resolution at the nm-scale, allowing for a more complete degradation analysis of the carbon support.
- A study dedicated to quantifying the error associated with the X-ray CT method would add confidence to the void distribution analysis and corresponding porosities.
- This study informs the need for CCLs with tailored morphologies that suppress both catalyst and carbon support degradation, i.e. initially larger catalyst diameters for particle coarsening suppression, porous supports that minimize contact between the catalyst and ionomer, catalyst anchoring techniques, increased graphitization of the carbon support, ordered interiors of the Pt alloy catalysts, etc.
- This study informs the need for advanced stack-level voltage controls to prevent the high voltages that cause catalyst and support degradation.

6.2 Contaminant Cation Effects on Oxygen Transport Through the Ionomers of Polymer Electrolyte Membrane Fuel Cells

6.2.1 Summary

In this chapter, we evaluated the impact of contaminant cations on the O_2 transport properties of the ionomer used in PEMFC CCLs and developed hypotheses on the structure/transport relationship in contaminated, humidified ionomers. We used a novel O_2 transport cell to separate the ionomer of interest from any confinement or interfacial effects present in an operating CCL and evaluated these bulk ionomers' O_2 transport properties as a function of RH, cation valency, and cation concentration. We found that for ionomers contaminated with various cations, minimal contamination (less than 50% exchange) resulted in minimal O_2 transport losses, whereas high contamination levels (greater than 50% exchange) caused significant losses. In addition, we found that monovalent and divalent cations impacted the ionomer structure and corresponding transport differently; the monovalent cations increased ion pair strength with the sulfonate groups of the ionomer while the divalent cations formed cross links between sulfonate groups. Each mechanism ultimately increased compression of the hydrophilic domain that is responsible for O_2 transport and ultimately reduced O_2 permeation of the ionomer, hindering PEMFC performance.

6.2.2 Contributions

The key contributions of this work are listed below.

- We developed a novel O_2 transport cell that allows for the ex-situ O_2 transport characterization of ionomers without the interfacial, confinement, or polarization effects that complicate the characterization of ionomers within the CCLs.

- We demonstrated the effect of intermediate levels of Co^{2+} contamination on the O_2 transport properties of ionomer films that has not been reported in the literature to date.
- We developed ionomer structure/O_2 transport hypotheses for ionomers contaminated with monovalent and divalent cations for a range of operating RHs.

6.2.3 Future Work

The following efforts would improve the analysis and understanding of cation-contaminated ionomers and the impact on O_2 transport as well as advance the state of PEMFC technology.

- The integration of an O_2 sensor below the sample would enable more accurate estimation of the O_2 concentration used in the resistance calculation. We made this change for the water-filled micropore analysis in Chapter 4.
- Studying ionomer films of varying thickness with cation contaminants would allow for extrapolation of trends for estimation of resistances present for the ultra-thin films covering the Pt surface in real CCLs.
- Combining this chapter's analysis with more fundamental measurements, i.e. water uptake and DSC measurements, would help confirm the structure/transport hypotheses developed with the various cation study.
- This study informs the need for more robust catalysts that resist dissolution of Pt and the alloying element, i.e. Co or Ni.
- This study informs the need for ionomers that are resistance to domain collapse, i.e. ionomers with rigid backbones and side chains that resist deformation, i.e. the HOPI from Chapter 5.
- This study informs the need for cation-selective ionomers that limit the migration of cations under the potential gradient of the ionomer.
- This study informs the need for contaminant-flushing protocols to remove cation contaminants that are leached over the lifetime of PEMFC vehicles.
- This study informs the need for operating condition adjustment to mitigate the effect of cation contaminants, i.e. operating at higher RHs and lower current densities to minimize the cation/sulfonate group interactions and miminize migration of the contaminant cations.

6.3 Operando Analysis of Cesium Migration in the Catalyst Layers of PEMFCs

6.3.1 Summary

In this chapter, we studied the migration of contaminant cations within the CL of a PEMFC in-operando, using our nano-CT facility's X-ray imaging capabilities to monitor the con-

centrations of Cs^+ as a function of time under an applied current. We designed an X-ray conducive migration cell that allowed X-ray transmission of a CL/membrane interface and developed a model to corroborate our combined electrochemical and operando imaging analysis. Ultimately, our analysis showed polarization-induced migration of Cs^+ within the CL of a PEMFC under a H_2-pumping configuration and the corresponding model allowed us to estimate the diffusivity and mobility of the Cs^+ cations from the experiment. These results agreed well with previous experimental and modeling works that have predicted and shown the performance impacts of contaminant cation migration during PEMFC operation.

6.3.2 Contributions

The key contributions of this work are listed below.

- We developed a novel X-ray conducive cell hardware and methodology for visualization of cation (Cs^+) migration within an operating PEMFC CL, which has not to our knowledge been reported in the literature.
- We developed a complimentary model for estimating the diffusivity and mobility of the cation of interest (Cs^+) in our operando analysis.
- We confirmed the migration and accumulation of Cs^+ in a PEMFC CL under a H_2-pumping configuration and extracted reasonable diffusivity and mobility estimations.

6.3.3 Future Work

The following efforts, based on our work, would help advance the state of PEMFC technology.

- Reducing the sources of cation contamination would eliminate or minimize the performance degradation from migrating contaminants.
- Developing migration resistant or cation selective ionomers would help prevent accumulation of cations at the surface of the catalyst particles.

6.4 Measurement of Oxygen Transport Through Water-filled Nanopores

6.4.1 Summary

In this chapter, we examined the fundamental transport pathway of O_2 through confined water using the experimental setup from Chapter 2 with AAO membranes featuring well-controlled pore sizes of 10 and 20 nm. We took dry and filled-pore measurements, extracting the diffusivity and permeability of the AAO pores, respectively. Combining the wet and dry transports into a dimensionless transport ratio, K, allowed us to show improvement or impairment of confined water transport of O_2. For the 20 nm pores, we found that the experimentally measured dimensionless transport ratio, K, agreed well with theoretical predictions from transition-regime dry transport and bulk water transport. The 10 nm data deviated from the expected trend, showing improved wet permeation. This improvement is likely due to O_2 adsorption on the surface of the AAO pores, increasing the overall solubility

of the confined water and thus increasing the permeability. However, more experimental and MD modeling work targeting the distinction between O_2 solubility and diffusivity in confined water is needed to elucidate the origins of the witnessed experimental increase in O_2 permeation through our water-filled nanopores.

6.4.2 Contributions

The key contributions of this work are listed below.

- We experimentally measured the transport of O_2 through confined water, which to the best of our knowledge has not been reported in the literature.
- We characterized both the dry diffusivity and wet permeability for pores of 10 and 20 nm nominal diameter using anodic aluminum oxide, or AAO, membranes.
- We showed an increase in wet permeability for the 10 nm pores, likely due to O_2 adsorption to the pore walls and corresponding oversolubility for the smaller pore size.

6.4.3 Future Work

The following efforts would augment our analysis and advance the understanding of confined liquid transport of gases and help advance the state of PEMFC technology.

- To confirm our hypothesis of oversolubility in the pore, MD simulations and further experimental characterization for even smaller pores, i.e. 1-5 nm diameter are needed. Possible experimental techniques for the measurement of the solubility and diffusivity of confined O_2 in water include microelectrode integration with the AAO membrane and characterizing the Fickian and non-Fickian contributions of O_2 transport through the AAO membranes.
- The next generation of carbon supports used in fuel cell electrodes could be treated such that the surface functionalization of the carbon promotes O_2 adsorption and higher O_2 concentrations near the Pt surface for enhancement of the ORR reaction rate.

6.5 High Oxygen Permeable Ionomer Integration with State-of-the-Art Catalyst Layers

6.5.1 Summary

In this work, we integrated a novel HOPI with state-of-the-art CCLs and compared it with ionomers traditionally used in PEMFC cathodes. We also provided an initial solvent and I/C ratio optimization to inform future CCL morphology optimizations. In our analysis, we showed significant performance improvements for CCLs containing the new HOPI, compared with CCLs containing the traditional Nafion ionomer for both high and low EW versions. This performance improvement was witnessed through the full span of the performance curves and is the result of improved specific activity and improved O_2 transport. While the origins of the improved specific activity are as yet indistinguishable between side chain

length impacts and overall O_2 solubility, we have shown that the HOPI is true to its name, improving O_2 permeation at high current densities where the impact of specific activity is negated. In addition to the benchmark analysis, we showed that the HOPI is best utilized with an ink solvent consisting of n-propanol and water in a moderate ratio, i.e. 2.3:1 in our analysis and an I/C ratio of 0.6. The I/C ratio of 0.4 achieved the best O_2 transport at high current densities due to reduced ionomer film thickness but suffered low specific activity. In contrast, the I/C of 0.9 had better activity but reduced O_2 transport. The I/C of 0.6 had the best specific activity and comparable, albeit slightly worse, O_2 tranpsort compared with the I/C of 0.4. With the HOPI's improvements in low current density performance impacting PEMFC efficiency and the O_2 transport improvments at high current density improving total power, the HOPI-class of ionomers will be key in enabling the coming class of heavy duty PEMFC vehicles for which efficiency and available power are paramount.

6.5.2 Contributions

The key contributions of this work are listed below.

- We integrated the HOPI with state-of-the-art CCLs and showed improved performance at both low and high current densities, compared with the traditional Nafion ionomer used in PEFMC CCLs.
- We optimized HOPI CCLs' performance through ink solvent and I/C analyses, again showing improved performance compared to traditional Nafion-based CCLs.

6.5.3 Future Work

The following efforts would help elucidate the true impact of the HOPI on CCL morphology and performance as well as advance the state of PEMFC technology.

- In-dept colloidal analysis is needed, i.e. DLS, rheology measurements, to study and optimize HOPI coverage of the catalyst and support for peak performance and minimization of mud-cracking to address durability.
- Further integration with different state-of-the-art CCLs, i.e. HSCs, is needed to evaluate their impact in systems with minimal catalyst/ionomer interactions.
- A thorough evaluation of HOPI films O_2 solubility, diffusivity, and overall permeability are needed to decouple the impacts of the HOPI's short side-chain chemistry and the suspected improvement in O_2 solubility on the measured specific activity increase compared to traditional Nafion-based CCLs.

Bibliography

[1] Jake Rice et al. "Summary for policymakers of the regional assessment report on biodiversity and ecosystem services for the Americas of the Intergovernmental Science-Policy Platform on Biodiversity and Ecosystem Services". In: *IPBES book* (2018).

[2] Brian C O'Neill et al. "IPCC reasons for concern regarding climate change risks". In: *Nature Climate Change* 7.1 (2017), pp. 28–37.

[3] Richard SJ Tol. *Climate economics: economic analysis of climate, climate change and climate policy*. Edward Elgar Publishing, 2019.

[4] US EPA. "US transportation sector greenhouse gas emissions: 1990-2018". In: *Office of Transportation and Air Quality EPA-420-F-20-037* (2020).

[5] Simon T Thompson et al. "Direct hydrogen fuel cell electric vehicle cost analysis: System and high-volume manufacturing description, validation, and outlook". In: *Journal of Power Sources* 399 (2018), pp. 304–313.

[6] Anusorn Kongkanand. "Highly-Accessible Catalysts for Durable High-Power Performance". In: *2017 Annual Merit Review and Peer Evaluation Meeting, Washington, DC https://www.hydrogen.energy.gov/pdfs/review17/fc144_kongkanand_2017_o.pdf*. 2017.

[7] Yuxiu Liu et al. "Effects of catalyst carbon support on proton conduction and cathode performance in PEM fuel cells". In: *Journal of The Electrochemical Society* 158.6 (2011), B614.

[8] Venkata Yarlagadda et al. "Boosting fuel cell performance with accessible carbon mesopores". In: *ACS Energy Letters* 3.3 (2018), pp. 618–621.

[9] Elliot Padgett et al. "Connecting fuel cell catalyst nanostructure and accessibility using quantitative cryo-STEM tomography". In: *Journal of The Electrochemical Society* 165.3 (2018), F173.

[10] Adam Riese et al. "Accelerated stress testing by rotating disk electrode for carbon corrosion in fuel cell catalyst supports". In: *Journal of The Electrochemical Society* 162.7 (2015), F783.

[11] Rodney L Borup et al. "Recent developments in catalyst-related PEM fuel cell durability". In: *Current Opinion in Electrochemistry* 21 (2020), pp. 192–200.

[12] Laurent Rubatat et al. "Evidence of elongated polymeric aggregates in Nafion". In: *Macromolecules* 35.10 (2002), pp. 4050–4055.

[13] Frances I Allen et al. "Morphology of hydrated as-cast Nafion revealed through cryo electron tomography". In: *ACS Macro Letters* 4.1 (2015), pp. 1–5.

[14] Ahmet Kusoglu and Adam Z Weber. "New insights into perfluorinated sulfonic-acid ionomers". In: *Chemical reviews* 117.3 (2017), pp. 987–1104.

[15] Kenneth A Mauritz and Robert B Moore. "State of understanding of Nafion". In: *Chemical reviews* 104.10 (2004), pp. 4535–4586.

[16] Klaus Schmidt-Rohr and Qiang Chen. "Parallel cylindrical water nanochannels in Nafion fuel-cell membranes". In: *Nature materials* 7.1 (2008), pp. 75–83.

[17] Ahmet Kusoglu et al. "Impact of substrate and processing on confinement of Nafion thin films". In: *Advanced Functional Materials* 24.30 (2014), pp. 4763–4774.

[18] Kirt A Page et al. "Confinement-driven increase in ionomer thin-film modulus". In: *Nano letters* 14.5 (2014), pp. 2299–2304.

[19] Ryosuke Jinnouchi et al. "Molecular dynamics simulations on O2 permeation through nafion ionomer on platinum surface". In: *Electrochimica Acta* 188 (2016), pp. 767–776.

[20] Hubert A Gasteiger et al. "Activity benchmarks and requirements for Pt, Pt-alloy, and non-Pt oxygen reduction catalysts for PEMFCs". In: *Applied Catalysis B: Environmental* 56.1-2 (2005), pp. 9–35.

[21] Héctor R Colón-Mercado and Branko N Popov. "Stability of platinum based alloy cathode catalysts in PEM fuel cells". In: *Journal of Power Sources* 155.2 (2006), pp. 253–263.

[22] Kazuaki Yasuda et al. "Platinum dissolution and deposition in the polymer electrolyte membrane of a PEM fuel cell as studied by potential cycling". In: *Physical Chemistry Chemical Physics* 8.6 (2006), pp. 746–752.

[23] PJ Ferreira et al. "Instability of Pt/ C electrocatalysts in proton exchange membrane fuel cells: a mechanistic investigation". In: *Journal of the Electrochemical Society* 152.11 (2005), A2256.

[24] DD Papadias et al. "Durability of Pt-Co alloy polymer electrolyte fuel cell cathode catalysts under accelerated stress tests". In: *Journal of the Electrochemical Society* 165.6 (2018), F3166.

[25] Wu Bi, Gary E Gray, and Thomas F Fuller. "PEM fuel cell Pt/ C dissolution and deposition in nafion electrolyte". In: *Electrochemical and Solid State Letters* 10.5 (2007), B101.

[26] Lei Tang et al. "Electrochemical stability of nanometer-scale Pt particles in acidic environments". In: *Journal of the American Chemical Society* 132.2 (2010), pp. 596–600.

[27] Chao Wang et al. "Design and synthesis of bimetallic electrocatalyst with multilayered Pt-skin surfaces". In: *Journal of the American Chemical Society* 133.36 (2011), pp. 14396–14403.

[28] Lei Wang et al. "Core-shell nanostructured cobalt-platinum electrocatalysts with enhanced durability". In: *ACS Catalysis* 8.1 (2018), pp. 35–42.

[29] Vojislav R Stamenkovic et al. "Effect of surface composition on electronic structure, stability, and electrocatalytic properties of Pt-transition metal alloys: Pt-skin versus Pt-skeleton surfaces". In: *Journal of the American Chemical Society* 128.27 (2006), pp. 8813–8819.

[30] Anusorn Kongkanand and Mark F Mathias. "The priority and challenge of high-power performance of low-platinum proton-exchange membrane fuel cells". In: *The journal of physical chemistry letters* 7.7 (2016), pp. 1127–1137.

[31] Anusorn Kongkanand et al. "Achieving high-power PEM fuel cell performance with an ultralow-Pt-content core–shell catalyst". In: *ACS Catalysis* 6.3 (2016), pp. 1578–1583.

[32] Adam Z Weber and Ahmet Kusoglu. "Unexplained transport resistances for low-loaded fuel-cell catalyst layers". In: *Journal of Materials Chemistry A* 2.41 (2014), pp. 17207–17211.

[33] TA Greszler, TE Moylan, and HA Gasteiger. "Modeling the impact of cation contamination in a polymer electrolyte membrane fuel cell". In: *Handbook of Fuel Cells* (2010).

[34] Yun Cai et al. "Effects of cobalt cation on low Pt-loaded PEM fuel cell performance". In: *ECS Transactions* 69.17 (2015), p. 1047.

[35] Maximilian Schalenbach et al. "Gas permeation through nafion. Part 1: measurements". In: *The Journal of Physical Chemistry C* 119.45 (2015), pp. 25145–25155.

[36] Maximilian Schalenbach et al. "Gas permeation through nafion. Part 2: resistor network model". In: *The Journal of Physical Chemistry C* 119.45 (2015), pp. 25156–25169.

[37] K Broka and P Ekdunge. "Oxygen and hydrogen permeation properties and water uptake of Nafion® 117 membrane and recast film for PEM fuel cell". In: *Journal of applied electrochemistry* 27.2 (1997), pp. 117–123.

[38] Christopher M Evans et al. "Improving the gas barrier properties of Nafion via thermal annealing: evidence for diffusion through hydrophilic channels and matrix". In: *Macromolecules* 48.10 (2015), pp. 3303–3309.

[39] Felix N Büchi, Masanobu Wakizoe, and Supramaniam Srinivasan. "Microelectrode investigation of oxygen permeation in perfluorinated proton exchange membranes with different equivalent weights". In: *Journal of the Electrochemical Society* 143.3 (1996), p. 927.

[40] Ruiliang Jia et al. "Effect of cation contamination and hydrated pressure loading on the mechanical properties of proton exchange membranes". In: *Journal of Power Sources* 196.8 (2011), pp. 3803–3809.

[41] Shouwen Shi, Adam Z Weber, and Ahmet Kusoglu. "Structure-transport relationship of perfluorosulfonic-acid membranes in different cationic forms". In: *Electrochimica Acta* 220 (2016), pp. 517–528.

[42] KS Forland, T Okada, and S Kjelstrup Ratkje. "Molten salt regular mixture theory applied to ion exchange membranes". In: *Journal of the Electrochemical Society* 140.3 (1993), p. 634.

[43] Tatsuhiro Okada et al. "The effect of impurity cations on the transport characteristics of perfluorosulfonated ionomer membranes". In: *The Journal of Physical Chemistry B* 103.17 (1999), pp. 3315–3322.

[44] Tatsuhiro Okada et al. "Transport and equilibrium properties of Nafion® membranes with H+ and Na+ ions". In: *Journal of Electroanalytical Chemistry* 442.1-2 (1998), pp. 137–145.

[45] Tatsuhiro Okada et al. "Ion and water transport characteristics in membranes for polymer electrolyte fuel cells containing H+ and Ca2+ cations". In: *Journal of the Electrochemical Society* 144.8 (1997), p. 2744.

[46] S Litster et al. "Morphological analyses of polymer electrolyte fuel cell electrodes with nano-scale computed tomography imaging". In: *Fuel Cells* 13.5 (2013), pp. 935–945.

[47] Adam Z Weber and Charles Delacourt. "Mathematical Modelling of Cation Contamination in a Proton-exchange Membrane". In: *Fuel Cells* 8.6 (2008), pp. 459–465.

[48] BL Kienitz, H Baskaran, and TA Zawodzinski Jr. "Modeling the steady-state effects of cationic contamination on polymer electrolyte membranes". In: *Electrochimica Acta* 54.6 (2009), pp. 1671–1679.

[49] Serhiy Cherevko, Nadiia Kulyk, and Karl JJ Mayrhofer. "Durability of platinum-based fuel cell electrocatalysts: Dissolution of bulk and nanoscale platinum". In: *Nano energy* 29 (2016), pp. 275–298.

[50] Pratiti Mandal et al. "3D imaging of fuel cell electrode structure degraded under cell voltage reversal conditions using nanoscale X-ray computed tomography". In: *ECS Transactions* 69.17 (2015), p. 443.

[51] William K Epting, Jeff Gelb, and Shawn Litster. "Resolving the Three-Dimensional Microstructure of Polymer Electrolyte Fuel Cell Electrodes using Nanometer-Scale X-ray Computed Tomography". In: *Advanced Functional Materials* 22.3 (2012), pp. 555–560.

[52] Firat C Cetinbas et al. "Effects of porous carbon morphology, agglomerate structure and relative humidity on local oxygen transport resistance". In: *Journal of The Electrochemical Society* 167.1 (2019), p. 013508.

[53] Siddharth Komini Babu et al. "Resolving electrode morphology's impact on platinum group metal-free cathode performance using nano-CT of 3D hierarchical pore and ionomer distribution". In: *ACS applied materials & interfaces* 8.48 (2016), pp. 32764–32777.

[54] Aman Uddin et al. "High power density platinum group metal-free cathodes for polymer electrolyte fuel cells". In: *ACS applied materials & interfaces* 12.2 (2019), pp. 2216–2224.

[55] Binghong Han et al. "Record activity and stability of dealloyed bimetallic catalysts for proton exchange membrane fuel cells". In: *Energy & Environmental Science* 8.1 (2015), pp. 258–266.

[56] Jonathan P Braaten et al. "Studying Pt-based fuel cell electrode degradation with nanoscale X-ray computed tomography". In: *Journal of Power Sources* 478 (2020), p. 229049.

[57] Andrei Tkachuk et al. "X-ray computed tomography in Zernike phase contrast mode at 8 keV with 50-nm resolution using Cu rotating anode X-ray source". In: *Zeitschrift für Kristallographie-Crystalline Materials* 222.11/2007 (2007), pp. 650–655.

[58] Jeff T Gostick et al. "PoreSpy: A python toolkit for quantitative analysis of porous media images". In: *Journal of Open Source Software* 4.37 (2019), p. 1296.

[59] Elliot Padgett et al. "Mitigation of PEM fuel cell catalyst degradation with porous carbon supports". In: *Journal of The Electrochemical Society* 166.4 (2019), F198.

[60] Anusorn Kongkanand et al. "(Plenary) Electrochemical Diagnostics and Modeling in Developing the PEMFC Cathode". In: *ECS Transactions* 75.14 (2016), p. 25.

[61] Natalia Macauley et al. "Carbon corrosion in PEM fuel cells and the development of accelerated stress tests". In: *Journal of The Electrochemical Society* 165.6 (2018), F3148.

[62] Karren L. More and David Cullen. "Characterizations of Fuel Cell Materials". In: *DOE Hydrogen and Fuel Cells Program Annual Merit Review.*

[63] Jon P Owejan, Jeanette E Owejan, and Wenbin Gu. "Impact of platinum loading and catalyst layer structure on PEMFC performance". In: *Journal of The Electrochemical Society* 160.8 (2013), F824.

[64] Thomas A Greszler, David Caulk, and Puneet Sinha. "The impact of platinum loading on oxygen transport resistance". In: *Journal of The Electrochemical Society* 159.12 (2012), F831.

[65] Hang Liu, William K Epting, and Shawn Litster. "Gas transport resistance in polymer electrolyte thin films on oxygen reduction reaction catalysts". In: *Langmuir* 31.36 (2015), pp. 9853–9858.

[66] Frank D Coms, Han Liu, and Jeanette E Owejan. "Mitigation of perfluorosulfonic acid membrane chemical degradation using cerium and manganese ions". In: *ECS Transactions* 16.2 (2008), p. 1735.

[67] Tatsuhiro Okada et al. "Unprecedented effect of impurity cations on the oxygen reduction kinetics at platinum electrodes covered with perfluorinated ionomer". In: *Langmuir* 15.24 (1999), pp. 8490–8496.

[68] A Steck and HL Yeager. "Water sorption and cation-exchange selectivity of a perfluorosulfonate ion-exchange polymer". In: *Analytical Chemistry* 52.8 (1980), pp. 1215–1218.

[69] Timothy D Gierke, GE Munn, and FCd Wilson. "The morphology in nafion perfluorinated membrane products, as determined by wide-and small-angle x-ray studies". In: *Journal of Polymer Science: Polymer Physics Edition* 19.11 (1981), pp. 1687–1704.

[70] Nikhil H Jalani and Ravindra Datta. "The effect of equivalent weight, temperature, cationic forms, sorbates, and nanoinorganic additives on the sorption behavior of Nafion®". In: *Journal of membrane science* 264.1-2 (2005), pp. 167–175.

[71] Andrew M Baker et al. "Cerium migration during PEM fuel cell assembly and operation". In: *ECS Transactions* 69.17 (2015), p. 1009.

[72] Andrew M Baker et al. "The effects of cerium migration on pem fuel cell performance". In: *ECS Transactions* 80.8 (2017), p. 643.

[73] Jonathan P Braaten et al. "Contaminant Cation Effect on Oxygen Transport through the Ionomers of Polymer Electrolyte Membrane Fuel Cells". In: *Journal of The Electrochemical Society* 166.16 (2019), F1337.

[74] Daniel R Baker et al. "Measurement of oxygen transport resistance in PEM fuel cells by limiting current methods". In: *Journal of The Electrochemical Society* 156.9 (2009), B991.

[75] Tatsuhiro Okada et al. "Ion and water transport characteristics of Nafion membranes as electrolytes". In: *Electrochimica Acta* 43.24 (1998), pp. 3741–3747.

[76] Morihiro Saito, Kikuko Hayamizu, and Tatsuhiro Okada. "Temperature dependence of ion and water transport in perfluorinated ionomer membranes for fuel cells". In: *The Journal of Physical Chemistry B* 109.8 (2005), pp. 3112–3119.

[77] Hiroshisa Yoshida and Yuka Miura. "Behavior of water in perfluorinated ionomer membranes containing various monovalent cations". In: *Journal of membrane science* 68.1-2 (1992), pp. 1–10.

[78] Laércio Gomes Lage, Patriécia Gomes Delgado, and Yoshio Kawano. "Vibrational and thermal characterization of Nafion® membranes substituted by alkaline earth cations". In: *European polymer journal* 40.7 (2004), pp. 1309–1316.

[79] Kinji Asaka et al. "State of water and ionic conductivity of solid polymer electrolyte membranes in relation to polymer actuators". In: *Journal of Electroanalytical Chemistry* 505.1-2 (2001), pp. 24–32.

[80] Gang Xie and Tatsuhiro Okada. "The state of water in Nafion 117 of various cation forms". In: *Denki Kagaku oyobi Kogyo Butsuri Kagaku* 64.6 (1996), pp. 718–726.

[81] Anne-Laure Rollet et al. "A SANS determination of the influence of external conditions on the nanostructure of nafion membrane". In: *Journal of Polymer Science Part B: Polymer Physics* 39.5 (2001), pp. 548–558.

[82] Yun Cai et al. "Electrode edge cobalt cation migration in an operating fuel cell: an in situ micro-X-ray fluorescence study". In: *Journal of The Electrochemical Society* 165.6 (2018), F3132.

[83] Jing Qi et al. "Effect of cationic contaminants on polymer electrolyte fuel cell performance". In: *Journal of Power Sources* 286 (2015), pp. 18–24.

[84] Mark Sulek et al. "In situ metal ion contamination and the effects on proton exchange membrane fuel cell performance". In: *Journal of Power Sources* 196.21 (2011), pp. 8967–8972.

[85] Andrew M Baker et al. “Cerium ion mobility and diffusivity rates in perfluorosulfonic acid membranes measured via hydrogen pump operation”. In: *Journal of The Electrochemical Society* 164.12 (2017), F1272.

[86] August Beer. “Bestimmung der absorption des rothen lichts in farbigen flussigkeiten”. In: *Ann. Physik* 162 (1852), pp. 78–88.

[87] Johann Heinrich Lambert. *Photometria sive de mensura et gradibus luminis, colorum et umbrae*. sumptibus vidvae E. Klett, typis CP Detleffsen, 1760.

[88] Donald F Swinehart. “The beer-lambert law”. In: *Journal of chemical education* 39.7 (1962), p. 333.

[89] Alan D McNaught, Andrew Wilkinson, et al. *Compendium of chemical terminology*. Vol. 1669. Blackwell Science Oxford, 1997.

[90] Stephen J Paddison, David W Reagor, and Thomas A Zawodzinski Jr. “High frequency dielectric studies of hydrated Nafion®”. In: *Journal of Electroanalytical Chemistry* 459.1 (1998), pp. 91–97.

[91] Jennifer Peron et al. “Properties of Nafion® NR-211 membranes for PEMFCs”. In: *Journal of Membrane Science* 356.1-2 (2010), pp. 44–51.

[92] Thomas A Zawodzinski Jr et al. “Water uptake by and transport through Nafion® 117 membranes”. In: *Journal of the electrochemical society* 140.4 (1993), p. 1041.

[93] John H Hubbell and Stephen M Seltzer. *Tables of X-ray mass attenuation coefficients and mass energy-absorption coefficients 1 keV to 20 MeV for elements Z= 1 to 92 and 48 additional substances of dosimetric interest*. Tech. rep. National Inst. of Standards and Technology-PL, Gaithersburg, MD (United States), 1995.

[94] Swee Chye Yeo and A Eisenberg. “Physical properties and supermolecular structure of perfluorinated ion-containing (Nafion) polymers”. In: *Journal of applied polymer science* 21.4 (1977), pp. 875–898.

[95] Rohit Makharia, Mark F Mathias, and Daniel R Baker. “Measurement of catalyst layer electrolyte resistance in PEFCs using electrochemical impedance spectroscopy”. In: *Journal of The Electrochemical Society* 152.5 (2005), A970.

[96] Johannes Schindelin et al. “Fiji: an open-source platform for biological-image analysis”. In: *Nature methods* 9.7 (2012), pp. 676–682.

[97] HL Yeager and B Kipling. “Ionic diffusion and ion clustering in a perfluorosulfonate ion-exchange membrane”. In: *Journal of Physical Chemistry* 83.14 (1979), pp. 1836–1839.

[98] Haruo Sato, Mikazu Yui, and Hideki Yoshikawa. “Ionic diffusion coefficients of Cs+, Pb2+, Sm3+, Ni2+, SeO2-4 and TcO- 4 in free water determined from conductivity measurements”. In: *Journal of Nuclear Science and Technology* 33.12 (1996), pp. 950–955.

[99] Nagappan Ramaswamy et al. “Carbon Support Microstructure Impact on High Current Density Transport Resistances in PEMFC Cathode”. In: *Journal of The Electrochemical Society* 167.6 (2020), p. 064515.

[100] Kensaku Kodama et al. "Effect of the side-chain structure of perfluoro-sulfonic acid ionomers on the oxygen reduction reaction on the surface of Pt". In: *ACS Catalysis* 8.1 (2018), pp. 694–700.

[101] A Stassi et al. "Performance comparison of long and short-side chain perfluorosulfonic membranes for high temperature polymer electrolyte membrane fuel cell operation". In: *Journal of Power Sources* 196.21 (2011), pp. 8925–8930.

[102] Samaneh Shahgaldi, Ibrahim Alaefour, and Xianguo Li. "The impact of short side chain ionomer on polymer electrolyte membrane fuel cell performance and durability". In: *Applied energy* 217 (2018), pp. 295–302.

[103] Kazuma Shinozaki et al. "Suppression of oxygen reduction reaction activity on Pt-based electrocatalysts from ionomer incorporation". In: *Journal of Power Sources* 325 (2016), pp. 745–751.

[104] Tai Bui et al. "Transport mechanism of guest methane in water-filled nanopores". In: *The Journal of Physical Chemistry C* 121.29 (2017), pp. 15675–15686.

[105] Greeshma Gadikota et al. "Hydrophobic solvation of gases (CO2, CH4, H2, noble gases) in clay interlayer nanopores". In: *The Journal of Physical Chemistry C* 121.47 (2017), pp. 26539–26550.

[106] Hongguang Sui, Jun Yao, and Lei Zhang. "Molecular simulation of shale gas adsorption and diffusion in clay nanopores". In: *Computation* 3.4 (2015), pp. 687–700.

[107] Edward Lansing Cussler and Edward Lansing Cussler. *Diffusion: mass transfer in fluid systems*. Cambridge university press, 2009.

[108] Nobuaki Nonoyama et al. "Analysis of oxygen-transport diffusion resistance in proton-exchange-membrane fuel cells". In: *Journal of The Electrochemical Society* 158.4 (2011), B416.

[109] WGt Pollard and Richard David Present. "On gaseous self-diffusion in long capillary tubes". In: *Physical Review* 73.7 (1948), p. 762.

[110] Ning Hsing Chen and DF Othmer. "New generalized equation for gas diffusion coefficient." In: *Journal of Chemical and Engineering Data* 7.1 (1962), pp. 37–41.

[111] Hiroshi Ito et al. "Properties of Nafion membranes under PEM water electrolysis conditions". In: *International journal of hydrogen energy* 36.17 (2011), pp. 10527–10540.

[112] RF Mann et al. "Henry's Law and the solubilities of reactant gases in the modelling of PEM fuel cells". In: *Journal of power sources* 161.2 (2006), pp. 768–774.

[113] Donald Lee Wise and Gb Houghton. "The diffusion coefficients of ten slightly soluble gases in water at 10–60 C". In: *Chemical Engineering Science* 21.11 (1966), pp. 999–1010.

[114] William P Krekelberg et al. "Impact of surface roughness on diffusion of confined fluids". In: *The Journal of chemical physics* 135.15 (2011), p. 154502.

[115] Kourosh Malek and Marc-Olivier Coppens. "Pore roughness effects on self-and transport diffusion in nanoporous materials". In: *Colloids and Surfaces A: Physicochemical and Engineering Aspects* 206.1-3 (2002), pp. 335–348.

[116] Kourosh Malek and Marc-Olivier Coppens. "Effects of surface roughness on self-and transport diffusion in porous media in the Knudsen regime". In: *Physical review letters* 87.12 (2001), p. 125505.

[117] Anh Phan, David R Cole, and Alberto Striolo. "Aqueous methane in slit-shaped silica nanopores: high solubility and traces of hydrates". In: *The Journal of Physical Chemistry C* 118.9 (2014), pp. 4860–4868.

[118] Aman Sharma, Sadanandam Namsani, and Jayant K Singh. "Molecular simulation of shale gas adsorption and diffusion in inorganic nanopores". In: *Molecular Simulation* 41.5-6 (2015), pp. 414–422.

[119] Marc Pera-Titus et al. "Direct volumetric measurement of gas oversolubility in Nanoliquids: beyond Henry's law". In: *ChemPhysChem* 10.12 (2009), pp. 2082–2089.

[120] Fuqiang Liu et al. "Nafion/PTFE composite membranes for fuel cell applications". In: *Journal of Membrane Science* 212.1-2 (2003), pp. 213–223.

[121] T Leon Yu et al. "Nafion/PTFE composite membranes for fuel cell applications". In: *Journal of Polymer Research* 11.3 (2004), pp. 217–224.

[122] Takuya Masuda et al. "Potential-dependent adsorption and desorption of perfluorosulfonated ionomer on a platinum electrode surface probed by electrochemical quartz crystal microbalance and atomic force microscopy". In: *The Journal of Physical Chemistry C* 117.30 (2013), pp. 15704–15709.

[123] Andrea Rolfi et al. "New perfluorinated ionomer with improved oxygen permeability for application in cathode polymeric electrolyte membrane fuel cell". In: *Journal of Power Sources* 396 (2018), pp. 95–101.

[124] Adlai Katzenberg et al. "Highly Permeable Perfluorinated Sulfonic Acid Ionomers for Improved Electrochemical Devices: Insights into Structure-Property Relationships". In: *Journal of the American Chemical Society* 142.8 (2020), pp. 3742–3752.

[125] Ryo Shimizu et al. "Effects of both oxygen permeability and ion exchange capacity for cathode ionomers on the performance and durability of polymer electrolyte fuel cells". In: *Journal of The Electrochemical Society* 165.6 (2018), F3063.

[126] Tadashi Ino et al. *Ionomer having high oxygen permeability.* US Patent 10,189,927. 2019.

[127] Nobuaki Nonoyama et al. *Cathode catalyst layer, membrane electrode assembly and polymer electrolyte fuel cell and manufacturing method thereof.* US Patent 9,431,661. 2016.

[128] Ryan O'hayre et al. *Fuel cell fundamentals.* John Wiley & Sons, 2016.

[129] Bhaskar Sompalli et al. *Methods of preparing membrane electrode assemblies.* US Patent 6,524,736. 2003.

[130] Venkata Yarlagadda et al. "Preparation of PEMFC electrodes from milligram-amounts of catalyst powder". In: *Journal of the Electrochemical Society* 164.7 (2017), F845.

[131] Min Wang et al. "Impact of catalyst ink dispersing methodology on fuel cell performance using in-situ X-ray scattering". In: *ACS Applied Energy Materials* 2.9 (2019), pp. 6417–6427.

[132] Sadia Kabir et al. "Elucidating the dynamic nature of fuel cell electrodes as a function of conditioning: an ex situ material characterization and in situ electrochemical diagnostic study". In: *ACS applied materials & interfaces* 11.48 (2019), pp. 45016–45030.

[133] Jingxin Zhang et al. *Methods and processes to recover voltage loss of pem fuel cell stack*. US Patent App. 12/939,867. 2011.

[134] US Fuel Cell Council. *Single Cell Test Protocol*. Report. 2006. URL: `http://www.members.fchea.org/core/import/PDFs/Technical%5C%20Resources/MatComp%5C%20Single%5C%20Cell%5C%20Test%5C%20Protocol%5C%2005-014RevB.2%5C%20071306.pdf`.

Appendix A

Abbreviations and Acronyms

AAO	Anodic aluminum oxide
ABS	Nano-CT absorption contrast mode
ACL	Anode catalyst layer
AST	Accelerated stability test
BC	Boundary condition
CCL	Cathode catalyst layer
CCM	Catalyst coated membrane
Ce	Cerium
CL	Catalyst layer
Co	Cobalt
CV	Cyclic voltammetry or voltammogram
ECSA	Electrochemically active surface area
EIS	Electrochemical impedance spectroscopy
Fe	Iron
FOV	Field of view
GDL	Gas diffusion layer
H_2	Hydrogen
HER	Hydrogen evolution reaction
HFR	High frequency resistance
HOPI	High oxygen permeable ionomer
HOR	Hydrogen oxidation reaction
HRES	High-resolution mode for the nano-CT
HSC	Generic nomenclature for high surface area carbon
I/C	Ionomer to carbon mass ratio
ICP-OES	Inductively-coupled plasma optical emission spectroscopy
IPA	Isopropanol
LFOV	Large field of view mode for the nano-CT
Li	Lithium
LSAC	Low surface area carbon
LSV	Linear sweep voltammetry
MD	Molecular dynamics

MEA	Membrane electrode assembly
N_2	Nitrogen
Na	Sodium
nano-CT	Nanoscale X-ray compute tomography
Ni	Nickel
nPA	n-propanol
O_2	Oxygen
OCV	Open circuit voltage
ORR	Oxygen reduction reaction
PDF	Probability distribution function
PEMFC	Polymer electrolyte membrane fuel cell or proton exchange membrane fuel cell
PEM	Proton exchange membrane or polymer electrolyte membrane
PFIB-SEM	Plasma focused ion beam scanning electron microscopy
PFSA	Perfluoro-sulfonic acid
Pt	Platinum
Pt/Vu	Platinum supported on Vulcan carbon
Pt/LSAC	Platinum supported on low surface area carbon
PtCo/HSC	Platinum cobalt alloy supported on high surface area carbon
PTFE	Polytetrafluoroethylene or Teflon
RF	Roughness factor
RH	Relative humidity
ROI	Region of interest
R_{NF}	Non-Fickian oxygen transport resistance
R_{O2}	Oxygen transport resistance
SEM	Scanning electron microscopy
TEM	Transmission electron microscopy
UPD	Underpotential deposition
VR	Voltage recovery
Vu	Vulcan carbon
ZPC	Nano-CT's Zernike phase contrast mode